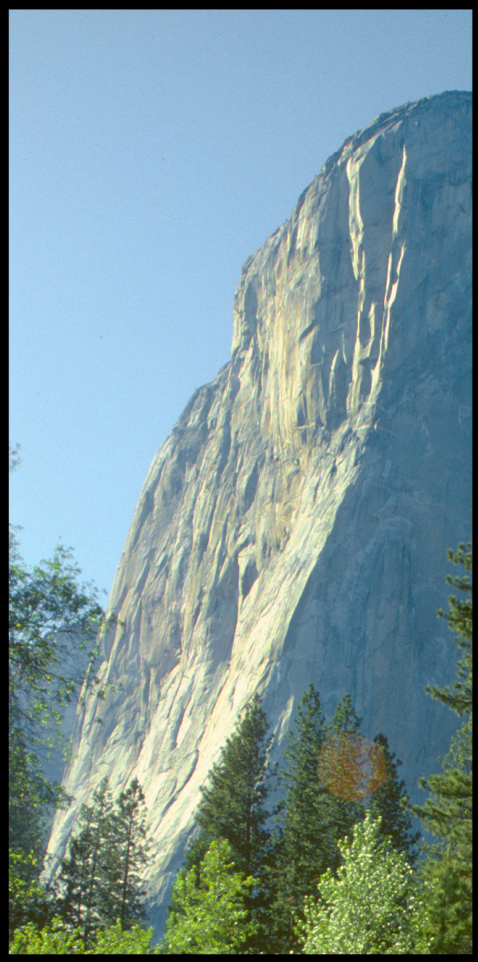

YOSEMITE

Aerosol Characterization Study of 2002 (YACS)

ISSN 0737-5352-69

National Park Service

Colorado State University CIRA

Prepared by:

Department of Atmospheric Science

Christian M. Carrico
Sonia M. Kreidenweis
Jeffrey L. Collett, Jr.
Gavin R. McMeeking
Pierre Herckes
Guenter Engling
Taehyoung Lee
Jacqueline Carrillo

and:

Cooperative Institute for Research in the Atmosphere / National Park Service

Derek Day
William C. Malm
Jenny L. Hand

Colorado State University, Ft. Collins, CO 80523 USA

1. *EXECUTIVE SUMMARY:*
THE YOSEMITE AEROSOL CHARACTERIZATION STUDY

The Yosemite Aerosol Characterization Study (YACS) was an intensive field measurement campaign conducted by a number of U.S. research groups from 15 July to 4 September 2002 at Yosemite National Park (NP), California. This summary describes the major findings of the study in the context of outstanding issues related to the Regional Haze Rule and to visibility and air quality concerns specific to Yosemite NP.

Aerosol composition measurements have been conducted in Yosemite NP since 1988 as part of the Interagency Monitoring of Protected Environments (IMPROVE) network. The long-term data record (1988–2004) clearly shows a seasonal trend in organic aerosol mass concentrations, with peaks in the summer and early fall (Figure 1). The long-term Yosemite data show that organic carbon contributes between 40 and 60% of the monthly average fine aerosol mass. These fractions are much higher than most IMPROVE sites in the eastern United States. Not only the total fine particulate mass concentration, but also the fraction attributable to organic species, increases during summer and fall. Furthermore, the variability in organic aerosol mass concentrations becomes much larger in those seasons.

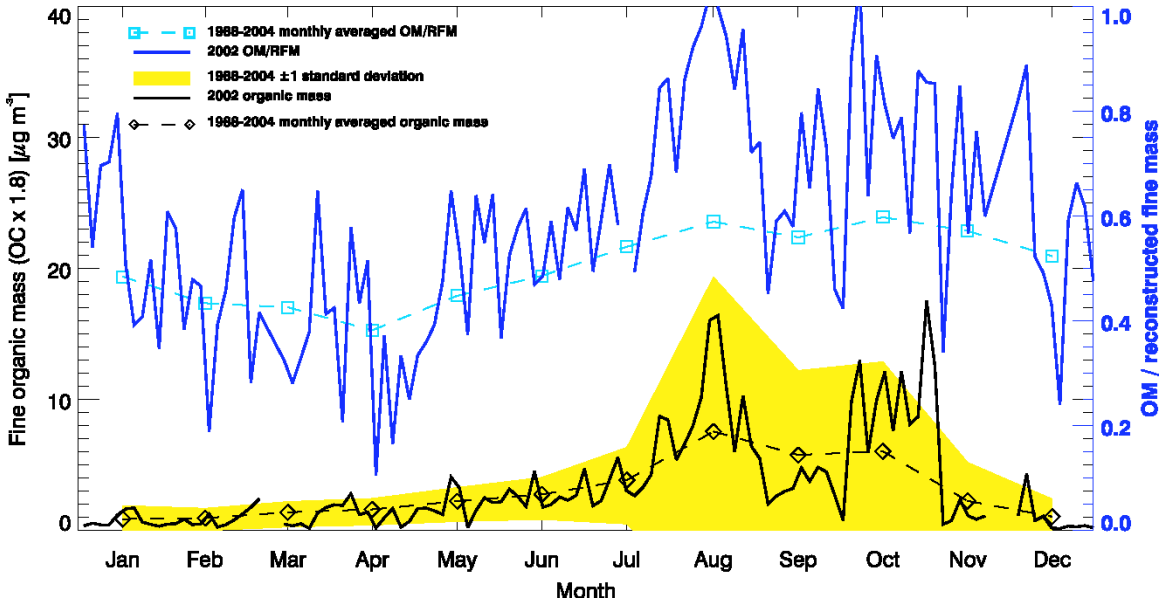

Figure 1.1 Annual variation of organic carbon mass concentrations in the fine mode of the aerosol ($PM_{2.5}$), from data obtained from the IMPROVE database (http://vista.cira.colostate.edu/views/). A measure of interannual variability is indicated by the yellow shaded area, which envelops one standard deviation in the data. Blue lines indicate the fraction of fine particulate mass concentration apportioned to organic carbon over the long-term average and for 2002.

These observations suggest an important role for organic carbon in air quality and visibility degradation in Yosemite NP. However, at the time this study was planned, several key properties of aerosol organic carbon were unknown, all of which affect estimates of visibility impairment.

- First, organic carbon in atmospheric aerosols exists in molecular forms that incorporate hydrogen, oxygen, nitrogen, and possibly other elements. However, the standard IMPROVE analytical technique measures only carbon concentrations, and thus a multiplication factor that accounts for additional weight contributed by other elements is needed to determine the total organic aerosol mass concentration in the atmosphere. Although a factor of 1.4 is used for this conversion in the Regional Haze Rule, recent studies suggested this factor may not be appropriate for many of the rural and remote locations represented in IMPROVE. The study design included measurements that could be used to constrain total mass and thus to deduce appropriate conversion factors for summertime Yosemite aerosols.
- Second, it was unknown whether the organic carbon fraction of the total aerosol could absorb water in response to increases in ambient relative humidity; standard IMPROVE and Regional Haze Rule visibility calculations assume it cannot. The absorption of water can dramatically increase total atmospheric aerosol mass concentrations and also tends to enhance extinction per unit mass. Both effects can significantly increase estimates of visibility impairment and thus need to be accurately modeled. To address these questions, the study design included measurements to quantify the increase in extinction, as a function of relative humidity, due to water uptake by aerosol organic carbon.
- Finally, the standard IMPROVE measurements can provide little insight into the sources of aerosol organic particulate matter, although the increased variability and occurrence of higher organic aerosol mass concentrations during years having severe wildfire seasons suggest that wildfire emissions are important. However, tourism in Yosemite NP follows a similar seasonal trend. Elucidation of the respective contributions of wildfire emissions and transportation sources to particulate organic matter concentrations in Yosemite NP was a third key objective of the Yosemite Aerosol Characterization Study. Sampling occurred at the elevated Turtleback Dome site, the location of the long-term IMPROVE monitors, and at a ground-level site in Yosemite Valley.

1.1 Study Objectives

- **Determine appropriate values for converting analyzed aerosol carbon mass to ambient aerosol organic carbon mass.**
- **Develop an improved understanding of the visibility-impairment-related characteristics of a smoke/organic carbon-dominated aerosol, including the role of relative humidity in modifying visibility impairment.**
- **Examine the sources contributing to high aerosol organic carbon mass concentrations.**

1.2 Study Findings

- **Accurate modeling of the effects of aerosols on summertime visibility in Yosemite NP requires revision of several commonly-applied assumptions.**
  - The total mass of organic compounds present in fine particulate matter at Turtleback Dome was better represented by multiplying elemental carbon concentrations by 1.8, rather than by 1.4 (Figure 2). The commonly applied 1.4 factor underestimated the total mass concentration of fine-mode organic aerosol by more than 25%. This higher multiplier suggests that a significant fraction of the aerosol organic matter comprised highly oxygenated organic species.

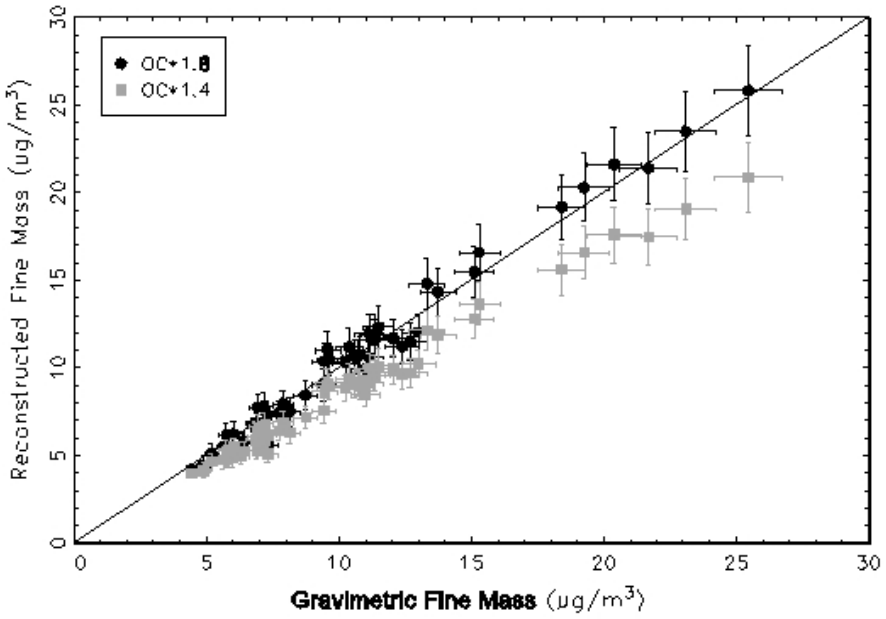

Figure 1.2 Fine mass concentrations reconstructed from individual species concentration measurements, plotted against fine mass concentrations determined by gravimetry (weighing of filters). Reconstructions are shown for two assumptions regarding the elemental-to-molecular mass conversion for organic carbon.

- The average dry mass scattering efficiency of the $PM_{2.5}$ aerosol was determined to be close to 4 $m^2\ g^{-1}$, the same value used in the IMPROVE protocols to estimate dry light scattering coefficients of organic carbon particulate matter. However, during periods of high fine mass concentrations dominated by organic carbon and influenced by fire emissions, the dry mass scattering efficiencies ranged as high as 6 $m^2\ g^{-1}$. The standard IMPROVE formula thus underestimates the contribution of organic carbon to total light scattering by as much as 50% during these periods.

- Light absorption was better modeled if it was assumed that elemental carbon was mixed with other constituents in individual particles, rather than assuming it was present as a separate mode. Single-particle analyses by electron microscopy also suggested that aerosol constituents were mostly found together in individual particles. IMPROVE formulas base the optical properties of elemental carbon on the assumption that it is not mixed with other aerosol species.

- At 85% relative humidity, aerosol light scattering coefficients are enhanced by a factor of 1.1 to 1.3 due to the presence of condensed water in the aerosol phase. This is much lower than the factors expected for aerosols dominated by sulfate compounds.

- Nitrate in the fine particle mode was associated most often with reacted sea salt and was only occasionally present as ammonium nitrate, which is the assumed molecular form in IMPROVE conversion equations. The reacted sea salt is present primarily in the coarse mode, although some of this mass is captured and detected on the $PM_{2.5}$ filter samples. Nitrate associated with coarse sea salt particles has a lower impact on visibility per unit mass than is assumed for fine mode ammonium nitrate in the IMPROVE equations. However, this is partially compensated for by lower estimates of nitrate species mass concentrations, because the molecular mass of sodium nitrate is slightly larger than that for ammonium nitrate.

- **Organic carbon was the dominant component of fine particulate matter in Yosemite NP during summer 2002, and $PM_{2.5}$ mass concentrations were higher than long-term average concentrations.**
  - Figure 3 shows the study-averaged fine ($PM_{2.5}$) aerosol composition as observed at Turtleback Dome and at the Yosemite Valley site, along with an estimate of the coarse mass concentration (PM_{10}–$PM_{2.5}$). Organic carbon represented, on average, more than 70% of the fine mass concentration at both sites.

- The average $PM_{2.5}$ mass concentration in Yosemite Valley during the study was 16 ± 5 μg m^{-3}, and at Turtleback Dome it was 10 ± 4 μg m^{-3}. This compares with July–August average values over 1988–2004, calculated from data in the IMPROVE database for the Yosemite NP site at Turtleback Dome, of 8 ± 5 μg m^{-3}. As can be seen in Figure 3, most of the difference in the fine aerosol mass concentrations between the two sites was due to higher concentrations of aerosol organic carbon at the Valley Floor site.

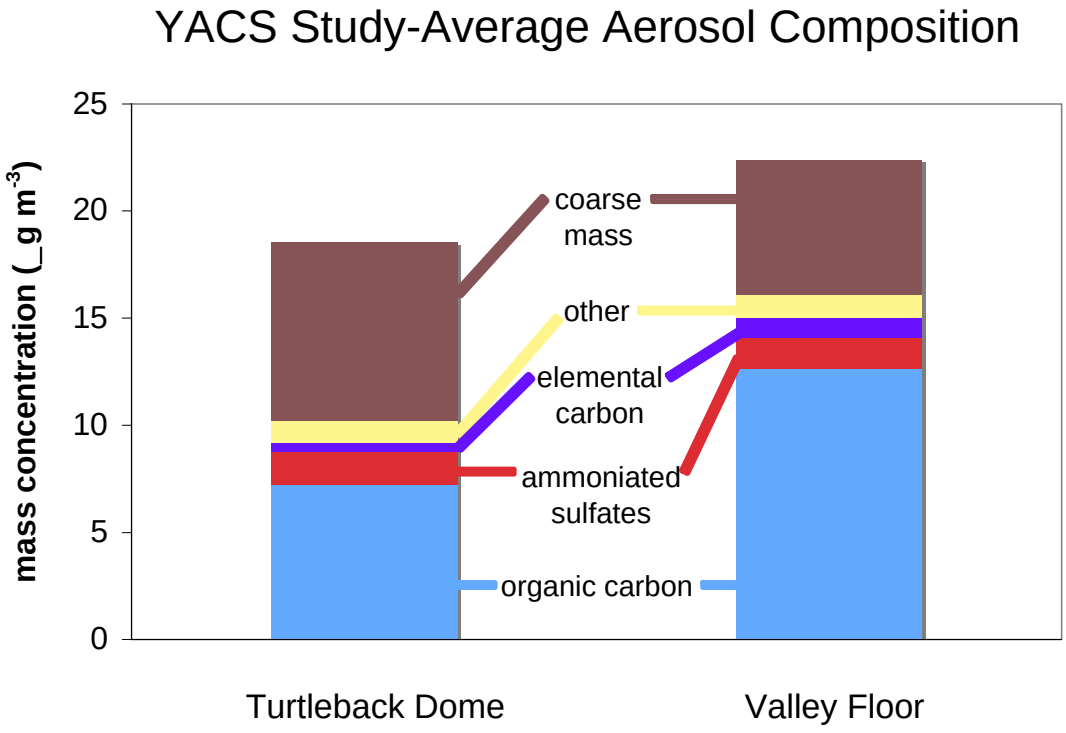

Figure 1.3 PM_{10} aerosol mass concentrations reconstructed from individual species concentration measurements, for the Turtleback Dome and Valley Floor sites.

- **Fine particles were the dominant contributor to visibility degradation at Turtleback Dome during summer 2002.**
  - The average total (gas plus aerosol) extinction coefficient at Turtleback Dome was 57 ± 31 Mm^{-1}, representing the mean value ± one standard deviation. This corresponds to a visual range of approximately 69 km. The highest values of the extinction coefficient occurred in mid-August and were on the order of 191 Mm^{-1} (20-km visual range). This compares with the proposed annual average extinction coefficient for "natural background" conditions in the nonurban western United States of 15.8 Mm^{-1}.

- On average, 77% of the total light extinction coefficient was attributed to scattering by fine particles; absorption by fine particles and scattering by coarse mode particles contributed 8% and 15%, respectively (Figure 4).

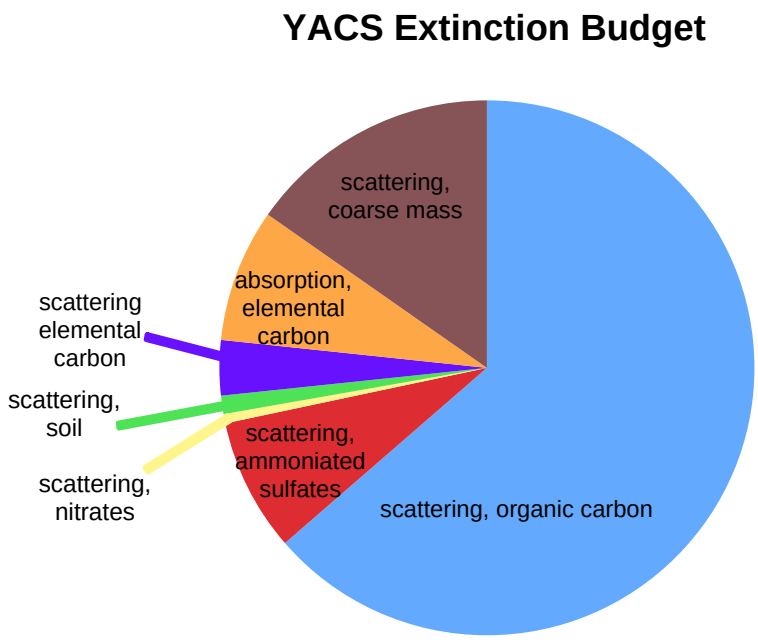

Figure 1.4 Reconstructed, study-averaged extinction budget at Turtleback Dome. All species except coarse mass are in the fine aerosol mode.

- **Natural (biogenic) sources dominated the total, and the variability in, particulate organic mass concentrations in summer 2002 at Turtleback Dome.**
  - Carbon isotope analyses of fine aerosol filter samples from Turtleback Dome determined a constant contribution from fossil fuel sources of 0.7 ± 0.1 µg m^{-3} to particulate organic matter. Contemporary (biogenically derived) carbon represented 2–9 µg m^{-3}. Sources of contemporary aerosol carbon include emissions from fires and vegetative emissions of reactive gases that subsequently form condensable species, both particulate primary emissions and volatile organic aerosol precursors that are later oxidized to secondary organic aerosols.

- **There is evidence that particulate matter sampled at Turtleback Dome was strongly influenced by the long-range transport of emissions from wildfires.**
  - During the summer of 2002, wildfires burned more than 7 million acres in the United States. Several of the largest and longest-lived fires were in southern Oregon and California. Back and

forward trajectories indicate that fire emissions were transported into California, and that a regional haze affected much of the state during August. Figure 5 shows an example satellite image from MODIS (http://modis.gsfc.nasa.gov/gallery/).

Figure 1.5 MODIS image (August 18) of smoke from fires (red areas) in Oregon and in Sequoia National Park transported into California's Central Valley.

- Back trajectory analyses and molecular marker techniques also confirmed the influence of smoke on aerosols sampled at the site. Figure 6 shows the study-average apportionment of $PM_{2.5}$ organic carbon measured at Turtleback Dome to various sources for which molecular markers and source signature profiles exist. The apportionment was highly variable in time, with primary wood smoke particles estimated to contribute <1% during the first week of the study to a high of 65% during the last week. Transportation sources contributed 4–19% on a weekly basis, and 10% on average, at this site. Most of the organic carbon mass could not be attributed to primary emissions from known sources and was thus assumed to be secondary in nature. Given the modern carbon signature observed in Turtleback Dome aerosol, most of the secondary material probably was derived from oxidation of biogenic volatile organic

compound (VOC) emissions. VOCs associated with wildfire smoke appeared to be significant contributors to secondary organic aerosol.

- Although fewer measurements of organic aerosol speciation were available at the Valley Floor site, data available from that location suggest a somewhat larger contribution of transportation sources to observed organic carbon.

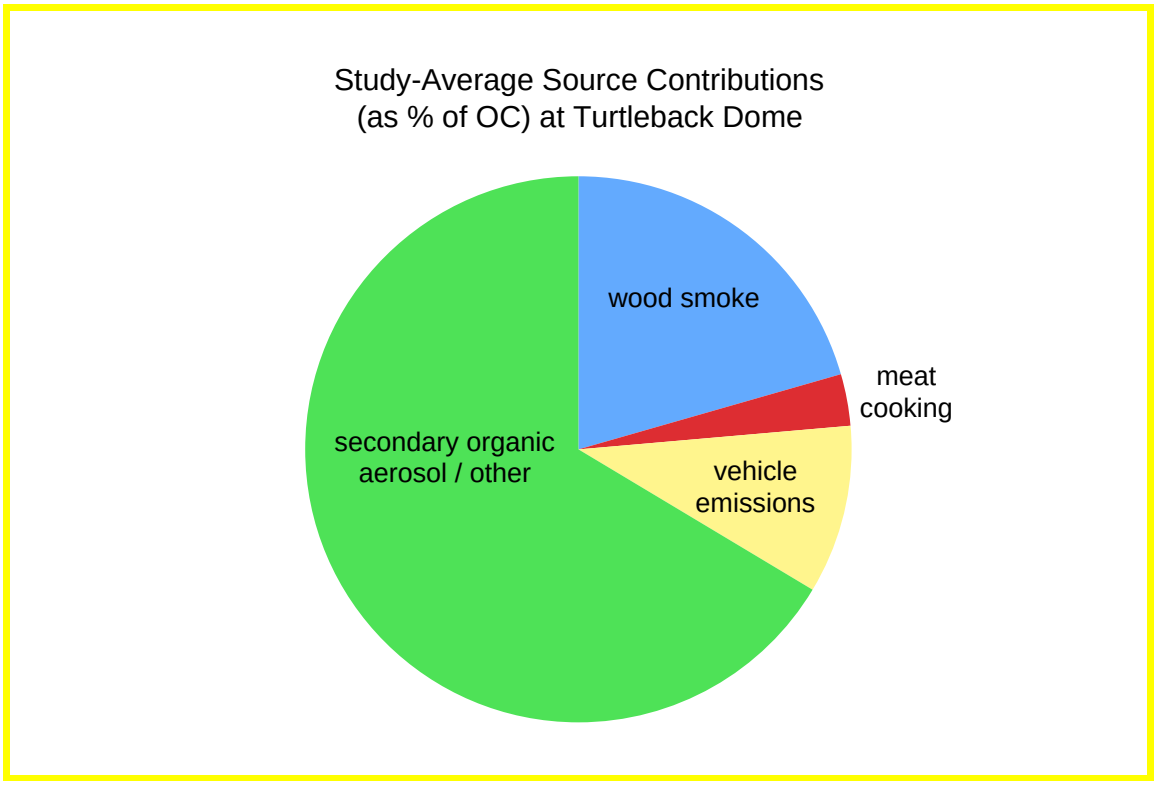

Figure 1.6 Study-averaged source contributions of fine aerosol organic carbon (expressed as % of OC) at Turtleback Dome.

PREFACE, DISCLAIMER AND ACKNOWLEDGMENTS

This report is a collaborative effort involving the listed authors and many other individuals. The authors gratefully acknowledge Mr. John Molenar, Dr. David Dietrich, and the staff of Air Resource Specialists, Inc., for their contributions to managing the field campaign. The authors also gratefully acknowledge Yosemite National Park and, in particular, the assistance of Russell Galipeau and Katy Warner. We also thank Drs. Lowell Ashbaugh, Charles McDade, and Thomas Cahill from the University of California at Davis for their assistance.

The National Park Service supported this research (cooperative agreement #CA238099001 TO0356). This report is a work prepared for the Cooperative Institute for Research in the Atmosphere.

2. ***TABLE OF CONTENTS***

3. ***LIST OF TABLES***

4. ***LIST OF FIGURES***

5. ***INTRODUCTION***

5.1 Wildland Fires in Class I Visibility Areas: The Need for an Integrated Visibility and Land Management Strategy

A complex relationship exists between humans, the natural ecosystem, air quality, and the role of wildland fires [*MacCleery*, 1992]. Wildland fires include both naturally initiated wildfires and prescribed burns that are deliberately set by humans for land management practices. Over the last century, fire management on public lands has evolved into a formal public policy with specific guidelines and regulations [*Pyne*, 1997a]. Over that time period an evolution of attitude and priorities regarding fire has also occurred. In 1913 Chief Forester Henry Graves stated, "The necessity of preventing losses from forest fires requires no discussion. It is the fundamental obligation of the Forest Service and takes precedence over all other duties and activities." Similarly, Chief Forester William Greeley (1920–1928) stated, "The conviction burned into me that fire prevention is the number one job of American foresters...(p. 268)" [*Pyne*, 1997b]. These attitudes have transformed over time as awareness of the role fire plays in the development and sustainability of healthy, natural ecosystems has become better understood.

Fire suppression efforts over the past century in the United States have simultaneously allowed extreme fuel build-up and have threatened forest health. As seen with the 1988 Yellowstone National Park fires, naturally occurring fires result in unacceptable threats to human life and natural and cultural resources. A pictorial example of Yosemite Valley from a century ago illustrates some of the changes, e.g., much denser forest regions, that have occurred both at Yosemite and throughout the western United States (Figure 5.1). While unnatural fuel buildup presents problems, especially in rapidly growing urban interface areas throughout the West, forest health may be at even greater risk. Fire exclusion allows insect and disease ecosystem components to gain ground, which in turn can lead to the risk of more catastrophic fires [*Pyne*, 1997b]. For these reasons, federal land managers have, in recent years, joined together with local governments to develop a coordinated wildland fire policy. Protection of human life remains the first priority, while protection of property and natural and cultural resources are jointly a second priority. At the same time, wildland fire, as a critical natural process, must be reintroduced into the ecosystem based upon the best available science. For example, in Yosemite, the use of prescribed burns has increased over the past several decades in order to address the increasing

amount of large, destructive wildfires (Figure 5.2). Both controlled and wild fires have air quality impacts in the local environment and can contribute to regional haze.

The U.S. Environmental Protection Agency (EPA) promulgated the Regional Haze Rule that mandates improvements in visibility to "natural conditions" over an approximately 60-year period in 156 Class I national parks and wilderness areas [*United States Environmental Protection Agency*, 1999]. The Regional Haze Rule relates directly to forest and agriculture burning, and both air resource and land managers will be affected by the regulations. The rule impacts area sources such as wildland fires to the same extent that industrial and mobile sources have faced regulation over the past several decades. In addition, these regulations come at a time when public and private land managers are planning increased application of fire as a management tool. Prescribed fire will remain viable as a tool for land managers, but only under a comprehensive fire and smoke management strategy. This strategy will include formal "state-approved" smoke management programs and will require the use of new and "approved" technologies that have been subjected to public and stakeholder scrutiny. These programs must also acknowledge that wildland fire is much different from conventional human-caused air pollution sources [*Riebau and Fox*, 2001].

Figure 5.1 Yosemite Valley as it looked in 1899 with large expanses of open meadow and few cedar and pine trees, and currently (http://www.nps.gov/yose/fire/history.htm).

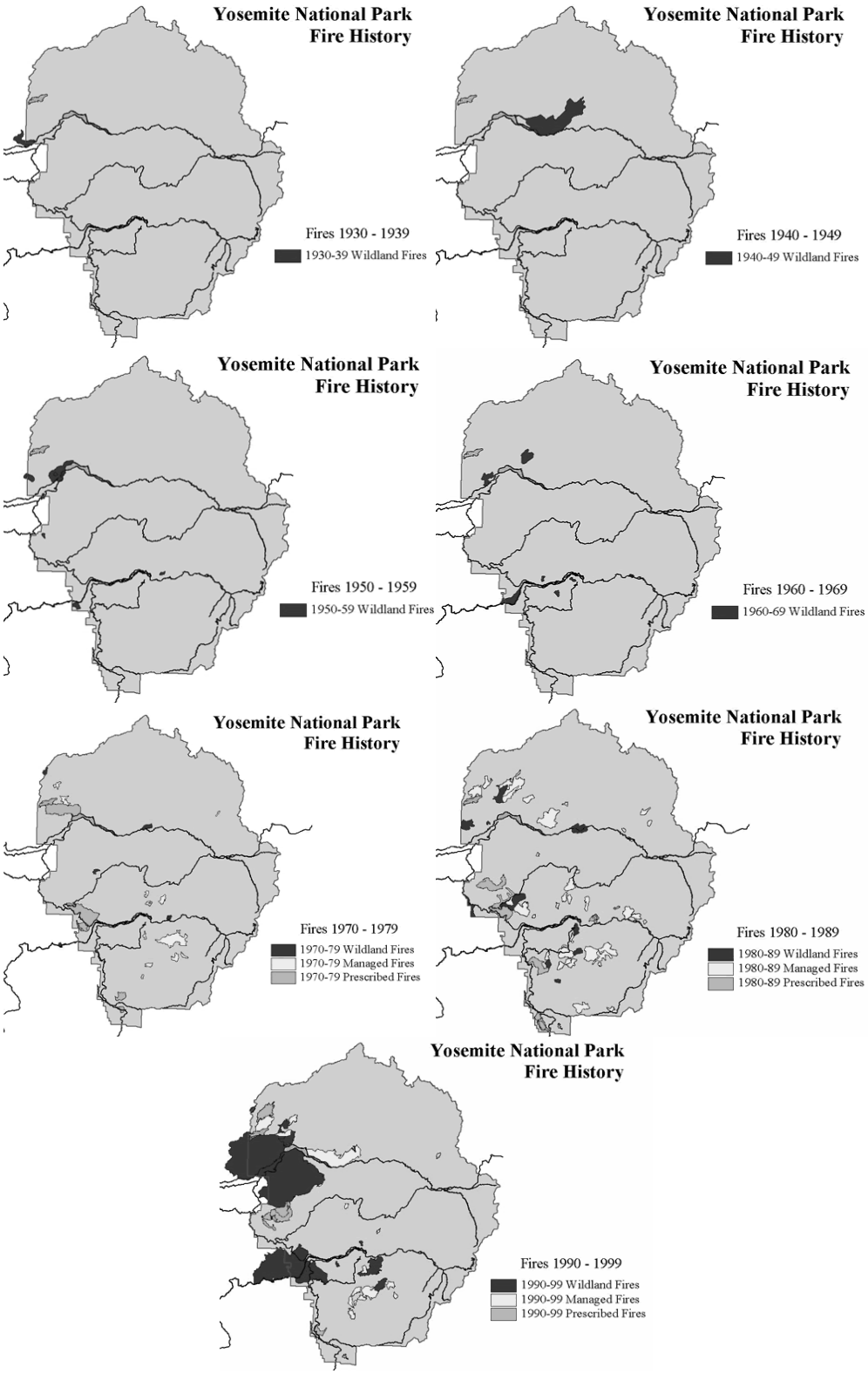

Figure 5.2 Fire history at Yosemite National Park (http://www.nps.gov/yose/fire/history.htm).

5.2 Carbonaceous Aerosol: Pyrogenic, Biogenic, and Anthropogenic Sources

The effects of particulate materials on atmospheric optics, and hence visibility, depend strongly on their physical characteristics and their chemical composition, which in turn are related to their sources. Particulate organic matter (POM, also abbreviated OCM for organic carbon mass) is of special interest due to its atmospheric abundance, complex speciation and the limited understanding of its composition, formation mechanisms, and optical properties [*Seinfeld and Pandis*, 1998]. POM is carbon bound to other elements like hydrogen, oxygen, nitrogen, etc., and is often composed of a myriad of chemical compounds ranging from alkanes, alkenes, carboxylic acids, sugars, alcohols, and aromatic compounds. The most often used analytical methods only quantify the carbon mass, termed organic carbon (OC), associated with POM. Carbonaceous aerosol also comprises elemental carbon (EC), or carbon in a relatively pure elemental state, to a lesser extent typically [*Seinfeld and Pandis*, 1998]. Depending on the measurement technique, EC may be referred to as "light-absorbing carbon", "black carbon", or "graphitic carbon", all of which are similar entities, though operationally defined based on the method of evaluation.

POM has a diversity of primary and secondary sources including natural and human as delineated in Figure 5.3. Broadly, POM sources may be categorized into anthropogenic (human generated), biogenic (due to biological activity), and pyrogenic (resulting from open combustion of biomass). Anthropogenic sources often have a substantial contribution from fossil fuel burning, though they include a wide variety of sources including vehicle, power generation, agricultural, and industrial emissions. POM also has substantial contributions from natural biogenic sources. For example, $PM_{2.5}$ averaged 2.6 μgm^{-3} and was found to be approximately 80% POM in a natural forest environment in Amazonia during the wet season when burning or human influences are minimal [*Graham et al.*, 2003]. Pyrogenic sources may be considered as either biogenic or anthropogenic (wildfires versus prescribed burns). However, for these purposes, pyrogenic sources are grouped together due to the difficulty in distinguishing between POM from prescribed burns or wildfires.

A study of global emissions concluded that biomass burning emissions during the 1980s were of the same magnitude as those from fossil fuels on a global basis [*Andreae and Merlet*, 2001]. Globally, pyrogenic sources contribute as much as 85 Tg yr^{-1} of aerosol mass to the atmosphere [*Formenti et al.*, 2003]. A majority of this particulate material from biomass burning is typically POM. As a result, much interest has developed in studying the properties of biomass smoke and

its impact on atmospheric chemistry and air quality [*Andreae and Crutzen*, 1997; *Wotawa and Trainer*, 2000; *Andreae and Merlet*, 2001; *Kreidenweis et al.*, 2001]. Pyrogenic aerosols are important to visibility degradation, affect aquatic ecosystems and terrestrial vegetation, and potentially have human health consequences from air toxins [*McKenzie et al.*, 1995; *Riebau and Fox*, 2001]. Smoke is relevant to climate in addition to visibility in terms of direct impacts on radiative transfer and changes in cloud lifetime and albedo, causing, for example, nonprecipitating clouds with smaller droplets [*Penner et al.*, 1992; *Hobbs et al.*, 1997; *Iacobellis et al.*, 1999; *Rosenfeld*, 2000].

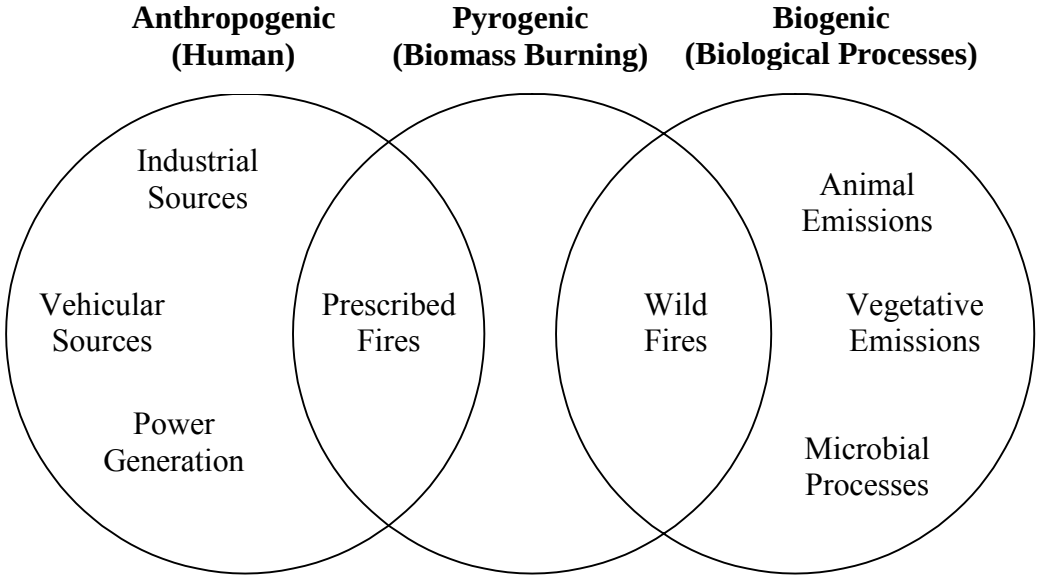

Figure 5.3 Grouping of POM source categories, each of which may contribute primary (directly emitted) and secondary (formed in the atmosphere from precursor emissions) aerosol.

The effects of POM aerosols and a concern for human health, climate, and visibility, have made them the subject of recent research and regulation [*Chung and Seinfeld*, 2002]. The EPA's Regional Haze Rule is intimately connected to the issues associated with POM and biomass burning. For example, the complex composition of POM and the difficulty in distinguishing between natural and anthropogenic sources makes determining "background visibility conditions" challenging. As described in the Regional Haze Guidance document, the EPA suggests default value concentrations of 0.02 μg m^{-3} and 0.47 μg m^{-3} for natural EC and OC in the western United States [*United States Environmental Protection Agency*, 2003a, 2003b]. A modeling study at several IMPROVE sites using a fire emissions database and a best estimate of biogenic emissions estimated that natural EC and OC concentrations were 2–3 times higher than EPA default values

in most locations [*Park et al.*, 2003]. The larger background translates to ~ 20% decreased "natural visibility" as compared with EPA estimates [*Park et al.*, 2003]. As are fire emissions, smoke contributions to regional haze and visibility impacts in national parks are large and highly variable [*Malm et al.*, 1994; *GCVTC*, 1996, 1999; *Ames et al.*, 2004; *Malm et al.*, 2004]. Past studies have implicated smoke as a primary contributor to large $PM_{2.5}$ episodes, particularly in western U.S. parks, with contributions ranging from <10 to >70%, strongly dependent on season, region, and episodic fire occurrence [*Ames and Malm*, 2001; *Ames et al.*, 2004].

5.3 Historical Yosemite Aerosol Properties from IMPROVE Network Measurements

The national monitoring program developed to monitor long term trends in visibility and to implement the regional haze regulations is the Interagency Monitoring of Protected Visual Environments (IMPROVE) program. Long-term IMPROVE measurements show high concentrations of POM in western U.S. parks, and anecdotal observations have suggested that these are particularly impacted by smoke from wildland fires (Figure 5.4, Table 5.1) [*Malm et al.*, 1994; *Ames et al.*, 2004; *Malm et al.*, 2004]. Likewise, models suggest that pyrogenic and biogenic sources dominate POM in this region, particularly in summer [*Park et al.*, 2003]. For these reasons, the relationship between POM, smoke from biomass burning, and effects on visibility and air quality are vital issues for western parks. Inland national parks of California such as Sequoia, Joshua Tree, Yosemite, and others are typically the most air quality impacted parks in the western U.S., thought in part due to potential smoke influence and their downwind location from major population and agro-industrial centers [*Sullivan et al.*, 2001]. SO_2 emissions are generally low in California; industrial, energy, and transportation sectors are substantial sources of nitrogen oxides (NOx) and volatile organic carbon (VOC), though these have generally declined in urban California overall during the past 20 years. Nonetheless, Yosemite has demonstrated substantial damage to flora linked to ozone [*Sullivan et al.*, 2001] as summer O_3 often exceeds the California one-hour standard of 95 ppb, including in 2002 (http://www.arb.ca.gov/adam/welcome.html). Furthermore, regions such as the San Joaquin valley of California have experienced rapid development and population growth, potentially impacting the park [*Sullivan et al.*, 2001].

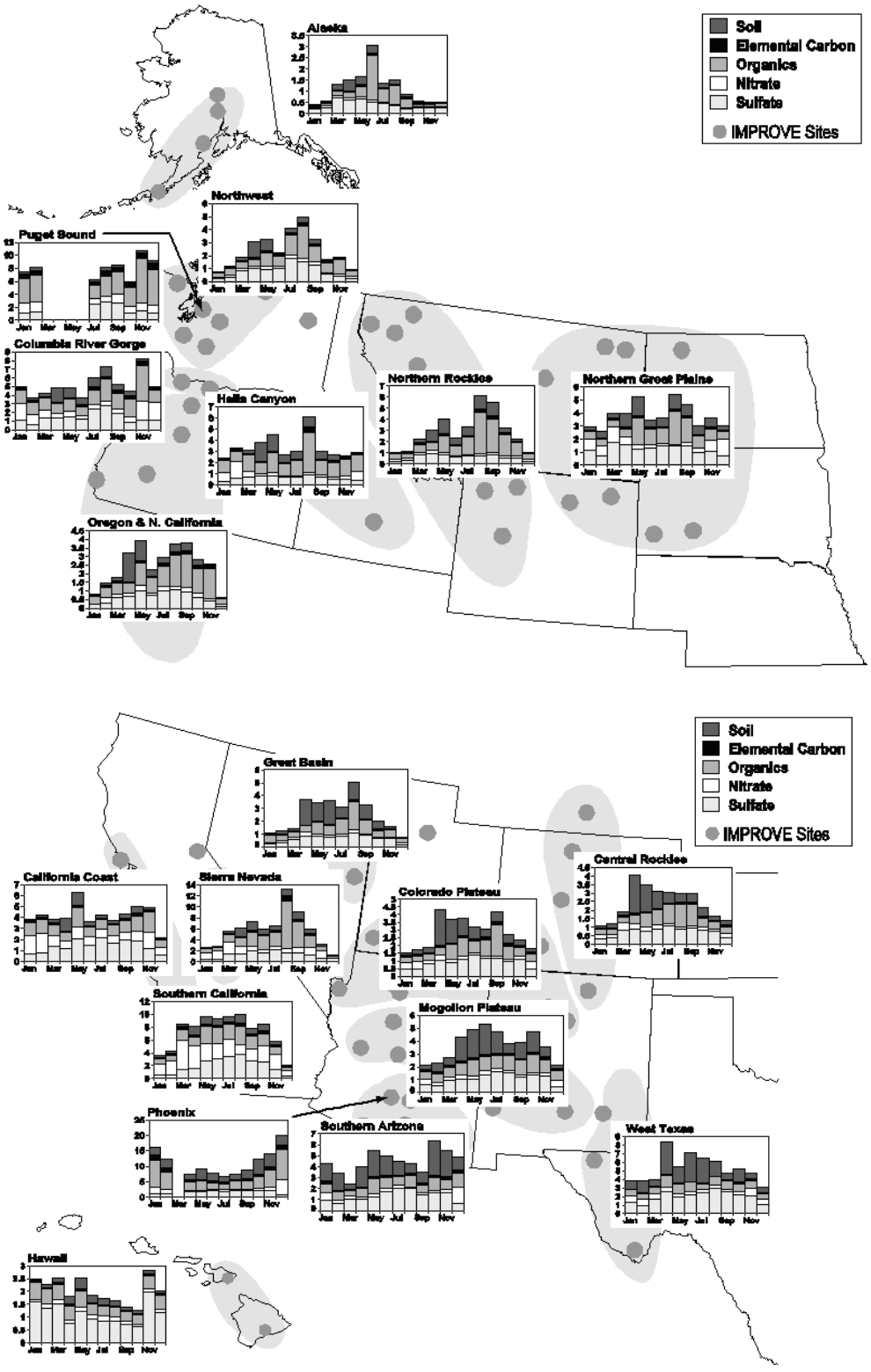

Figure 5.4 Map showing stacked bar charts of monthly distributions of $PM_{2.5}$ aerosol species for the western United States from IMPROVE network measurements. Starting from the base of the chart ammonium sulfate and nitrate, POM (organics), light-absorbing (elemental) carbon, and soil are shown. Note the large contribution of POM during summer in many western parks.

Table 5.1 Summary of historical Yosemite summer aerosol properties (15 July through 5 September, 1988–2003). POM assumes a POM/OC multiplier of 1.8 as found in the Yosemite Aerosol Characterization Study (YACS) in 2002. Extinction coefficient (b_{ext}) is reconstructed from aerosol components (http://vista.cira.colostate.edu/improve/Data/IMPROVE/AsciiData.aspx).

YOSE Summer Historical (1988-2003)					
	Mean	**Std Dev**	**Min**	**Max**	**N**
b_{ext} (Mm^{-1})	33.32	16.04	12	116	1470
PM_{10}	15.85	13.97	5.62	164.64	1566
$PM_{2.5}$	8.37	4.91	0.00	40.33	1560
POM*	6.41	9.53	1.33	96.98	1681
EC	0.52	0.72	0.09	7.56	1559
SO_4^{2-}	1.22	0.46	0.36	2.80	1565
NO_3^-	0.35	0.29	0.05	2.46	1588
K	0.06	0.03	0.01	0.18	1589
SOIL	0.73	0.30	0.12	2.24	1586

* Average POM decreases to 5.4 ± 4.8 μgm^{-3} excluding 2001 when POM reached 97 μgm^{-3} with probable local fire impact

IMPROVE measurements have demonstrated that air quality in western national parks including Yosemite is strongly impacted by POM (Table 5.1) [*Malm et al.*, 1994; *Ames et al.*, 2004; *Malm et al.*, 2004]. Many eastern U.S. parks have shown marked improvement in air quality indicators such as SO_4^{2-} concentrations, which constitute a large fraction of $PM_{2.5}$ in those parks and which have decreased in concert with decreased regional SO_2 emissions [*Malm et al.*, 2002]. In Yosemite, where POM continues to be the most important contributor, no improvement in visibility nor a significant trend was observed during the 1990s even though SO_4^{2-} decreased [*Sullivan et al.*, 2001]. Average $PM_{2.5}$ mass concentration at Yosemite peaks during the summer months and during summers of 1988–2003 averaged 8.4 μgm^{-3} (Table 5.1). On the average, carbonaceous material contributes well over half of the fine aerosol (or $PM_{2.5}$ for these purposes, i.e., particles with aerodynamic diameters $D_p < 2.5$ μm) (Figure 5.5, Table 5.1) and during autumn that fraction can exceed 80% [*Malm et al.*, 2004]. Historically at Yosemite, the total light extinction coefficient also peaks in the summer. The average transmissometer light extinction coefficient was 33 Mm^{-1} during the summers of 1988–2003, with half of the light extinction estimated from POM (Table 5.1).

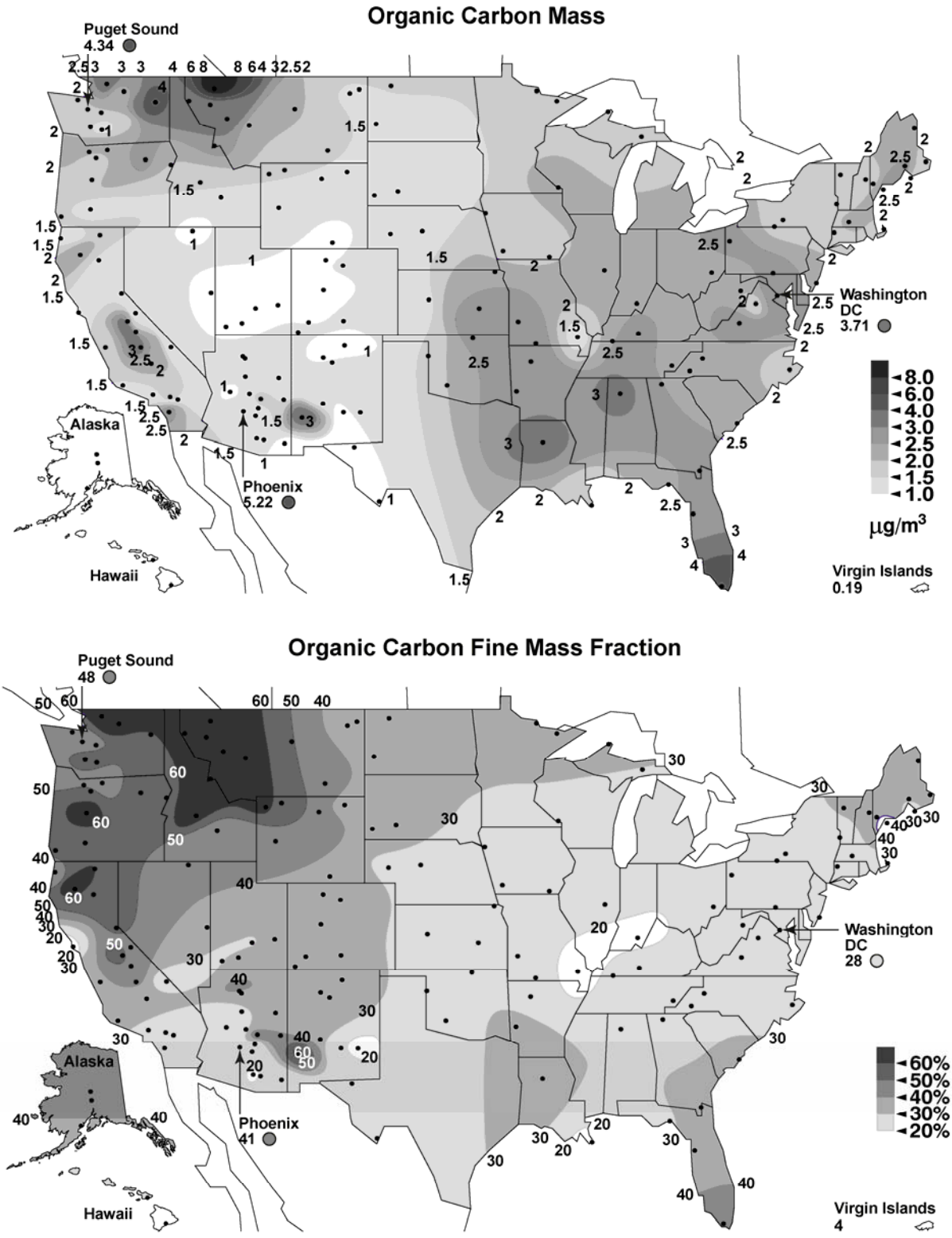

Figure 5.5 Contour map of organic carbon concentrations (POM/1.4) and percentage of $PM_{2.5}$ from IMPROVE network data (http://vista.cira.colostate.edu/IMPROVE/).

5.4 The Yosemite Aerosol Characterization Study: Scientific Questions

Atmospheric aerosols, natural and anthropogenic, alter atmospheric optical properties through light scattering and absorption [*Charlson et al.*, 1992; *Malm et al.*, 1996]. For several decades, physical and optical properties of inorganic aerosol components (particularly sulfates and nitrates) have been extensively studied [*Charlson et al.*, 1990]. Less, however, is known about carbonaceous aerosols, especially in relation to our nation's national parks and wilderness areas. Biomass smoke contains a large fraction of particulate organic material, and it plays a vital role in visibility degradation in Class I areas. Limited understanding, particularly of smoke impacts on visibility in western parks such as Yosemite, requires a detailed smoke emission inventory as well as better characterization of smoke aerosol properties [*Riebau and Fox*, 2001]. The Yosemite Aerosol Characterization Study (YACS) was implemented to better understand the properties of a carbon-dominated aerosol influenced by biomass smoke. The objectives can be broadly classified as (a) measurement of the fundamental properties of regional haze at Yosemite (e.g., PM concentrations, major chemical components, light extinction properties), (b) detailed characterization of aerosol physiochemical properties with high time resolution and other methods (e.g., aerosol size distribution, refractive index, aerosol hygroscopicity), (c) synthesis of measured aerosol physical and chemical properties into models for prediction of and comparison to measured light extinction properties, and (d) exploration of aerosol sources with airmass transport analysis, carbon isotopic analysis, and tracer species including organic carbon molecular marker techniques.

5.4.1 Measurement of Fundamental Aerosol Properties of Regional Haze at Yosemite

YACS was conceived to address this lack of knowledge regarding smoke aerosol properties and their impact on visibility in western U.S. parks. Therefore a primary goal of this research was to characterize the chemical, physical, and optical properties of a smoke-impacted regional aerosol. Current monitoring protocols are unable to accurately assess smoke contributions to haze in Class I areas due to limited information on smoke properties. A number of previous small studies have examined smoke properties in extra-tropical temperate forests [*Radke et al.*, 1991; *Martins et al.*, 1998; *Conny and Slater*, 2002]. However, most comprehensive previous studies of biomass smoke have typically focused on tropical regions, where 80% of global biomass-burning emissions occur [*Hao and Liu*, 1994]. For example, the Smoke, Clouds, and Radiation-Brazil (SCAR-B) and Southern Africa Regional Science Initiative (SAFARI) field projects examined

smoke influences on clouds and radiation over the Amazon and southern African rainforests [*Kaufman et al.*, 1998; *Haywood et al.*, 2003]. Recent smaller-scale field studies have also examined the properties of smoke and its effects on cloud properties from tropical biomass burning in Asia, Africa, and Central and South America [*Abel et al.*, 2003; *Ogunjobi et al.*, 2004].

Many of the most important parameters for determining the influence of POM from biomass burning on visibility in U.S. national parks are poorly characterized. Aerosol hygroscopicity (particle water uptake as a function of relative humidity), the ratio of POM to OC, POM mass scattering efficiencies, aerosol composition, microstructure (internal mixing characteristics), aerosol refractive index, and particle size distributions are all important parameters for assessing the role of smoke in reducing visibility.

The aerosol mass scattering efficiency allows estimates of visibility impacts based on mass concentration measurements of $PM_{2.5}$. This parameter, however, is uncertain due to variations in the physical and chemical state of POM, particularly those associated with smoke. Factors ranging from the size distribution, the mixing state of POM with other aerosol components, the index of refraction of POM, and the exact composition of the POM all contribute to the uncertainty in its optical properties. Nominal values of mass scattering efficiencies of 3.0 m^2/g and 4.0 m^2/g for sulfate and POM, respectively, have been adopted for tracking visibility changes and are used in IMPROVE network protocols [*United States Environmental Protection Agency*, 2003a, 2003b]. Based on numerous field studies, a wide range of dry mass scattering efficiencies for sulfates of 1.9 to 6.1 m^2/g and 1.3 to 7.0 m^2/g for POM has been observed [*Trijonis et al.*, 1990]. Based on mass size distribution measurements from several national parks, average summertime dry sulfate mass scattering efficiencies were found to vary from 2 to 3 [*Malm and Pitchford*, 1997]. Little data on mass scattering efficiencies for organic carbon aerosols have been reported, primarily because of the inability to accurately measure mass size distributions and other fundamental properties of organic carbon aerosols. Thus, one of the primary objectives of YACS was to investigate the mass scattering efficiency of POM and, particularly, of biomass smoke.

It is customary to estimate particulate organic material (POM) concentrations from measurements of organic carbon mass by multiplying a factor that is the ratio between average molecular weight and carbon weight. The OC to POM multiplication factor is a vital parameter in determining the contribution of POM to aerosol $PM_{2.5}$ and resulting visibility impacts. This factor is used to

convert the measured organic carbon mass (typically measured by thermal-optical techniques) to an equivalent POM mass concentration (which includes the elements bonded to carbon such as hydrogen, nitrogen, oxygen, etc.). Based on historical measurements, a factor of approximately of 1.2 to 1.4 has traditionally been used [*Turpin and Lim*, 2001]. Current IMPROVE protocols specify that this relationship is assumed to be [POM] = 1.4[OC], where OC is from the channel C IMPROVE filter measurement and determined by the thermal optical reflectance method (TOR) [*Chow et al.*, 1993]. Based on more recent laboratory and field measurements of various organic aerosol species, factors of ~ 1.6 and ~ 2.1 have been found more appropriate for an urban and an aged nonurban aerosol, respectively [*Turpin and Lim*, 2001]. This range of uncertainty in POM/OC from conversion factor 1.2 to 2.1 translates into a ± 27% uncertainty in POM mass concentration.

5.4.2 Evaluation of High Time Resolution Aerosol Measurement Techniques and Harmony Comparisons with Time-integrated Techniques

A further objective of YACS was to evaluate a variety of semi-continuous measurements in comparison to traditional time-integrated techniques, such as IMPROVE network filter samples. The self-consistency and overall quality of the aerosol measurements are assured by redundancy and intercomparisons between independently measured species [*Malm et al.*, 2005a]. In the most general sense, validation is a matter of comparing chemically related species that have been measured with different instrumentation at the same location and averaged over the same time period. Uncertainties for the 24-hour average filter-based measurements are better established than for semi-continuous measurements such as the particle-into-liquid (PILS) inorganic species and Rupprecht & Patashnick (R&P) carbon measurements or the micro-orifice uniform deposit impactor (MOUDI) derived ion mass concentrations. Therefore the bulk 24-hour samples will be used as "standards" against which these measurements are compared. Both additive and multiplicative biases are explored through simple correlation tables between concentrations measured using the various sampling systems and ordinary least squares (OLS) regression analysis [*Malm et al.*, 2005a].

The design of the IMPROVE sampler also allows for redundancy between module A measurements and modules B and C measurements of the ions and carbons, enabling quality control checks. For example, elemental sulfur mass times three should agree with the sulfate ion measured in module B. However, when comparing measured fine mass to reconstructed fine mass

(RCFM), two complicating factors must be considered. First, under some conditions, a large portion of the nitrates can volatilize from the module A Teflon® filter. Secondly, because of water retention by soluble aerosol species, the amount of residual water on the filter is a function of the relative humidity at which the filter is weighed and the relative humidity (RH) history to which the collected aerosol was exposed. Both positive and negative artifacts can also be observed with POM aerosol due to volatility issues [*Huebert and Charlson*, 2000].

High time resolution measurements can provide insights into aerosol properties not afforded by time-integrated, filter-based samplers. For example, with high time resolution techniques we are able to explore the associations of various chemical constituents and look at their probable molecular forms. Aerosol phase nitrate (NO_3^-) is often an important, though volatile, component of the ambient aerosol, subject to measurement artifacts. Nitric acid (HNO_3), the major oxidation product of NOx, and ammonia (NH_3), emitted from animal waste, use of fertilizers, and bacteria are prevalent atmospheric gases. The two species react to form particulate ammonium nitrate (NH_4NO_3) by gas-to-particle conversion. This is most typically part of the fine mode of the aerosol [*Richardson and Hightower*, 1987] and is assumed to be so under IMPROVE protocols. However, nitrate may exist in other forms; for example, HNO_3 in the presence of sea salt (mainly NaCl) or soil dust ($CaCO_3$) can react with these relatively alkaline materials [*Prospero and Savoie*, 1989]. These species typically reside in the coarse mode of the particle size distribution. The chemical form, hygroscopicity, and size distribution of NO_3^- are all important factors that relate to visibility, and hence this was a species of particular interest during YACS.

5.4.3 Determination of Detailed Aerosol Microphysical, Chemical, and Optical Properties

Previous lab, field, and modeling studies show atmospheric light extinction is often critically dependent on aerosol phase water [*Pilinis et al.*, 1995; *Malm and Kreidenweis*, 1997; *Malm et al.*, 2003]. Overall, hygroscopic properties of inorganic species have been investigated much more thoroughly than those of organic aerosols. Lab studies of water uptake by mixtures of POM with inorganic salts generally have shown a lower deliquescence point and lower hygroscopicity for the mixtures than for pure salts such as NaCl and $(NH_4)_2SO_4$ [*Hansson et al.*, 1998; *Prenni et al.*, 2003; *Brooks et al.*, 2004]. This is particularly relevant for biomass smoke aerosols, often composed of POM mixed with small contributions of inorganic constituents. Nonetheless, some organic species uptake water, though the precise hygroscopic behavior of ambient POM is poorly characterized and appears to vary with POM source and composition [*Saxena and Hildemann*,

1996]. Moreover, as a result of the diversity of species that compose it, fresh versus aged POM likely behaves differently, as does POM from biomass burning versus an urban-industrial plume.

As particles grow with increasing RH, separation into "more" and "less" hygroscopic modes (and sometimes additional modes) is often observed, indicative of externally mixed particles [*Zhang et al.*, 1994]. A review of ambient hygroscopic growth measurements found a broad range of results for diameter (D) growth factors as a function of RH ($D(RH)/D_o$, where D_o is the particle diameter at low reference RH "dry" conditions). Typically, though, there was a less hygroscopic mode with $D(\text{high RH})/D_o$ of 1 to 1.4 and a more hygroscopic mode in the range of 1.1 to 1.8 for high RH in the range of 80–90%, depending on the study [*Cocker et al.*, 2001]. This same study, based in Pasadena, California, also found enhanced hygroscopic growth during periods influenced by nearby forest fires [*Cocker et al.*, 2001]. Aircraft measurements of smoke in South America have shown nearly hygrophobic aerosol in fresh smoke and modest enhancements in hygroscopicity as the smoke ages [*Kotchenruther and Hobbs*, 1998]. Likewise, models have invoked diverse assumptions ranging from the suppression of inorganic water uptake by the presence of POM to POM hygroscopicity equaling that of $(NH_4)_2SO_4$ [*Saxena et al.*, 1995; *Iacobellis et al.*, 1999; *Malm and Day*, 2001; *Markowicz et al.*, 2003]. For instance, regional modeling efforts assumed that 50% of POM associated with smoke was as hygroscopic as sulfate, thereby enhancing its light scattering by a factor of 4.2 at ambient RH = 90% [*GCVTC*, 1996, 1999]. As a consequence, if the smoke does not adsorb water, smoke's contribution to haze may be overestimated roughly by a factor of 2. The hygroscopic behavior of POM and particularly biomass smoke is an uncertain though key determinant in assessing the impact of POM on visibility.

Other aerosol microphysical properties are important contributors to visibility degradation. Among these are the aerosol refractive index and the relative contributions of OC and EC to carbonaceous aerosols. As it relates to the refractive index of smoke, OC is typically assumed to be a pure scattering medium, while EC both scatters and absorbs visible light and thus has a complex index of refraction with both scattering (real part) and absorption (imaginary part). This study employed several methods to determine EC and OC. A distinct difference between the contribution of EC to total carbon (TC) has been observed in comparing POM source categories, e.g., urban-industrial versus biomass burning, with 10% contributions of EC to carbon mass from wood combustion [*McDonald et al.*, 2000] and 30–60% contributions of EC from urban sources [*Moosmuller et al.*, 2001; *Carrico et al.*, 2003a]. This is understandably a coarse distinction

between source categories and does not differentiate wildfires, prescribed fires, agricultural burning, and other biogenic sources from anthropogenic sources [*Ames et al.*, 2004].

Additionally, based on comparing complementary particle sizing methods, the real part of the aerosol refractive index can be retrieved [*Hand and Kreidenweis*, 2002; *McMeeking et al.*, 2005a]. This is important as the POM fraction of the aerosol is typically composed of a myriad of species, and methods of determining the totality of these are still developing. The aerosol mixing characteristics also impact the refractive index and the optical properties. The two extremes are pure external and pure internal mixtures of the various chemical constituents of the aerosol. Using particle-imaging techniques, the mixing state of individual particles collected during YACS is explored [*Laskin and Cowin*, 2001; *Laskin et al.*, 2003; *Hand et al.*, 2005]. These aerosol properties all contribute to determining the mass scattering and absorption efficiencies of the aerosol and ultimately their impacts on visibility.

Another goal of YACS is exploring the nature, speciation, and probable sources of carbonaceous aerosol. This includes distinguishing between biogenic, pyrogenic, and anthropogenic sources of aerosols and examining primary versus secondary aerosols. The composition of POM is often a complex mixture of compounds including alkanes, alkenes, alcohols, organic acids, aromatic compounds such as terpenes, and numerous other categories [*Seinfeld and Pandis*, 1998]. Even comprehensive measurements of carbon-containing compounds typically identify a minority of the mass of the organic species [*Rogge et al.*, 1993]. Two of the priorities of YACS thus were to speciate the composition of POM and to explore marker species for source categories such as pyrogenic, biogenic, and anthropogenic contributors.

6. ***OVERVIEW OF EXPERIMENTAL METHODS***

6.1 Sampling Sites Description

Yosemite National Park is located in the central Sierra Nevada mountain range. It was one of the first national parks set aside as a public trust in 1864 and was established as a national park in 1890. Yosemite features a rich ecological and cultural legacy, and it remains one of the most visited parks in the national park system, hosting approximately 3.3 million visitors in 2002 (http://www.nps.gov/yose/). Yosemite has incomparable scenic landscapes and sensitive ecosystems as, for example, it contains lakes very sensitive to acidification from nitrogen and

sulfur deposition. Located approximately 200 km east of San Francisco and being downwind of the San Joaquin valley, Yosemite is susceptible to air pollution impacts from these regions. Observed effects include foliar damage due to ozone and episodic visibility degradation [*Sullivan et al.*, 2001].

The majority of measurements during YACS were made on Turtleback Dome (37.71° North, 119.70° West, 1615 m above sea level) (Figure 6.1). High-volume, filter-based particulate samplers were located on the rocky dome itself at Turtleback, which is also the location of the standard IMPROVE sampling system. Most other instrumentation was located in three research trailers that were set back ~ 100 m from the dome at approximately the same elevation. Near the trailers, a scaffolding supported a second set of IMPROVE samplers and several other samplers including URG filter samplers. A subset of measurements were taken using IMPROVE and high-volume samplers that were located in Yosemite Valley (37.75° North; 119.59° West; 1213 m ASL). The measurement campaign took place between 15 July 2002 and 5 September 2002. "Intensive" periods were defined based on several observations in the field, including elevated carbon concentrations, enhanced ultraviolet (UV) absorption from the dual-channel aethalometer, and visually observed haze at the sampling site. These periods featured more frequent filter changes and shorter sampling periods for the time-integrated measurements. The two intensive sampling periods were 28–31 July and 14–16 August 2002. Aerosol physical, chemical, and optical properties were characterized using the samplers and instruments described below.

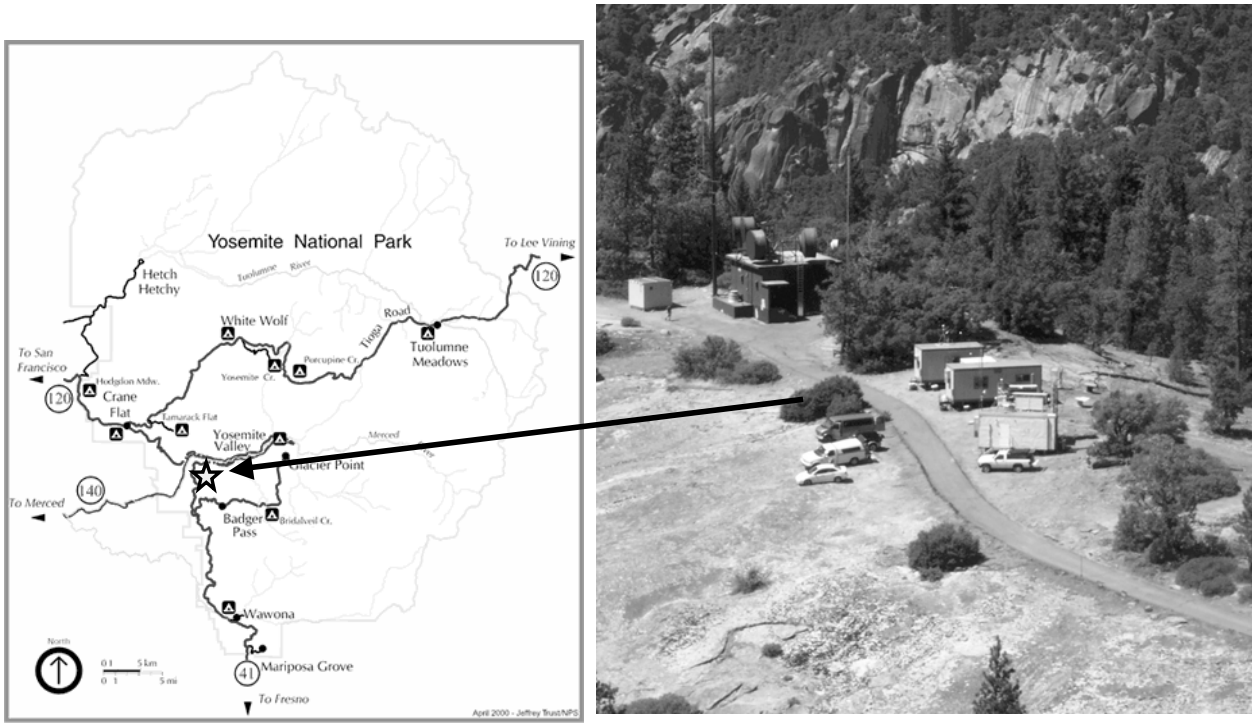

Figure 6.1 Location and photo of Turtleback Dome sampling site at Yosemite National Park.

6.2 Aerosol Chemical Composition

Aerosol chemical composition during YACS was characterized using several samplers operated in sample collection periods ranging from 5 minutes to 48 hours. Fine aerosol ($PM_{2.5}$ or particles with aerodynamic diameters $D_p < 2.5$ μm), total aerosol (PM_{10} or particles with $D_p < 10$ μm), OC, inorganic compounds, EC, and various elemental concentrations were measured during the study. A brief description of the techniques is given below and summarized in Table 6.1 and Table 6.2. More detailed experimental protocols can be found in referenced manuscripts.

The IMPROVE network filter sampler has been operated extensively as part of the ongoing IMPROVE monitoring network since 1987 (Figure 6.2) [*Malm et al.*, 1994; *Malm et al.*, 2004] (http://vista.cira.colostate.edu/improve/Publications/SOPs/). Each of four independent modules incorporates a separate inlet, filter pack with four filters and manifold, and pump assembly all microprocessor-controlled (Figure 6.3). Modules A, B, and C have a $PM_{2.5}$ cyclone, while Module D has a PM_{10} inlet. Module A is analyzed for fine mass ($PM_{2.5}$) gravimetrically, for elements with 11 < atomic number < 82 (from Na to Pb) by x-ray florescence (XRF), for elemental hydrogen by proton elastic scattering analysis (PESA), and for light absorption. Module B, preceded by a carbonate denuder to remove gaseous nitrates, is analyzed by ion

chromatography for sulfate, nitrate, nitrite, and chloride. Module C utilizes tandem quartz fiber filters where the front filter is analyzed for particulate organic and elemental carbon using thermal optical reflectance (TOR) [*Chow et al.*, 1993]. The second filter is used for an estimation of the artifact from adsorbed organic gases. Finally, module D utilizes a Teflon® filter that is gravimetrically analyzed for PM_{10} mass concentration. During YACS, three sets of IMPROVE samplers were operated, two on Turtleback Dome and one at the Yosemite Valley visitor center. IMPROVE samplers at Turtleback Dome and at Yosemite Valley were operated with a $PM_{2.5}$ size cut while a second sampler at Turtleback Dome was operated with a PM_{10} size cut.

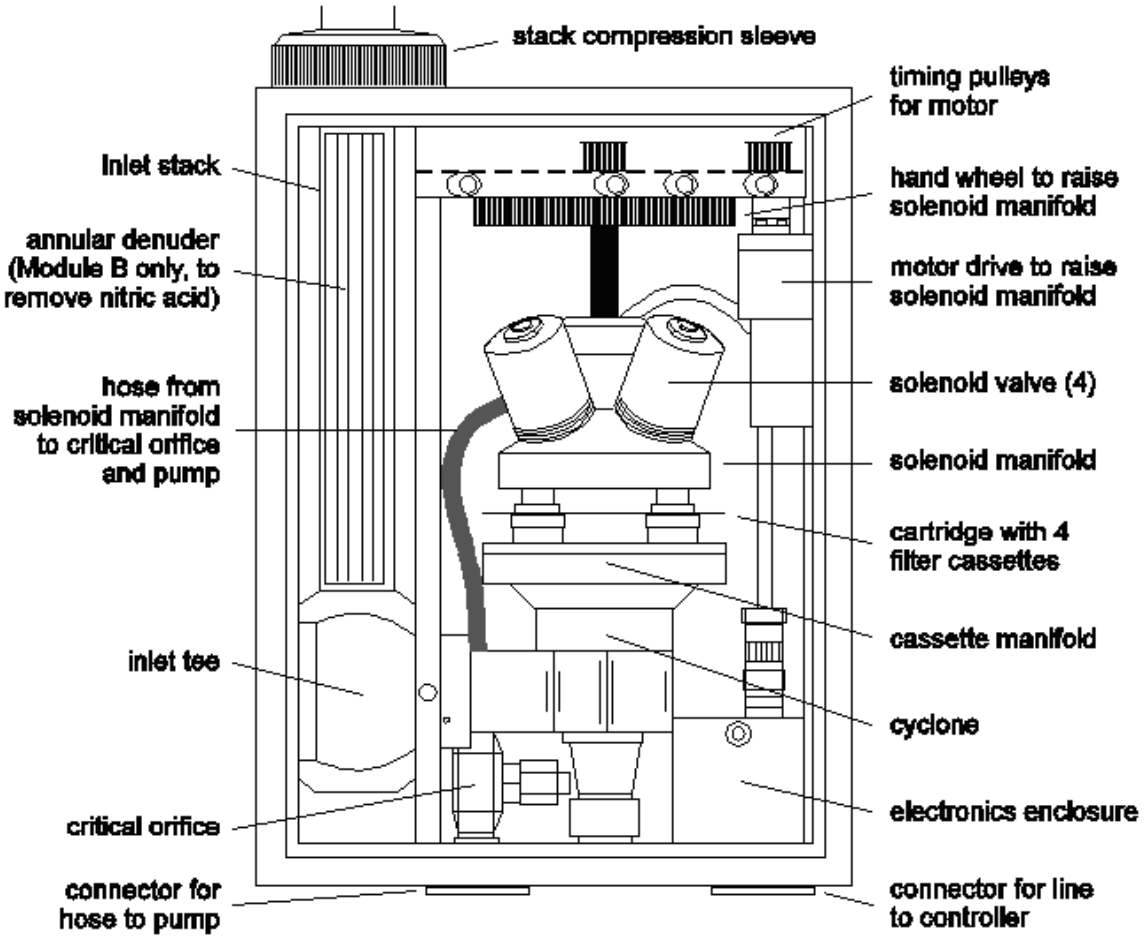

Figure 6.2 Schematic of a new version of the IMPROVE sampler $PM_{2.5}$ module used during YACS.

Figure 6.3 Outdoor sampling platform for URG filter samplers and IMPROVE network samplers.

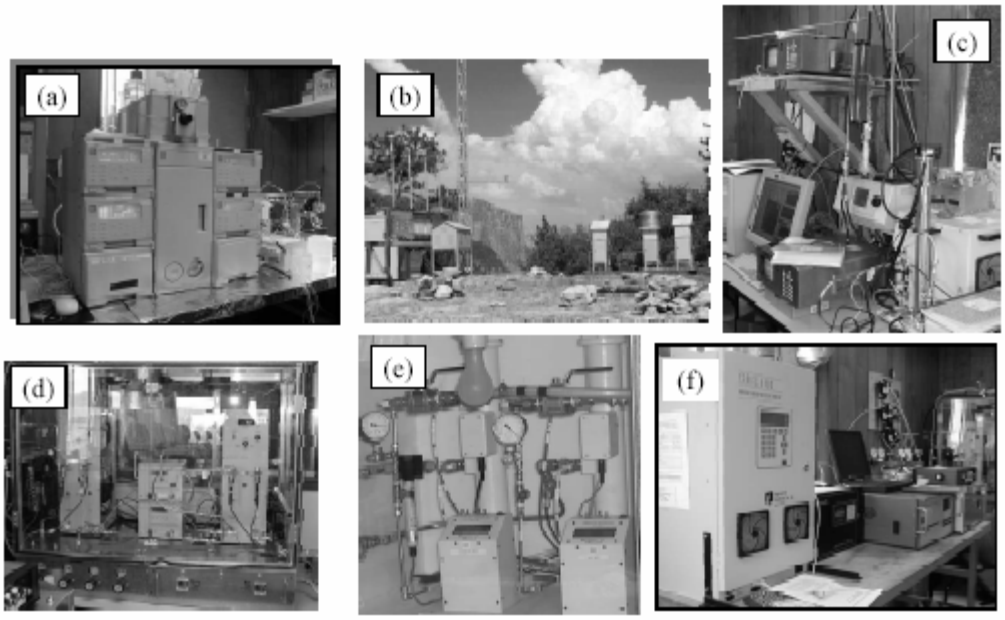

Figure 6.4 Instrumentation used for measurements during YACS including (a) particle-into-liquid (PILS) high time resolution ionic composition, (b) high-volume filter samplers for organic carbon speciation, (c) particle sizing instrumentation, (d) particle diameter growth measurements, (e) light scattering growth measurements, and (f) high time resolution carbon measurements.

Another $PM_{2.5}$ filter collection system (URG, Inc.), located on the sample scaffolding during YACS, consisted of a 2.5 μm cyclone, two denuders to remove nitric acid and ammonia gas, a Teflon® primary filter for particle collection, and nylon backup filter to collect any nitrate that escaped from the primary filter [*Lee et al.*, 2004] (Figure 6.3). Filter extracts were analyzed by

ion chromatography (Dionex DX-500) for major ions including SO_4^{2-}, NO_3^-, Cl^-, Na^+, K^+, Ca^{2+}, Mg^{2+}, NH_4^+, and oxalate. Extracts from the two denuders were analyzed to obtain HNO_3 and NH_3 gas phase concentrations. Typically, daily filter samples were collected for 24 hours beginning at 0800 local time (six-hour samples during intensive periods).

A particle into liquid/ion chromatography system (PILS/IC) took high time resolution (15-minute) semi-continuous measurements of $PM_{2.5}$ major ions (Figure 6.4) [*Weber et al.*, 2001]. Ambient air was drawn through a cyclone (D_{50} = 2.5 μm) and two denuders to remove acidic and basic gases. The PILS collects particles by introducing them into an environment of 100°C steam and impacting the grown droplets into an aqueous solution formed by a small continuous flow of high purity water. The collected sample liquid is then analyzed every 15 minutes by ion chromatography for major ions.

A cascade impactor (MOUDI) collected particles into discrete size ranges with multiple stages [*Marple et al.*, 1991]. The eight main impaction stages of the MOUDI collected particles onto silicone-coated aluminum substrates in the following aerodynamic diameter size ranges: (stage 1) 18–10 μm, (stage 2) 10–5.6 μm, (stage 3) 5.6–3.2 μm, (stage 4) 3.2–1.8 μm, (stage 5) 1.8–1.0 μm, (stage 6) 1.0–0.56 μm, (stage 7) 0.56–0.32 μm, and (stage 8) 0.32–0.18 μm. The MOUDI also included an after-filter to collect particles $D_p < 0.18$ μm and an initial greased cup stage for particles $D_p > 18$ μm. During YACS, aerosol samples were collected for 24 hours (12 hours during intensives). Laboratory analyses of sample extracts were done by ion chromatography for major anions (SO_4^{2-}, NO_3^-, Cl^-) and major cations (NH_4^+, Na^+, Ca^{2+}, K^+) [*Lee et al.*, 2004].

A two-channel aethalometer preceded by a 2.5 μm size cut cyclone measured aerosol black carbon (BC) concentration at wavelengths of 350 and 880 nm [*Hansen et al.*, 1984]. With a five-minute sample frequency, the instrument measured attenuation of a light beam through an aerosol sample collected on quartz fiber filter tape. While the 880nm channel is sensitive to BC, the UV channel also responds to absorption by certain organic compounds that are found in wood smoke or diesel exhaust. Thus a divergence of the two channels with increased short wavelength absorption indicates the presence of wood smoke or diesel exhaust.

A Rupprecht and Patashnick model 5400 Ambient Carbon Particulate Monitor [*Rupprecht et al.*, 1995] was used to measure hourly aerosol total carbon (TC). The instrument collects sample aerosol on one of two stainless steel impactor plates. After sample collection, the impactor plate is

heated to 750°C in air and the CO_2 evolved is measured with a Li-Cor sensor. Sampling and heating are alternated between two parallel impactors. A 2.5 μm size cut inlet preceded the sample line, while the minimum size cut for the impactors is 0.14 μm with a flow of 16.7 lpm.

High-volume, filter-based samplers were used to collect $PM_{2.5}$ on pre-fired quartz fiber filters, while accelerator mass spectrometry was used to measure carbon isotopic ratios [*Bench and Herckes*, 2004]. Measurement of the $^{14}C/^{12}C$ ratio of $PM_{2.5}$ allows apportionment of POM to contemporary (biogenic, pyrogenic) and fossil carbon (anthropogenic) using a two-component model. Carbon with ratios similar to the present atmospheric $^{14}C/^{12}C$ level is considered "contemporary carbon". It is primarily biogenic or pyrogenic in origin from plant biological activity or wildland fires, respectively. In contrast, carbon from the burning of fossil fuels was sequestered underground for periods much longer than the 5730-year half-life of ^{14}C and hence is radiocarbon-free. Other sources of carbon can arise from carbonate dust and soil organics, and the method presumes that these contributions are small. In most cases, a 12-hour sampling period (during daytime upslope flow conditions) was repeated on the same quartz filter for three consecutive days for a total sampling of 36 hours. However, during intensive periods quartz filters were changed every 1–2 days.

Samples were also collected using high-volume filter samplers equipped with a $PM_{2.5}$ impactor to examine POM composition, trace species content, and explore markers for wood smoke [*Engling et al.*, 2005]. Levoglucosan, a combustion product of cellulose thought to be stable against degradation in the atmosphere, is one candidate tracer for woodsmoke influence [*Simoneit et al.*, 1999]. Particle size distributions of selected organic species were determined using a second collector equipped with a six-stage cascade impaction inlet. The six stages of the cascade impactor correspond to the following aerodynamic particle diameter ranges: < 0.49 μm; 0.49–0.95 μm; 0.95–1.5 μm; 1.5–3.0 μm; 3.0–7.2 μm; > 7.2 μm. A third hi-vol sampler equipped with a PM_{10} inlet was located in Yosemite Valley. Samples were collected on pre-fired quartz fiber filters with sampling times of 12, 24, or 72 hours, typically beginning at 0800 local time. Weekly composite samples were analyzed using gas chromatography-mass spectrometry [*Brown et al.*, 2002; *Engling et al.*, 2005].

6.3 Aerosol Physical, Optical, and Hygroscopic Properties

Several complementary instruments were used to measure the aerosol particle size distribution. Ambient aerosol was sampled through a roof inlet with a five-way flow splitter to deliver a common aerosol sample to the particle sizing instrumentation located in an air-conditioned trailer on Turtleback Dome. To reduce uncertainties in particle sizing and intercomparisons due to variations in relative humidity (RH), the measurements were made at RH ~ 10%. Aerosol drying was accomplished using Nafion® membrane driers or heating (T ~ 35°C) for measurement of larger particles with the aerodynamic particle sizer. Dry size distributions were measured with an electrical mobility technique (40 nm < D < 850 nm), a time-of-flight technique (aerodynamic 0.6 < D < 20 μm), and an optical sizing technique (0.1 < D < 2 μm) [*Hering and McMurry*, 1991; *Sachweh et al.*, 1998; *Hand and Kreidenweis*, 2002].

Examination of the overlapping regions for these measurements yields retrieval of the real part of the aerosol refractive index. Data from the differential mobility analyzer (DMA) and an optical particle counter (OPC) were aligned, giving a size distribution for $0.04 < D_p < 2$ μm (geometric diameter) [*Knutson and Lioy*, 1989]. The DMA sized aerosol particles by their electrical mobility diameter, close to the true geometric D_p, while the OPC sized particles by their optical diameter, a function of the particle refractive index. An iterative alignment method assuming a range of refractive indices was applied to OPC size distributions to match them to DMA size distributions, returning the best fit real refractive index. An OPC sampled dried aerosol from the same inlet; however, failure of the instrument flow rate meter required replacing its data with measurements made by a second OPC not connected to the drying system. The RH in this second instrument was measured at the exhaust, and only data with RH < 25% were used. Aerosol hygroscopic growth factors were observed to be very low through the study [*Carrico et al.*, 2005], so humidity effects on particle size were likely very small. The study average RH for the exhaust flow of the OPC sampling nondried aerosol was RH = 14 ± 4%.

Several optical instruments were operated during the Yosemite study to measure aerosol light scattering, light extinction, dry aerosol light scattering, and light scattering as a function of relative humidity. The ambient light scattering coefficient at 550 nm was measured using two standard Optec nephelometers and two Optec nephelometers fitted with 2.5 μm cutpoint cyclones [*Molenar*, 1997]. The ambient light extinction coefficient at 550 nm was measured continuously using an transmissometer (Optec LPV-2) [*Molenar et al.*, 1989]. "Dry" σ_{sp} was measured with

several instruments including two Radiance Research M903 nephelometers at an effective wavelength of 530 nm [*Day et al.*, 2000; *Day and Malm*, 2001].

Hygroscopic growth in light scattering (*f*(RH)) was measured using a tandem nephelometery system with two nephelometers (Radiance Research M903) that measured σ_{sp} at a wavelength of 530 nm [*Day et al.*, 2000; *Day and Malm*, 2001]. One of these nephelometers was operated at low RH continuously (RH < 20% reference σ_{sp}), while the second nephelometer measured σ_{sp} with variable RH controlled to 10% < RH < 95%. RH was controlled upstream using bundles of 10 Nafion® membrane driers (Perma Pure Inc., MD-110-48SS) [*Day and Malm*, 2001]. Using two of these bundles in series allowed drying followed by humidification (or vice versa) to allow measurements on the deliquescent (or metastable) branch of the particle growth hysteresis loop. The enhancement in σ_{sp} due to RH or *f*(RH) is the ratio of σ_{sp}(RH)/σ_{sp} (low RH).

Measurements of aerosol hygroscopicity were also conducted with a humidified tandem differential mobility analyzer (HTDMA) [*Rader and McMurry*, 1986; *Carrico et al.*, 2005]. The instrument contains two electrostatic classifiers (TSI, Inc., model 3071), two condensation particle counters (TDI, Inc., model 3010), and a membrane-based humidification system (Perma Pure Inc.) [*Brechtel and Kreidenweis*, 2000; *Prenni et al.*, 2003; *Carrico et al.*, 2005]. The instrument selected a nearly monodisperse segment of the dry (RH < 5%) aerosol population and conditioned the sample to a controlled RH to examine the diameter growth factors on the deliquescent branch of the aerosol growth hysteresis loop. Typically, dry diameters of 100 and 200 nm and RH setpoints of 5, 40, 60, 70, 80, 85, and 90% were selected during the Yosemite study.

Individual particle analysis using electron microscopy was performed on YACS samples to characterize particle size, morphology, composition, and mixing states. The Pacific Northwest National Laboratory TRAC (time-resolved aerosol collector) sampler was used to collect 15-minute aerosol samples during 10 August to 4 September 2002 [*Laskin and Cowin*, 2001; *Laskin et al.*, 2003; *Hand et al.*, 2005]. The sampler is a one-stage jet and plate impactor with a $PM_{2.5}$ upper size cut and a lower size limit of $D_p \sim 0.37$ μm. Single particle analyses were performed with computer-controlled scanning electron microscopy (CCSEM), and a combination of backscattered and transmitted electron signals was used to image particles.

Table 6.1 Summary of aerosol chemical composition measurements.

Instrument and Size cut	Species Measured	Substrate	Denuder	Time Resolution	Analytical Technique	Purpose
IMPROVE $PM_{2.5}$ Chan A	Elements, Mass	Teflon®	None	24 hour	X-ray Fluorescence (XRF), Gravimetric	Mass Concentration and Elemental Content of $PM_{2.5}$
IMPROVE $PM_{2.5}$ Chan B	SO_4^{2-}, NO_3^-, Cl^-,	Nylon	Na_2CO_3	24 hour	Ion Chromatography	Anionic Content of $PM_{2.5}$
IMPROVE $PM_{2.5}$ Chan C	Organic and Elemental Carbon	Quartz	None	24 hour	Thermal Optical Reflectance (TOR)	Organic and Elemental Carbon Content of $PM_{2.5}$
IMPROVE PM_{10} Chan A	Elements, Mass	Teflon®	None	24 hour	XRF, Gravimetric	Mass Concentration and Elemental Content of PM_{10}
IMPROVE PM_{10} Chan B	SO_4^{2-}, NO_3^-, Cl^-,	Nylon	Na_2CO_3	24 hour	Ion Chromatography	Anionic Content of PM_{10}
IMPROVE PM_{10} Chan C	Organic and Elemental Carbon	Quartz	None	24 hour	TOR	Organic and Elemental Carbon Content of $PM_{2.5}$
URG $PM_{2.5}$	SO_4^{2-}, NO_3^-, Cl^-, NH_4^+, Na^+, K^+	Teflo Primary Nylon Backup	Na_2CO_3 & H_3PO_3	24 hour (6-hour intensives)	Ion Chromatography	Ionic Content of $PM_{2.5}$
MOUDI Multi-stage Impactor	SO_4^{2-}, NO_3^-, Cl^-, NH_4^+, Na^+, K^+	Aluminum Foil Teflo after-filter	None	24 hour (12-hour intensives)	Ion Chromatography	Ionic Size Distribution
Hi-vols Multistage and $PM_{2.5}$	Multiple Organic Carbon Species	Pre-fired Quartz	None	24 or 48 hour (12-hour intensives)	GC-MS	Marker Compounds for POM Sources
PILS $PM_{2.5}$	SO_4^{2-}, NO_3^-, Cl^-, NH_4^+, Na^+, K^+	None	Na_2CO_3 & H_3PO_3	15 min	Ion Chromatography	High Time Resolution Ionic Content of $PM_{2.5}$
SEM $PM_{2.5}$	Individual Particle Analysis	Copper Mesh Grids with Carbon Films	None	15 min	Scanning Electron Microscope and EDX	Particle Morphology and Atomic Weight %
R&P $PM_{2.5}$	Total Carbon	Stainless Steel Impactor	None	1 hour	Thermal Desorption	High Time Resolution Carbon Content of $PM_{2.5}$
Aethalometer $PM_{2.5}$	Black Carbon	Quartz	None	5 min	Light Absorption at Two Wavelengths	Black Carbon Content of $PM_{2.5}$; Qualitative Biomass Smoke Marker
Hi-vol $PM_{2.5}$	C_{12}/C_{14} Isotope	Pre-fired Quartz	None	12 hour daytime	Accelerator Mass Spec (AMS)	Modern and Fossil Carbon Fractions of POM in $PM_{2.5}$

Table 6.2 Aerosol physical and optical measurements, averaging periods, etc., for all Yosemite measurements.

Instrument	Parameter Measured	Diameter Size Range	Sample RH	Time Resolution/Frequency	Purpose/Analytical Technique
Optical Particle Counter	D_p	$0.1\mu m < D_p < 2\ \mu m$	RH < 20%	15 min	Optical Particle Sizing
Differential Mobility Analyzer	D_p	$0.04\ \mu m < D_p < 0.85\ \mu m$	RH < 20%	15 min	Electrical Mobility Particle Sizing
Aerodynamic Particle Sizer	D_p	$0.6\ \mu m < D_p < 20\ \mu m$ (aerodynamic)	RH < 20%	15 min	Time of Flight Particle Sizing
Radiance Research Nephelometer	b_{sp}	$D_p < 2.5\ \mu m$	RH < 20%	2 min	Light Scattering Coefficient by Particles for "Dry" Conditions
Radiance Research Nephelometer	b_{sp}	$D_p < 2.5\ \mu m$	5% < RH < 95%	Daily	Light Scattering Dependence on Controlled Relative Humidity
Optec Nephelometer	b_{sp}	$D_p < 2.5\ \mu m$	~ Ambient	2 min	Light Scattering by Fine Mode Particles
Optec Nephelometer	b_{sp}	All	~ Ambient	2 min	Light Scattering by Total Particles
Transmissometer	b_{ext}	All	Ambient	1 min	Ambient Light Extinction Coefficient
Tandem Differential Mobility Analyzer	D/D_o	100 nm, 200 nm	5% < RH < 95%	daily	Particle Size Dependence on Controlled Relative Humidity
Time Resolved Aerosol Collector (TRAC)	D_p. Shape, Composition	$D_p < 2.5\ \mu m$	Uncontrolled	15 min	Individual Particle Analysis using Environmental Scanning Electron Mobility Imaging

7. RESULTS AND DISCUSSION

The results from YACS 2002 are discussed below, beginning with meteorological background and fundamental aerosol chemical, optical, and physical properties including mass concentrations, overall aerosol composition, and light extinction properties. The discussion progresses to more detailed aerosol physical, chemical, and optical properties including aerosol size distributions, hygroscopicity, refractive index and density, individual particle analyses, and speciation of POM.

7.1 Meteorology during YACS

The prevailing meteorology featured hot, dry conditions during YACS, contributing to an active fire season in the West in the summer of 2002. Yosemite is located on the western slope of the Sierra Nevada mountain range. Solar heating during the daytime hours caused San Joaquin valley air to expand and this air was transported upslope to Yosemite. Generally, each morning as temperatures increased, upslope westerly flow transported boundary-layer air from the valley below (often hazy). Winds stagnated or changed to easterlies in the evening due to subsiding airmasses (Figure 7.1). Experiment average (n = 1248 hourly averages) temperature and relative humidity (RH) were 21.1 ± 4.6 °C and 33 ± 11%, while daytime averages during upslope conditions (n = 368 hourly averages from 1000 to 1800 local) were 25.0 ± 3.4 °C and 26 ± 9%, respectively (values are reported as mean ± 1 standard deviation). Aside from light precipitation on the first and last days of YACS, conditions were dry.

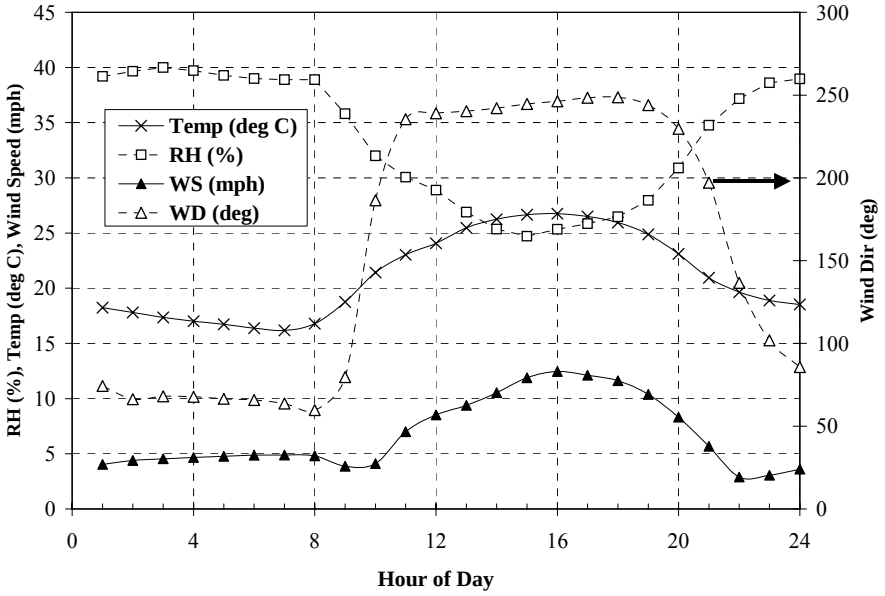

Figure 7.1 Daily average ambient temperature, relative humidity, wind speed, and wind direction at Turtleback Dome averaged over the YACS study period. Winds increased speed and changed from downslope (from the northeast) to upslope (from the southwest) in mid-morning due to diurnal heating.

7.2 Fundamental Aerosol Properties at Yosemite during YACS

7.2.1 $PM_{2.5}$ and Coarse Mass Concentrations at Turtleback Dome during YACS

In general, the Central Valley region of California experienced poor air quality during the summer of 2002 (Figure 7.2). Yosemite National Park also experienced degraded air quality with overall average $PM_{2.5}$ and coarse (diameters from 2.5 to 10 μm) mass concentrations during YACS of 9.6 ± 4.5 and 8.3 ± 2.2 μgm^{-3}, respectively. A predominance of the fine mode contribution to aerosol loading at Yosemite was apparent only during the highest mass loading periods (Figure 7.3). Though they have a myriad of sources, fine mode aerosols are often the result of gas-to-particle conversion and are often the result of combustion processes, both anthropogenic and natural. This is in contrast to coarse mode aerosols, which are often the result of mechanical processes such as the effects of wind on ocean and land surfaces [*Blanchard and Woodcock*, 1980; *Hinds*, 1999]. Historically, the average $PM_{2.5}$ mass concentration in Yosemite during the summer is ~ 8 μgm^{-3} with >50% contribution from POM as indicated from IMPROVE network historical measurements (Table 5.1). Summer 2002 thus was above average in terms of air quality impacts, though not atypical.

Figure 7.2 Local newspaper headlines during the YACS study period.

The fine mass concentration varied widely during the study with 24-hour average values ranging from 4 to 24 μgm^{-3} (Table 7.5, Figure 7.3). In comparison, a polluted urban area (Atlanta, Georgia) featured 24-hour average $PM_{2.5}$ mass concentrations ranging from 11 to 44 μgm^{-3} during the summer [*Carrico et al.*, 2003a]. As another comparison, the EPA's proposed $PM_{2.5}$ annual standard of 15 μgm^{-3} shows that Yosemite, which is considered to be a "pristine" environment, can at times be considerably impacted by regional haze.

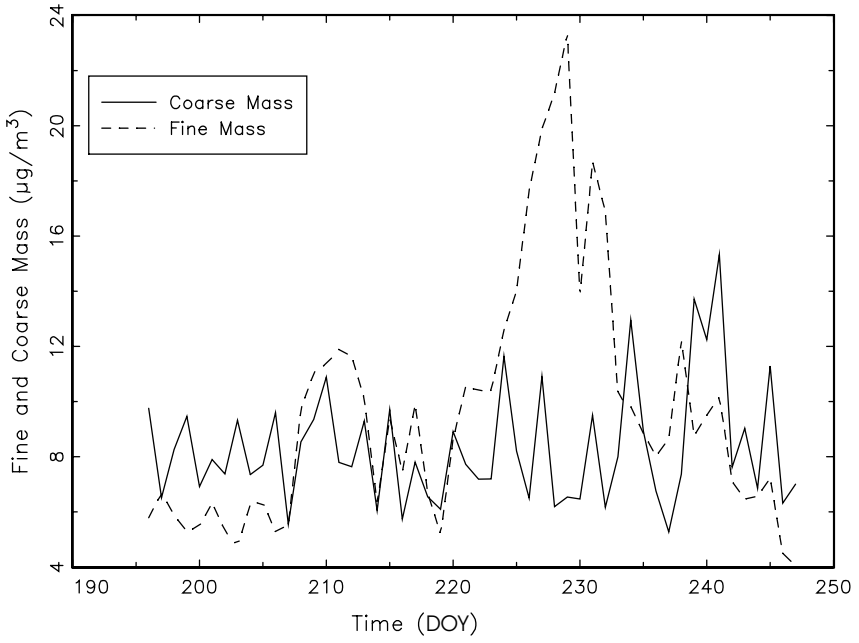

Figure 7.3 Time series of $PM_{2.5}$ and coarse mass concentrations at Turtleback Dome during YACS.

Comparisons of complementary and redundant measurements of $PM_{2.5}$ concentration provide quality control for the various sampling methodologies used during YACS. Comparisons of individual species are detailed later; here, a comparison between overall $PM_{2.5}$ mass concentrations is explored. The scatter plot of measured versus reconstructed $PM_{2.5}$, Figure 7.4, shows high correlation between the gravimetric $PM_{2.5}$ measurements and the mass of individual species reconstructed using standard IMPROVE protocols (i.e., equation 7.1). Two scenarios for the reconstruction equation are considered: (a) using a 1.4 multiplier for estimating POM/OC, which is the typically assumed IMPROVE value, and (b) using a 1.8 multiplier for POM/OC. Also, based on MOUDI and PILS measurements that are discussed in further detail below, nitrate is considered to be in the form of $NaNO_3$.

$$FM = [(NH_4)_2 SO_4] + [NaNO_3] + [1.4 * OC] + [EC] + [SOIL] \qquad (7.1)$$

The 1.8 POM/OC multiplication factor was derived from an OLS regression with $PM_{2.5}$ mass concentration as the dependent variable and the various species as independent variables. The R^2 for the scatter plot shown in Figure 7.4 with the 1.8 multiplier is 0.98, while the slope is 1.05 ± 0.02 and the intercept is not significantly different from zero, implying, to within the uncertainty of the measurements, no bias between reconstructed and gravimetric $PM_{2.5}$ mass concentrations. Using the 1.4 multiplier, as is the recommended value in the Regional Haze Guidance document [*United States Environmental Protection Agency*, 2003a] for calculating the POM/OC ratio, underestimates gravimetric $PM_{2.5}$ mass with a 20% multiplicative bias. At higher $PM_{2.5}$ concentrations, this bias is greater than the inherent uncertainty of the species concentrations measurements (Figure 7.4).

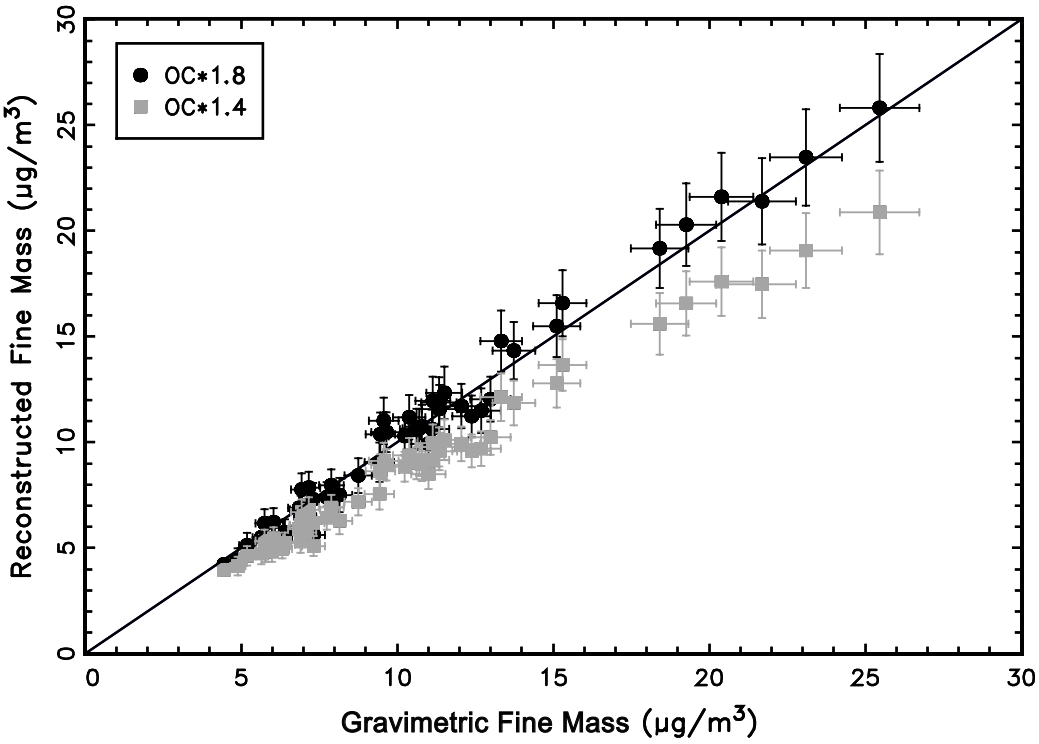

Figure 7.4 Scatter plot of gravimetric mass and the sum of derived aerosol species mass concentrations with POM = 1.4*OC (gray squares) and POM = 1.8*OC (black circles).

A second means of estimating mass concentration is by integrating over volume size distributions that are derived from measured number size distributions [*McMeeking et al.*, 2005a]. Assuming a POM density of 1.5 g cm^{-3}, using literature densities for other constituents, and using a POM/OC multiplier of 1.8 give similarly strong agreement between measured and calculated mass (Figure 7.5). Both of the comparisons shown in Figure 7.4 and Figure 7.5 give confidence to the measurements of $PM_{2.5}$ mass concentrations and show that the "standard" assumption of POM/OC multiplier of 1.4 is an underestimate for YACS aerosol.

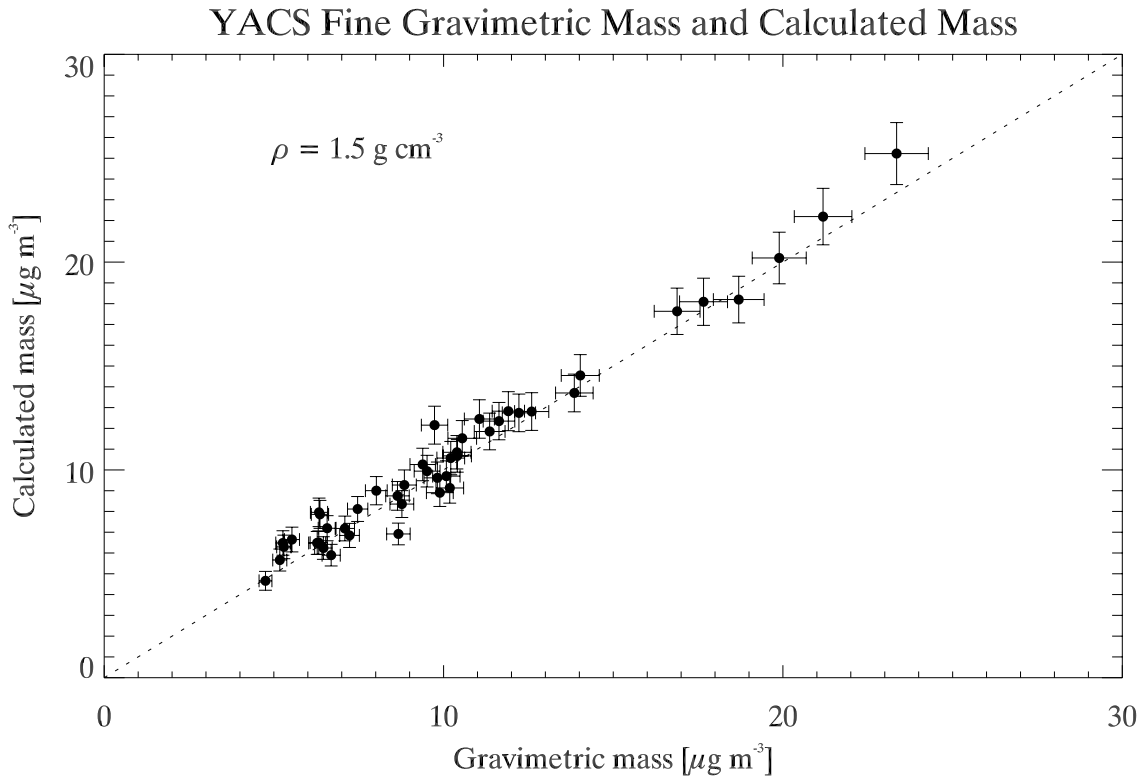

Figure 7.5 YACS gravimetric mass and calculated mass concentrations from integrated volume concentrations and density calculated from composition measurements (POM/OC ratio of 1.8).

As POM was so important, one further mass closure comparison using the high time resolution carbon measurement (R&P 5400) averaged to 24 hours gives further insight (Figure 7.6). Using the R&P to reconstruct $PM_{2.5}$ mass concentrations (POM/OC of 1.8) shows much poorer agreement with measured gravimetric mass than did the integrated volumes or 24-hour, filter-based mass reconstructions above. The comparison suggests the R&P measurement was biased high during periods of low concentration and vice versa as explored further below [*Malm et al.*, 2005a].

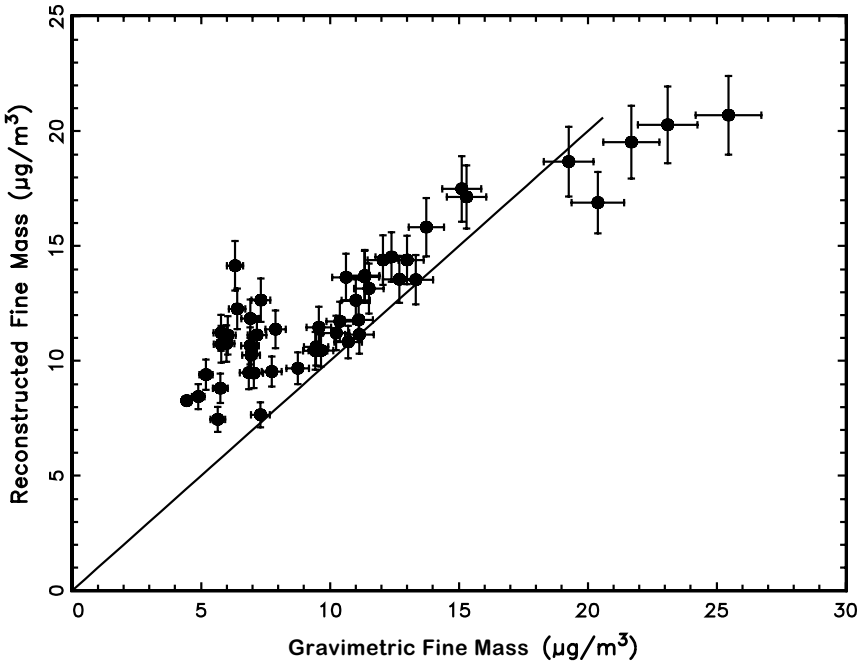

Figure 7.6 Scatter plot of gravimetric fine mass and sum of derived aerosol species mass or reconstructed fine mass concentrations using R&P-measured carbon times 1.8 and with an assumed uncertainty of 5%. Using R&P carbon shows a bias at low and high carbon concentrations.

7.2.2 Harmony Comparisons between Complementary Techniques: Inorganic Composition

Comparisons between species concentrations measured with various time-integrated and semi-continuous methods give a means of quality control and data validation. "Harmony" comparisons of the most important inorganic species including SO_4^{2-}, NH_4^+, NO_3^-, and K^+ among complementary techniques are discussed here. Additive and multiplicative biases are explored through correlation tables and OLS regression analysis [*Malm et al.*, 2005a]. The IMPROVE and URG samplers gave 24-hour average concentrations, while the PILS measured semi-continuous 15-minute concentrations (http://vista.cira.colostate.edu/improve/Publications/SOPs/arssop.asp). The PILS measurements are averaged over 24 hours to compare with the time-integrated samplers. Discrete mass size distributions from the MOUDI were smoothed using the Twomey inversion method and summed on relevant stages to compare with the $PM_{2.5}$ size cut of the other samplers on 25 sampling days in common from all measurements. Uncertainties for the 24-hour average filter measurements are better established and are deemed "standards" against which other measurements are compared.

Overall, 24-hour "bulk" filter measurements compared reasonably well with one another. Average SO_4^{2-} was 1.16 µg/m^3 for IMPROVE and URG and is used as the "reference value." The

difference between sulfate mass as determined by these two systems is about 8%, while the intervariable correlation is high at 0.98 [*Lee et al.*, 2004]. The bias between the two samplers is multiplicative as opposed to an additive offset. Also, if all sulfur from x-ray fluorescence analysis of IMPROVE filters is assumed in the form of SO_4^{2-}, elemental sulfur times three (3*S) can be compared to the other samplers. IMPROVE 3*S is 17% lower than the reference value but highly correlated with the URG SO_4^{2-} at 0.97. MOUDI SO_4^{2-} (including the after-filter) is 6% lower than the reference value but nearly the same as URG-derived SO_4^{2-}. Note that Table 7.2 shows ~ 28% of SO_4^{2-} on average is found on the after-filter, implying an ultra fine SO_4^{2-} mode with $D_p < 0.18$ μm, the cutpoint of the last MOUDI stage. This mode was more commonly observed in the early part of the experiment. It should be noted that the MOUDI does not include a specific size cut at $D_p = 2.5$ μm, so the size distributions are smoothed using the Twomey method, which may contribute to differences.

Based on the semi-continuous PILS measurement, large diurnal variability in SO_4^{2-} was observed (Figure 7.7a) and strongly influenced by the mountain-valley wind system (Figure 7.1). On average, PILS-derived SO_4^{2-} (averaged to 24 hours) compares favorably as it is 6% lower than the reference value. However, the correlation between PILS and the other methods is lowest at ~ 0.7 (Table 7.1, Figure 7.7b). Estimated URG SO_4^{2-} uncertainties are shown in Table 7.4; however, they have not been established for the PILS measurements. Except for three outlying data points, there is an additive offset PILS SO_4^{2-} ~ 0.4 μg/m^3 lower over all sampling periods.

Among nitrate measurements, IMPROVE and URG NO_3^- values compare most favorably with an average of 0.36 μg/m^3 and a difference of 18% (Table 7.1, Table 7.2). Regression shows a strong correlation (0.98) with ~ 0.04 μg/m^3 additive offset and a 6% multiplicative bias. For $PM_{2.5}$, MOUDI NO_3^- is about 50% lower than this average, though a smaller 14% was observed in the coarse mode. Coarse mode NO_3^- is primarily in the form of $NaNO_3$, while in the fine mode it is the more volatile NH_4NO_3 (discussed further below). The larger fine mode discrepancy between the MOUDI and the reference may result from NH_4NO_3 volatilization from the MOUDI impaction surfaces. PILS NO_3^- is ~ 22% lower than the reference though well correlated (0.83). The scatter plot (Figure 7.8) shows PILS NO_3^- is biased low with respect to the URG, with additive and multiplicative low biases of 0.11 μg/m^3 and 2%, respectively.

The IMPROVE potassium measurement uses XRF analysis and is therefore an elemental concentration, while the other samplers' filters are analyzed by ion chromatography for K^+. On

average, the concentration of potassium was ~ 0.06 μg/m^3 and compared well between samplers with $R^2 > 0.9$ for URG, IMPROVE, and PILS. However, the MOUDI R^2 was between 0.5 and 0.6. IMPROVE, URG, and MOUDI agree well in magnitude, while the PILS-derived potassium is lower with a 0.01 additive bias. Ammonium ion (NH_4^+) was measured by the URG and MOUDI samplers; analysis shows NH_4^+ compares closely with an average difference ~ 8% and R^2 of 0.93. Similar to SO_4^{2-}, ~ 32% of NH_4^+ is on the MOUDI after-filter and associated with an ultra fine mode aerosol. It is also interesting to note that, relative to the fine mode, a substantial amount of ammonium is also found in the coarse fraction. More detailed intercomparisons including additional species are given in *Malm et al.*, [2005a].

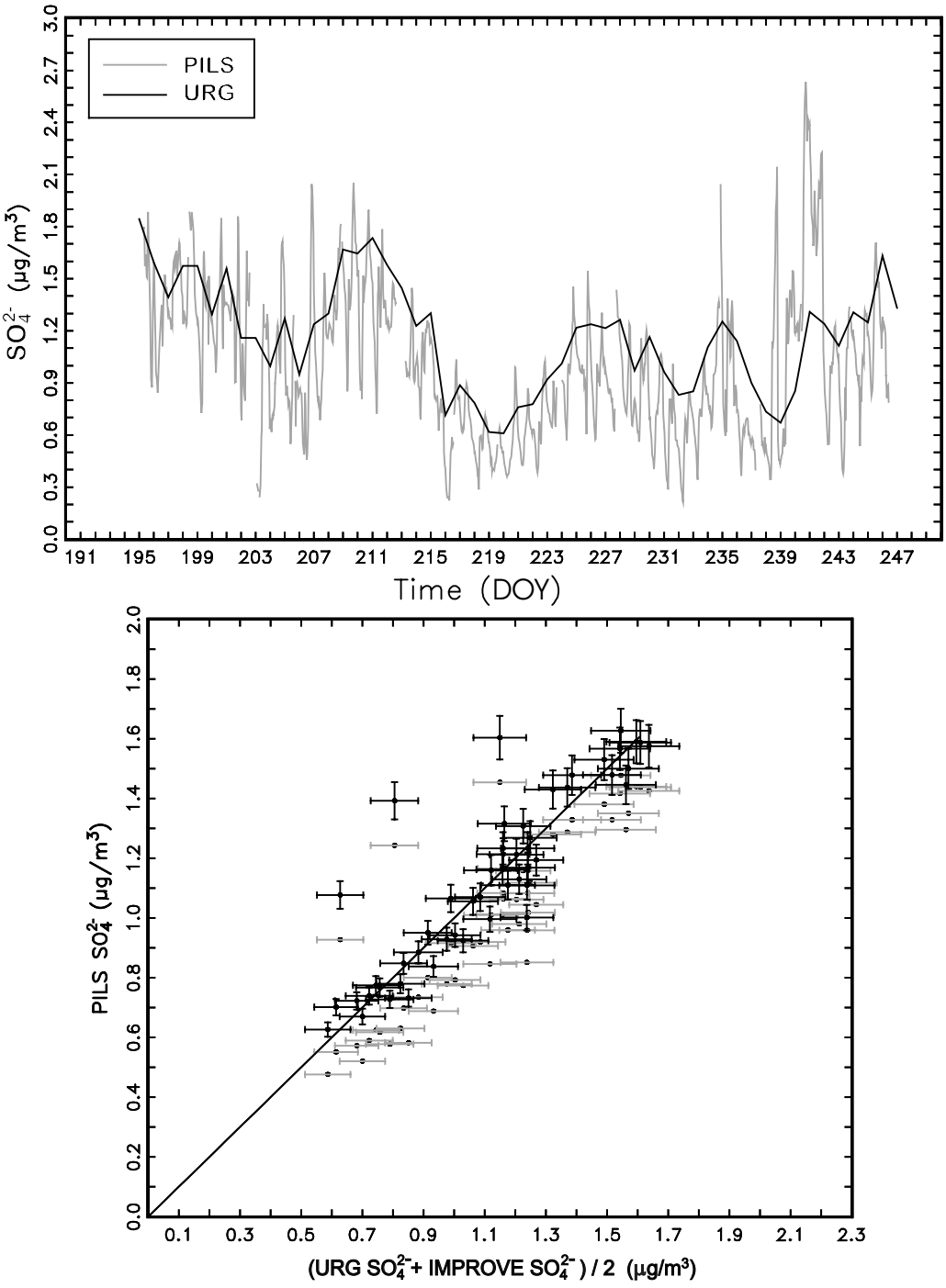

Figure 7.7 Time series and scatter plots of the 24-hour average filter-based (URG/IMPROVE) versus PILS fine sulfate mass concentrations. PILS data has been averaged to 24 hours for comparison to URG/IMPROVE samples. Data points in gray are for the measured data sets, while those in black correspond to the bias-corrected PILS data.

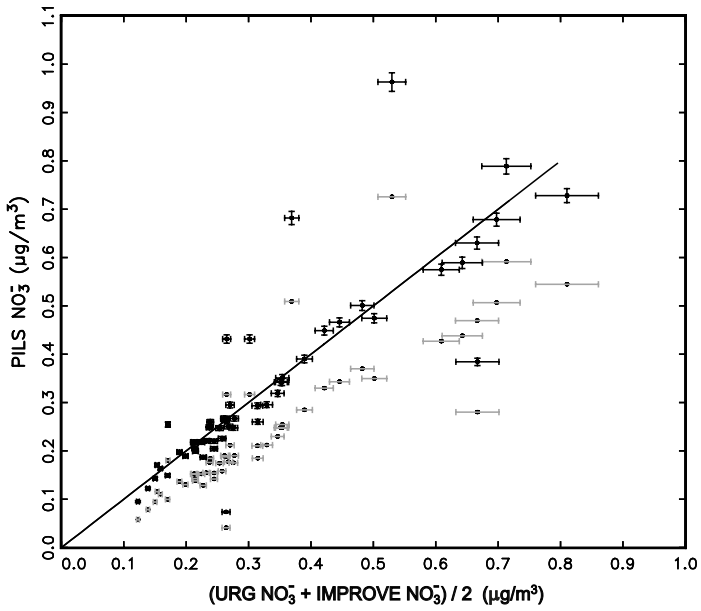

Figure 7.8 Scatter plot of the average URG/IMPROVE and PILS fine nitrate mass concentrations. PILS data has been averaged to 24 hours for comparison to URG/IMPROVE samples. Data points in gray are for the measured data sets, while those in black correspond to the bias-corrected PILS data.

Table 7.1 Correlation table (R^2) of species concentrations derived from the measurement methodologies used during YACS. All concentrations correspond to $D_p < 2.5$ µm unless otherwise noted. NH_4^+ from the URG and MOUDI samplers were correlated at 0.93.

	IMPROVE	**URG**	**MOUDI**	**PILS**	**IMPROVE XRD Sulfur*3**
IMPROVE SO_4^{2-}	1.00	0.98	0.96	0.70	0.96
IMPROVE XRF Sulfur*3	0.96	0.97	0.98	0.68	1.00
URG SO_4^{2-}	0.98	1.00	0.96	0.74	0.97
MOUDI SO_4^{2-}	0.96	0.96	1.00	0.67	0.98
PILS SO_4^{2-}	0.70	0.74	0.67	1.00	0.68
IMPROVE NO_3^-	1.00	0.98	0.78	0.84	
URG NO_3^-	0.98	1.00	0.81	0.83	
MOUDI NO_3^-	0.78	0.81	1.00	0.63	
PILS NO_3^-	0.84	0.83	0.63	1.00	
IMPROVE K^+	1.00	0.97	0.55	0.91	
URG K^+	0.97	1.00	0.52	0.90	
MOUDI K^+ (0.18–2.5 µm)	0.55	0.52	1.00	0.57	
PILS K^+	0.91	0.90	0.57	1.00	

Charge neutrality (total cation charge = total anion charge) as determined from ion chromatography measurements provides a further quality control comparison. Substrates collected with the URG sampling system were analyzed for the anions SO_4^{2-}, NO_3^-, Cl^-, and oxalate, and the cations NH_4^+, Na^+, Ca^{2+}, Mg^{2+}, and K^+. Ignoring oxalate gives excess cations a net positive charge, while inclusion of oxalate gives a much closer charge balance (Figure 7.9). For an aerosol that includes such organic acid species that are typically not included in the IMPROVE protocol, charge balance may not be achieved. Other inorganic species that are not commonly quantified, for example, carbonate, might also contribute to such charge imbalances.

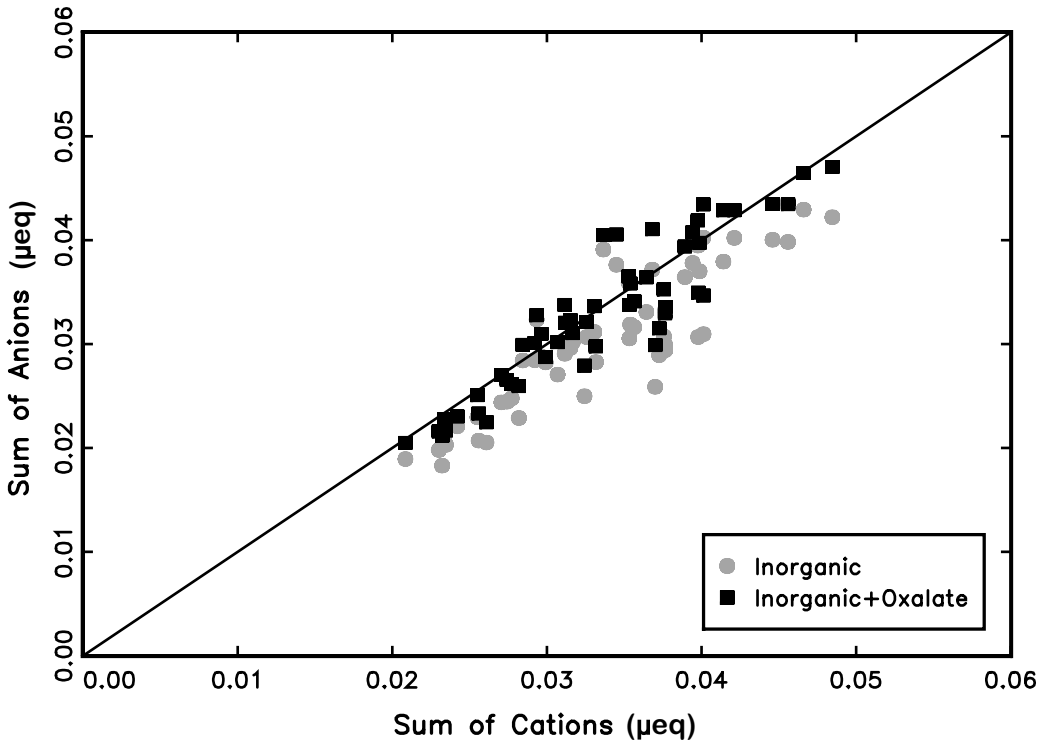

Figure 7.9 Charge balance between cations and anions with and without oxalate included.

Table 7.2 Summary of inorganic species concentrations derived from the measurement methodologies used during YACS. The minimum detection limit (MDL) for these systems is on the order of 0.01–0.02 μg/m^3. All measurements are 24-hour averages.

Species Concentration (μg/m^3)	Size Range	Mean	UNC	Std Dev	Min	Max
IMPROVE SO_4^{2-}	$PM_{2.5}$	1.11	0.011	0.31	0.56	1.55
XRF Sulfur*3	$PM_{2.5}$	0.92	0.003	0.27	0.45	1.37
URG SO_4^{2-}	$PM_{2.5}$	1.20	0.005	0.33	0.61	1.73
MOUDI SO_4^{2-}	0.18–2.5 μm	1.09	0.014	0.32	0.57	1.64
After-filter SO_4^{2-}	<0.18 μm	0.30	0.005	0.27	0.05	0.83
PILS SO_4^{2-}	$PM_{2.5}$	1.09	NA	0.35	0.48	2.01
IMPROVE Coarse SO_4^{2-}	2.5-10 μm	0.00	0.011	0.04	-0.07	0.09
MOUDI Coarse SO_4^{2-}	2.5-10 μm	0.79	0.018	0.17	0.49	1.08
IMPROVE NO_3^-	$PM_{2.5}$	0.32	0.004	0.17	0.14	0.75
URG NO_3^-	$PM_{2.5}$	0.39	0.006	0.17	0.16	0.88
MOUDI NO_3^-	0.18–2.5 μm	0.18	0.006	0.09	0.07	0.43
After-filter NO_3^-	<0.18 μm	0.01	0.003	0.01	0.00	0.02
PILS NO_3^-	$PM_{2.5}$	0.28	NA	0.16	0.03	0.09
IMPROVE Coarse NO_3^-	2.5-10 μm	0.21	0.008	0.12	-0.08	0.46
MOUDI Coarse NO_3^-	2.5-10 μm	0.18	0.006	0.09	0.06	0.43
IMPROVE K^+	$PM_{2.5}$	0.06	0.001	0.02	0.03	0.11
URG K^+	$PM_{2.5}$	0.06	0.001	0.03	0.02	0.13
MOUDI K^+	0.18–2.5 μm	0.06	0.016	0.03	0.02	0.14
After-filter K^+	<0.18 μm	0.01	0.006	0.01	0.00	0.03
PILS K^+	$PM_{2.5}$	0.05	NA	0.02	0.01	0.10
MOUDI Coarse K^+	2.5-10 μm	0.05	0.012	0.04	0.01	0.14
URG NH_4^+	$PM_{2.5}$	0.48	0.002	0.11	0.26	0.65
MOUDI NH_4^+	0.18–2.5 μm	0.52	0.010	0.13	0.28	0.78
After-filter NH_4^+	<0.18 μm	0.17	0.004	0.13	0.04	0.42
MOUDI Coarse NH_4^+	2.5-10 μm	0.36	0.010	0.09	0.20	0.53

7.2.3 Harmony Comparisons between Complementary Techniques: Carbonaceous Content

$PM_{2.5}$ was collected over 24-hour periods using an IMPROVE sampler with quartz fiber filters; these filters were analyzed using the thermal-optical-reflectance method (TOR) to obtain organic carbon (OC) and elemental carbon (EC) concentrations, which combined give total carbon (TC)

[*Malm et al.*, 2005a]. Semi-continuous TC was also measured using the R&P 5400 instrument, while an aethalometer (Magee Scientific AE2) was used to measure black carbon (BC). Summary statistics and correlations between carbon measurements are given in Table 7.3, while temporal and scatter plots of total carbon concentrations are given in Figure 7.10.

On average, R&P-derived TC was ~ 40% higher than IMPROVE/TOR TC, but more importantly, there was not a clear additive or multiplicative bias observed. During the beginning and end of the study period, R&P carbon is biased substantially higher (~ factor of 5) than IMPROVE TOR carbon, while during the elevated carbon episode (DOY = 225–230), it is biased low. In general, when aerosol mass was low, R&P carbon was greater than IMPROVE/TOR carbon, while the opposite was true at higher mass concentrations. This difference not only showed up over the longer time frame of weeks but also on a diurnal basis. Expressed as the average of the absolute value of the mean difference, the estimated average uncertainty of the R&P TC concentrations is about 0.9 $\mu g/m^3$ for an average OC mass concentration of 2.1 $\mu g/m^3$ or ~ 43% uncertainty. Although the uncertainty in the semi-continuous carbon analyzer appears large, the correlation between the OC measurements is relatively good with $R^2 = 0.87–0.93$.

IMPROVE TOR elemental carbon and black carbon derived from the aethalometer differ by about 25%, with IMPROVE TOR elemental carbon being the highest (Table 7.4). For the IMPROVE system EC/TC = 0.09, while for the R&P-aethalometer combination EC/TC = 0.05. Finally, about four times as much organic carbon is found in the fine versus coarse mode, while for elemental carbon the ratio is near 10. This substantial difference between these carbon-monitoring systems will be further explored with light scattering closure calculations in later sections.

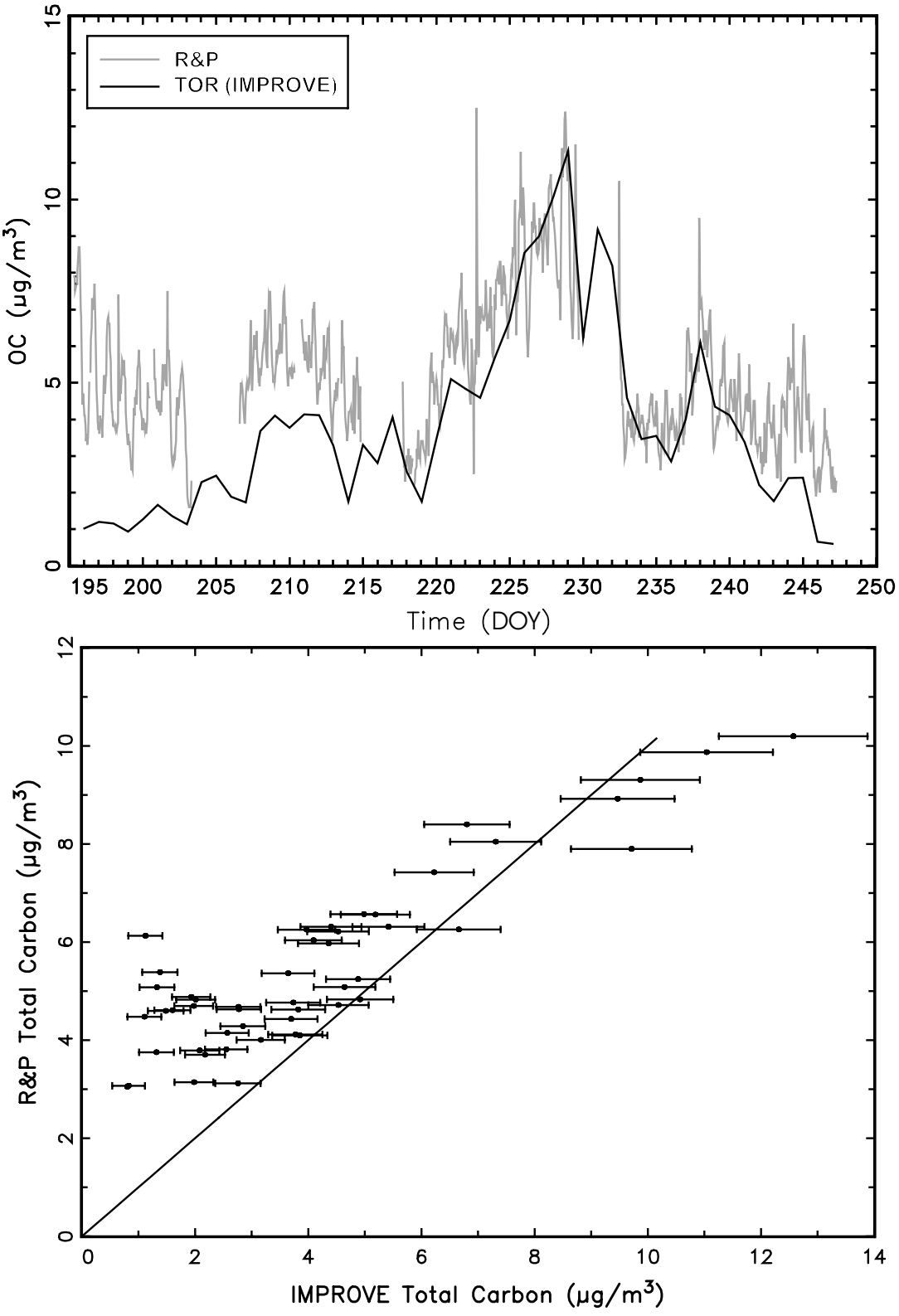

Figure 7.10 Temporal and scatter plots of semi-continuous carbon data from the R&P 5400 instrument and IMPROVE (TOR) 24-hour average total carbon (TC) mass concentration.

Table 7.3 Correlation table of total carbon (TC) and elemental carbon (EC or black carbon) mass concentrations derived from various sampling and analytic methodologies.

Carbon Measurements	R&P TC	IMPROVE TOR EC	Aethalometer BC
IMPROVE TOR TC	0.89	0.91	0.94
R&P TC	NA	0.80	0.91
IMPROVE TOR EC	NA	NA	0.87

Table 7.4 Statistical summary of carbon mass concentration derived from various sampling and analytic methodologies (n = 49 samples). Comparisons are made for time periods with data in common for all the indicated samplers.

Variable ($\mu g/m^3$)	**Mean**	**UNC**	**Std Dev**	**Minimum**	**Maximum**
IMPROVE TOR TC	4.09	0.081	2.75	0.80	12.57
R&P TC	5.46	NA	1.78	3.05	10.20
IMPROVE TOR EC	0.39	0.014	0.22	0.10	1.23
Aethalometer BC	0.29	0.013	0.13	0.13	0.68
IMPROVE Coarse TOR TC	0.99	0.080	0.32	0.46	1.81
IMPROVE Coarse TOR EC	0.04	0.014	0.11	-0.37	0.28

7.2.4 24-Hour Average Aerosol Composition at Turtleback Dome during YACS

Having established the comparability of sampling methods above, individual constituents of the $PM_{2.5}$ aerosol during YACS are next explored in more detail. The coarse (particles with diameters between 2.5 and 10 μm) mass concentration at Turtleback Dome (7.5 ± 2.2 μgm^{-3}) was dominated by soil dust contributions (72%), POM (23%), and nitrate (4%), the latter observed in the form of sodium nitrate as discussed later (Table 7.6). $PM_{2.5}$ composition during YACS was dominated by POM, on average ~ 70% of $PM_{2.5}$ mass concentration [*Malm et al.*, 2005a]. During YACS, POM, EC, ammonium sulfate, sodium nitrate, and soil dust composed 70, 5, 15, 5, and 6%, respectively, of $PM_{2.5}$ mass concentration that averaged 9.6 μgm^{-3} (Table 7.5). $PM_{2.5}$ POM at Turtleback Dome was 6.8 μgm^{-3} on average, using a multiplier of 1.8 for the conversion of OC to POM. This is higher than historical average POM fractions at most parks, even in the western United States. Historically, as indicated from IMPROVE measurements, average POM (1988–2003 using a 1.8 POM/OC multiplier) is 6.4 $\mu g/m^3$ and dominates $PM_{2.5}$ at Yosemite during the summer (Table 5.1). The historical value of POM is 5.4 $\mu g/m^3$ if measurements from 2001, when huge spikes in POM were observed, presumably related to local fires, are excluded. Still, POM dominates $PM_{2.5}$ at Yosemite, historically accounting for 64% of $PM_{2.5}$. This demonstrates summertime air quality at Yosemite, and particularly in the summer 2002, to be strongly POM-impacted at Yosemite. The carbonaceous component of the aerosol was dominated by POM with LAC concentrations

always < 1 μg/m^3 and only several percent of $PM_{2.5}$ on average (Figure 7.11). This shows a limited soot component and suggests limited anthropogenic influence, as urban areas often have EC concentrations making up a substantial fraction of POM [*Moosmuller et al.*, 2001; *Carrico et al.*, 2003a]. Using the same 1.8 OC/POM multiplier found here, the EPA assumed natural background POM concentrations of ~ 0.6 μgm^{-3} in the West when developing the Regional Haze Rule, and a modeling study suggests a best estimate of ~ 1.6 μgm^{-3} (both here taking their OC concentrations and multiplying by 1.8) [*Park et al.*, 2003; *United States Environmental Protection Agency*, 2003b]. POM concentration during YACS, on average 7 μgm^{-3} and reaching a 24-hour maximum of 20 μg/m^3 (85% of $PM_{2.5}$), is much higher than either estimate of "background" conditions.

A time series comparison of 24-hour average composition measurements from IMPROVE filters also illustrates the dominance of POM, showing it to control the overall variability in $PM_{2.5}$ (Figure 7.11). Even the coarse mode of the aerosol (2.5 μm < D_p < 10 μm) showed a substantial POM contribution, though estimated soil dominated this size fraction (Table 7.6). The time series of POM versus the time series of ionic components shows distinctly different temporal profiles, suggesting different sources and/or controlling processes for carbon and inorganic aerosol components during YACS (Figure 7.11). During the haziest 14-day period in mid-August (DOY 221–235), $PM_{2.5}$ mass concentrations varied from 15 to 20 μgm^{-3} and the contribution of POM exceeded 80% (Figure 7.11). This period was strongly impacted by biomass smoke as discussed in greater detail later. A summary of the composition is provided in Table 7.5.

Table 7.5 Average $PM_{2.5}$ properties during YACS (20 July through 5 September 2002) based on n = 52 samples.

Variable (μg/m$^{3)}$	Mean	UNC	Std Dev	Minimum	Maximum
$PM_{2.5}$	9.61	0.080	4.47	4.06	23.35
Recon $PM_{2.5}$ (1.4 POM/OC)	8.35	0.056	3.73	3.85	19.32
Recon $PM_{2.5}$ (1.8 POM/OC)	9.85	0.071	4.74	4.09	23.86
Ammonium Sulfate	1.59	0.011	0.41	0.84	2.38
Sodium Nitrate	0.48	0.004	0.23	0.16	1.20
POM	6.81	0.070	4.59	1.08	20.41
LAC	0.38	0.007	0.22	0.10	1.23
SOIL	0.59	0.006	0.16	0.29	0.94

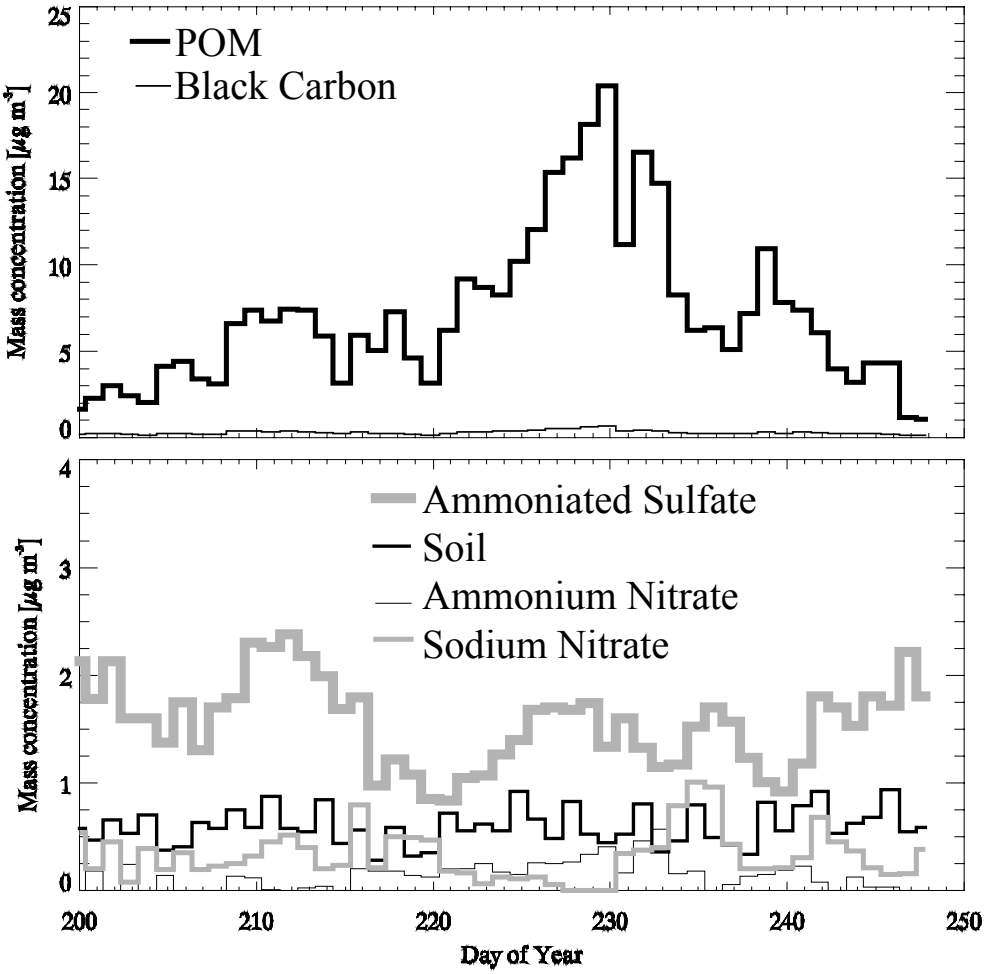

Figure 7.11 Time series of $PM_{2.5}$ carbonaceous species (above) and inorganic components (below) at Turtleback Dome Yosemite during YACS.

Table 7.6 Statistical summary for the coarse mass fraction ($2.5 < D_p < 10.0$ µm) during YACS based on n = 52 samples.

Variable (µg/m^3)	Mean	UNC	Std Dev	Minimum	Maximum
Coarse Mass	7.46	0.103	2.19	4.28	14.41
Ammonium Sulfate	0.00	0.008	0.06	-0.20	0.17
Sodium Nitrate	0.32	0.004	0.24	-0.11	1.48
POM	1.73	0.070	0.57	0.83	3.26
LAC	0.04	0.007	0.11	-0.37	0.28
SOIL (estimated)	5.38	NA	2.05	1.29	11.63

7.2.5 Comparison of Measurements at Turtleback Dome and Yosemite Valley Sampling Sites

Measurements of aerosol chemical composition using IMPROVE samplers and methodology were conducted at two sites in Yosemite National Park during the YACS study: Turtleback Dome and

Yosemite Valley. The Turtleback Dome sampling site, an exposed granite outcropping on the rim, is about 1300 feet above Yosemite Valley. The Yosemite Valley site was located at the visitor center on the floor of the valley itself. The valley site receives heavy motor vehicle traffic and is therefore more susceptible to the influence of vehicle exhaust and other anthropogenic sources.

Overall, the $PM_{2.5}$ chemical compositions in Yosemite Valley and at Turtleback Dome were similar. Yosemite Valley, like Turtleback Dome, had a dominant contribution from POM (>70% of $PM_{2.5}$) and smaller contributions from ammonium sulfate, light-absorbing carbon, and sodium nitrate (Figure 7.12). The residual mass consisted of small contributions from soil dust, aerosol phase water, and trace concentrations of additional species. Both sites show similar temporal trends in $PM_{2.5}$ with ($R^2 = 0.6$), ammonium sulfate ($R^2 = 0.92$), and sodium nitrate ($R^2 = 0.63$). Both sites clearly show the impact of the smoke episodes occurring near DOY 210 and particularly around DOY 230 (Figure 7.13, Figure 7.14).

A key difference between the two sites is higher concentrations of EC and POM at Yosemite Valley, which lead to 20–100% higher total $PM_{2.5}$ mass concentrations. The average $PM_{2.5}$ mass concentration at Yosemite Valley was 16 ± 5 μgm^{-3}, approximately 60% higher than at Turtleback Dome. The average EC concentration observed at Yosemite Valley (0.9 ± 0.4 μgm^{-3}) was considerably larger than at Turtleback Dome (0.4 ± 0.2 μgm^{-3}). The EC concentrations at the two sites were largely decoupled ($R^2 = 0.04$), reflecting the probable influence of local valley sources for this species.

More substantial anthropogenic sources in the valley and perhaps larger smoke contributions due to the closer proximity of local Yosemite prescribed fires draining into the valley may have both contributed to higher concentrations of carbonaceous species. Overall, qualitatively, inorganic species and, to a certain degree, POM concentrations at both sites reflect regional trends. On top of this is an added contribution of POM and EC at Yosemite Valley due to local sources. As will be discussed in more detail later, POM speciation results demonstrate that a greater anthropogenic signature was indeed present at the Yosemite Valley site [*Engling et al.*, 2005].

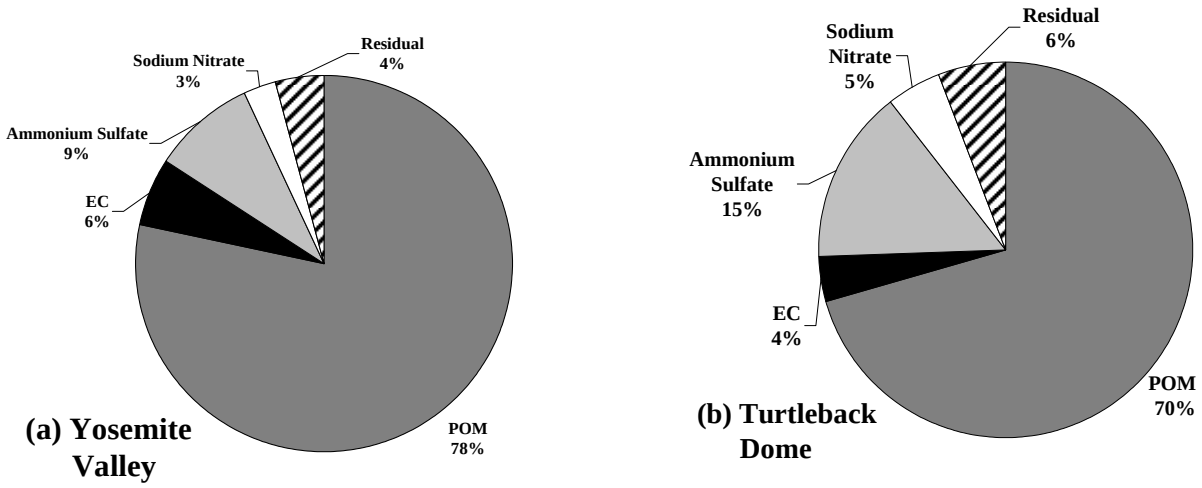

Figure 7.12 Pie chart comparison of $PM_{2.5}$ major chemical composition at Yosemite Valley and Turtleback Dome (assumes POM/OC = 1.8, and sulfate and nitrate in indicated forms). Residual mass is found from the difference in $PM_{2.5}$ mass and the sum of species and is primarily soil dust and aerosol phase water (other constituents compose <1% of $PM_{2.5}$).

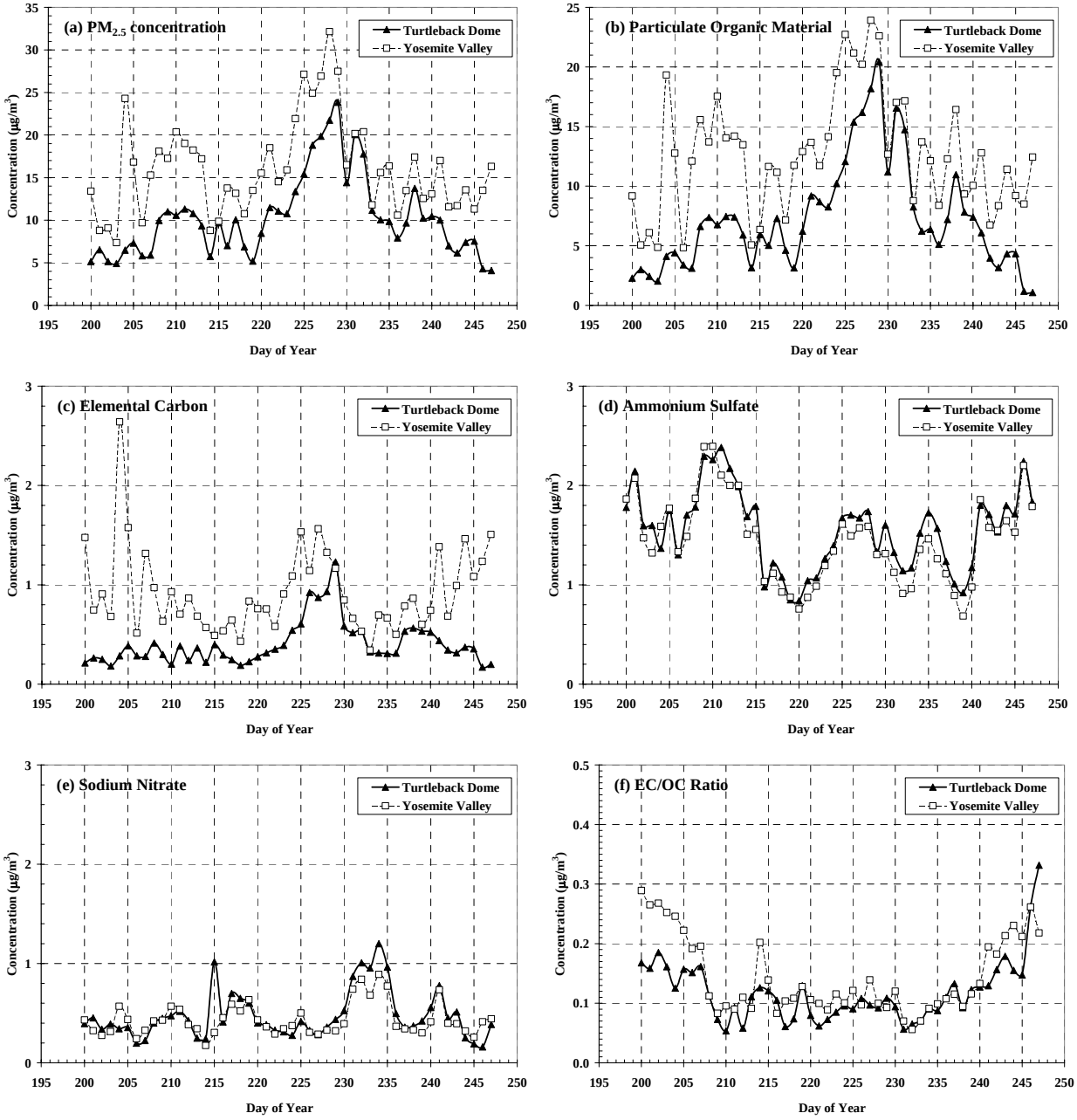

Figure 7.13 Time series comparisons of total $PM_{2.5}$ mass concentration, POM, EC, sulfate, nitrate, and EC/OC ratio at Turtleback Dome and Yosemite Valley sites in Yosemite National Park.

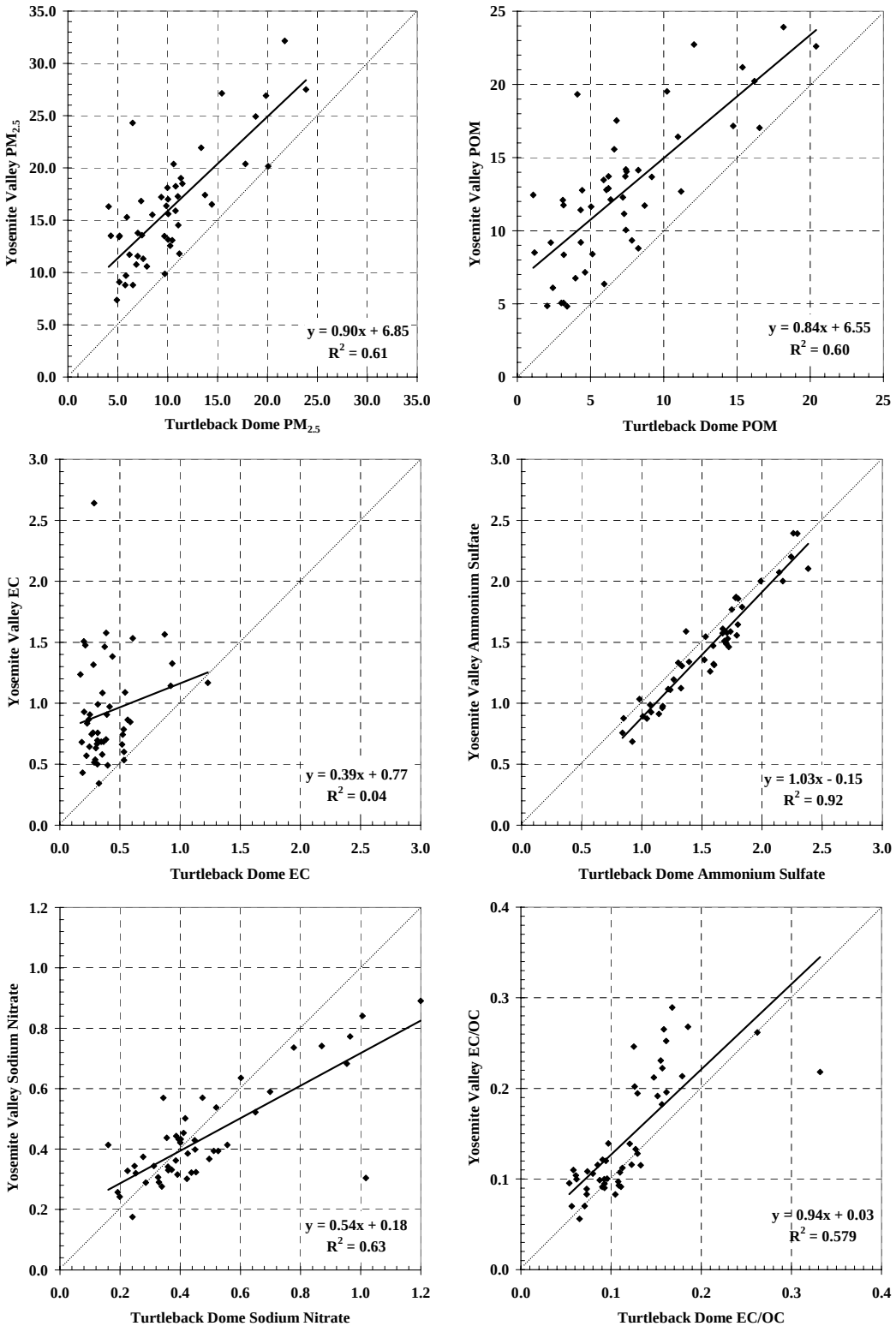

Figure 7.14 Scatter plot comparison of $PM_{2.5}$ mass concentrations and individual species at Yosemite Valley site and Turtleback Dome at Yosemite National Park.

7.2.6 High Time Resolution Features of the Chemical Composition

One objective of YACS was to evaluate the comparability of a wide variety of aerosol monitoring systems including semi-continuous monitors measuring inorganic ions and total carbon as was discussed above in the harmony sections. Twenty-four-hour average measurements demonstrate the dominance of POM, but do not reveal the daily variations of aerosol composition. Several concurrent measurements, including the particle-into-liquid sampler coupled with ion chromatography (PILS/IC), reveal finer time-scale variations in aerosol chemical composition.

The PILS/IC semi-continuous measurement demonstrates the species' intercorrelation and can suggest what molecular form they take. In many polluted environments, nitrate, which typically results from the NOx precursors, is often associated with ammonium and found in submicrometer diameter particles [*Seinfeld and Pandis*, 1998]. A time series of $PM_{2.5}$ sodium, chloride, and nitrate at Yosemite, though, strongly suggests that nitrate during YACS was often in the form of sodium nitrate rather than the commonly assumed ammonium nitrate (Figure 7.15). The assumption of nitrate in the form of NH_4NO_3, which is used in many studies and is part of the IMPROVE protocol, may have limitations in such cases. As will be seen later in examining the size distribution of inorganic species, NO_3^- was also observed to be largely in the coarse mode with Na^+ and Cl^-. These observations lead to the assumption of NO_3^- in the form of $NaNO_3$ used throughout this analysis.

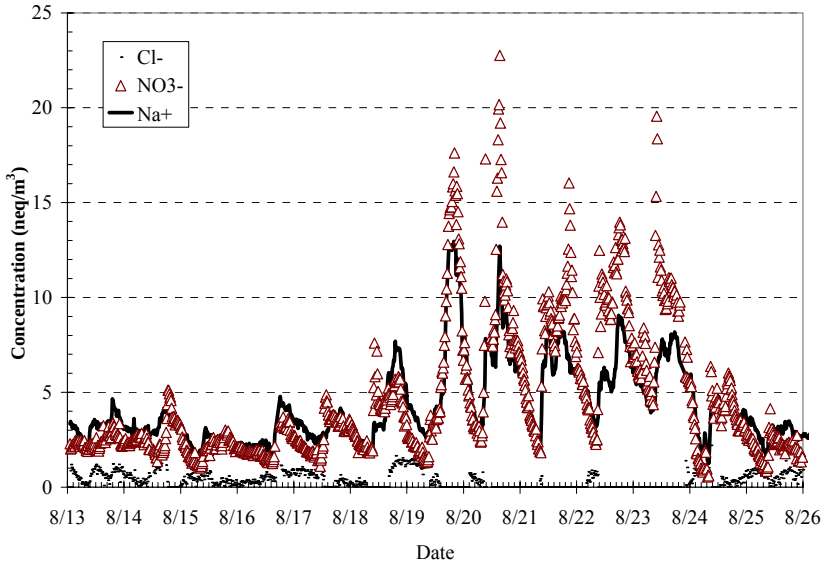

Figure 7.15 Time series of high time resolution chloride, nitrate, and sodium at Turtleback Dome, Yosemite, during YACS.

7.2.7 Size Distributions of Aerosol Ionic Components from MOUDI Measurements

Cascade impactor measurements give size-resolved speciation of the inorganic content of $PM_{2.5}$. The average MOUDI size distribution measured at Yosemite National Park in August 2002 is shown in Figure 7.16. Nitrate during the study was present predominately in the coarse mode as sodium nitrate, indicating a product of the reaction between gas phase nitric acid or its precursors and sea salt particles. When the concentration of NO_3^- meets or exceeds the concentration of Na^+, essentially complete displacement of Cl^- has occurred. Although some periods of ammonium nitrate were observed in the summer study at Yosemite, these were rare, despite the abundant emissions of ammonia from the neighboring San Joaquin valley.

Typical 24-hour average mass equivalent size distributions for selected ions from MOUDI measurements show an interesting structure evident in most samples (Figure 7.16). NH_4^+ and SO_4^{2-} ions are commonly found in the D_p = 0.1–2.0 μm size range and share a common mean diameter $D_{g,v}$ (0.5 μm) and standard deviation σ_g (1.7). Often though, both were present on the after-filter (D_p < 0.18 μm), which contained on average 27% and 31% of the SO_4^{2-} and NH_4^+, respectively. This strongly implies an ultra fine mode of ammoniated sulfate.

Size-segregated chemical composition is especially useful in determining aerosol optical properties. Given the observed general relationships between ionic species (Figure 7.16), three diameter size ranges, 0.3–0.7, 0.7–2.5, and 2.5–10.0 μm, were chosen to approximate the molecular species predominantly present in each size range (Figure 7.17). For the coarse mode, all nitrate and chloride were assumed to be in the form of sodium nitrate and sodium chloride. The sum of excess nitrate and sulfate correlates well with ammonium, calcium, and potassium; however, the relative mix of assorted species appears to change from one sampling period to the next. Therefore the mass sum of these ions is combined into a group called "remaining" mass. Remaining mass would be made up of ammonium sulfate, ammonium nitrate, calcium nitrate, calcium sulfate, or potassium sulfate, depending on the relative concentration of each ionic species. The inorganic aerosol in the fine mode is made up primarily of ammonium sulfate. The analysis of the ionic composition of the URG samples discussed previously suggests that remaining anion mass is probably associated with oxalate. The mid-range and coarse modes have more diverse composition. The largest mass fraction in the 0.7–2.5 μm size range is sodium nitrate at about 40%, with ammonium sulfate and sodium chloride making up an additional 24%, while the remaining is excess cations (Figure 7.17) [*Malm et al.*, 2005a].

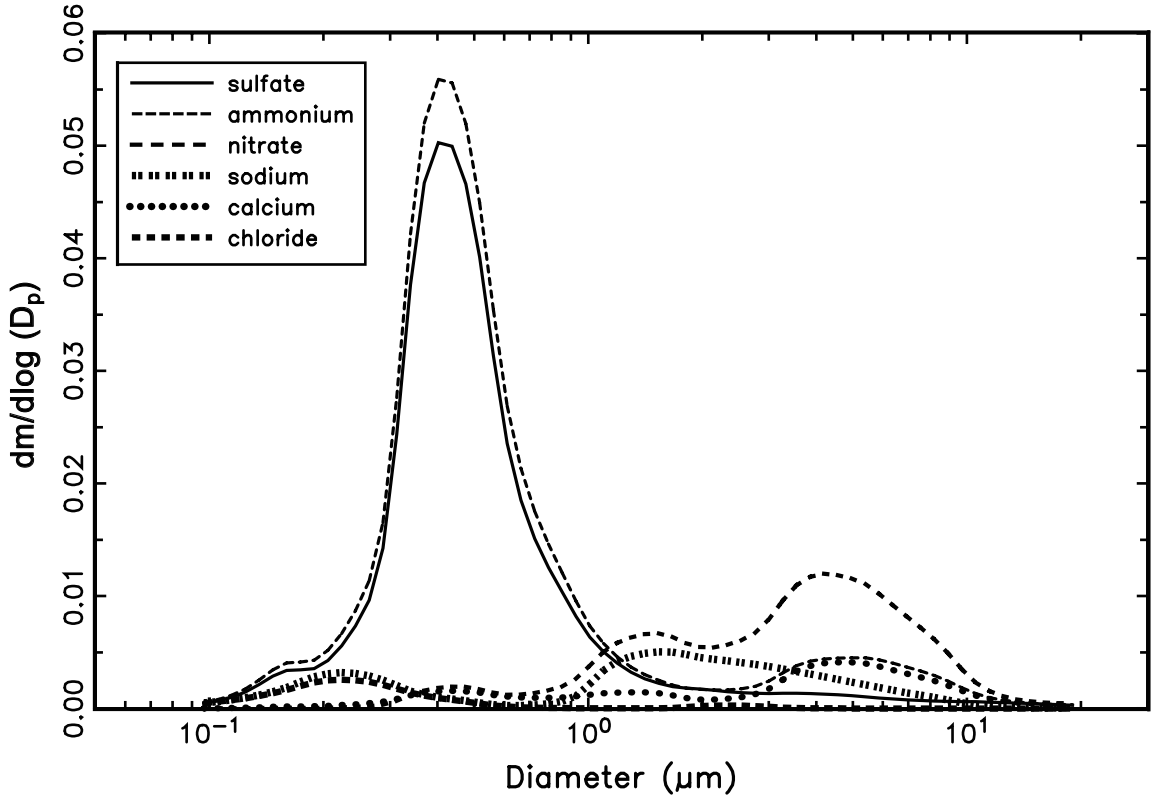

Figure 7.16 Equivalent mass size distribution of selected ions on 31 August 2002.

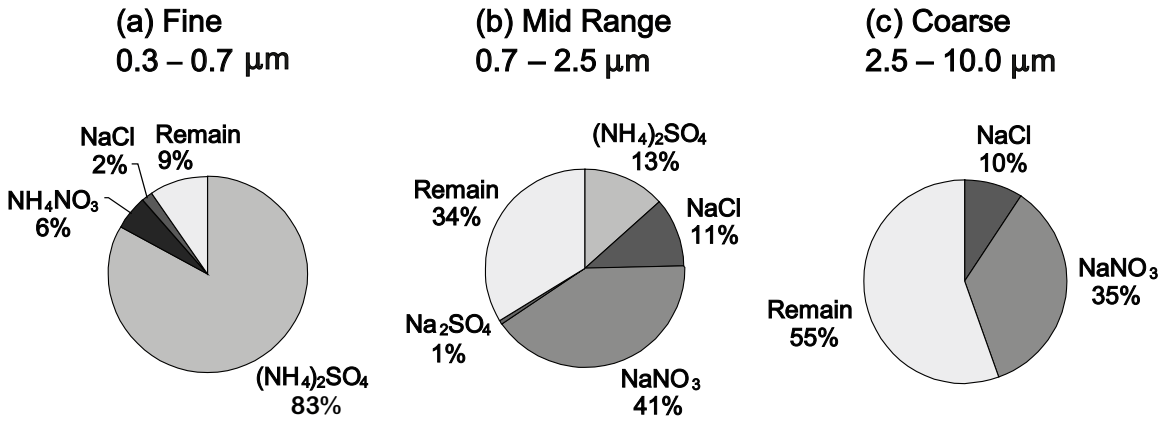

Figure 7.17 Ionic composition as a function of size range for aerosol sampled at Turtleback Dome.

7.2.8 Aerosol Number Concentrations and Size Distribution Characteristics

Total particle number concentrations (40 nm < D_p < 2.5 µm) exhibited a tremendous variability during YACS as shown in a timeline of integrated accumulation mode number and volume concentrations (Figure 7.18). Number concentrations (~ 15 min) range from hundreds of particles per cm^3, similar to background marine conditions, to over 7000 cm^{-3}, which might typify a regionally polluted location. Uncertainty in the number concentrations was on the order of 1%

[*McMeeking et al.*, 2005a]. High concentrations of sub-100 nm particles were responsible for the high total concentrations during the first two weeks of the study. On a daily basis, highest number concentrations occurred during the first two weeks of the study, typically peaking near midnight in the range of 4000–5000 cm^{-3}. Several other periods of particularly elevated number concentrations were observed during periods with possible local nighttime smoke on DOY 204–208 (23–27 July 2002) and DOY 238–239 (26–27 August) (Figure 7.18). The latter also featured a large peak in volume concentration.

Distinct periods of elevated volume concentration are evident around DOY 211 (30 July 2002) and particularly DOY 230 (18 August 2002), which have been classified as regional haze episodes. The overall mean and standard deviation of the accumulation mode volume concentration was 6.7 ± 3.9 $\mu m^3\ cm^{-3}$, with highest values, during the second regional haze event, peaking at ~ 27 $\mu m^3\ cm^{-3}$, while at times dropping as low as ~ 1 $\mu m^3\ cm^{-3}$. Mean volume concentrations and standard deviation during the first and second regional haze events were 7.9 ± 1.1 and 10.2 ± 4.6 $\mu m^3\ cm^{-3}$, respectively. Uncertainty in the integrated accumulation mode volume concentrations was on the order of 1–3% [*McMeeking et al.*, 2005a]. Interestingly, number concentration values are lower during the heavy regional haze smoke episode (Figure 7.18). However, the diurnal pattern during the early part of the experiment, with higher number concentrations typically observed at night, is still evident.

Based on merged size distribution measurements from DMA and OPC instruments, the structure of the size distributions of the fine mode aerosol may be examined over the range of 40 nm < D_p < 2.5 µm. Typically, a number mode centered near 100 nm was observed throughout the study (Figure 7.19). During the two regional haze episodes, number distributions became bimodal, particularly during the second episode around DOY 230. The larger mode was typically centered at $D_{g,v}$ = 0.4 µm, while the smaller mode was similar to the nearly ubiquitous number mode around D_p = 100 nm.

Contour plots in grayscale give a complete picture of the time variation of the size distribution, where darker shades indicate higher number or volume distribution concentrations (Figure 7.19, Figure 7.20). High concentrations of sub-100 nm particles (Figure 7.19) are largely responsible for high number concentrations observed during the first two weeks of the study (Figure 7.18). Bimodality emerging in the dry size distribution during the second smoke episode is apparent in mid-August as shown in Figure 7.19. The regional haze episodes are visible as shifts to larger

sizes, with high-volume distribution values near 0.3–0.5 μm from DOY 208–215 (27 July to 3 August) and DOY 222–234 (10–22 August). Aerosol coarse mode volume contributions for D_p > 1.0 μm are generally low except during the haziest period (~ DOY 226–234; 14–22 August), though still small compared to sub-micrometer contributions.

Accumulation mode volume mean geometric diameters ($D_{g,v}$) and standard deviations (σ_g) are shown as a time series in Figure 7.21. Uncertainties were less than 1% [*McMeeking et al.*, 2005a]. The study average $D_{g,v}$ was 0.28 ± 0.05 μm. During the second regional haze period in mid-August, mean $D_{g,v}$ was 0.32 ± 0.04 μm and at times as large as 0.4 μm (Figure 7.21). Smaller though more variable values of $D_{g,v}$ were observed during the first week of the study with the episodic presence of ultra fine particles with D_p < 100 nm. Average σ_g was 1.67 ± 0.11, with largest values observed during the first half of the study and lowest values observed during the second regional haze episode. The data show a strong inverse relationship between σ_g and $D_{g,v}$, with the lowest standard deviations corresponding to higher mean diameters (Figure 7.23). Increasing $D_{g,v}$ shows a strong relationship to increased aerosol volume concentrations (Figure 7.22). Overall, the influx of regional haze featured a shift to a larger but narrower mode of particles, which causes the elevated light scattering coefficient.

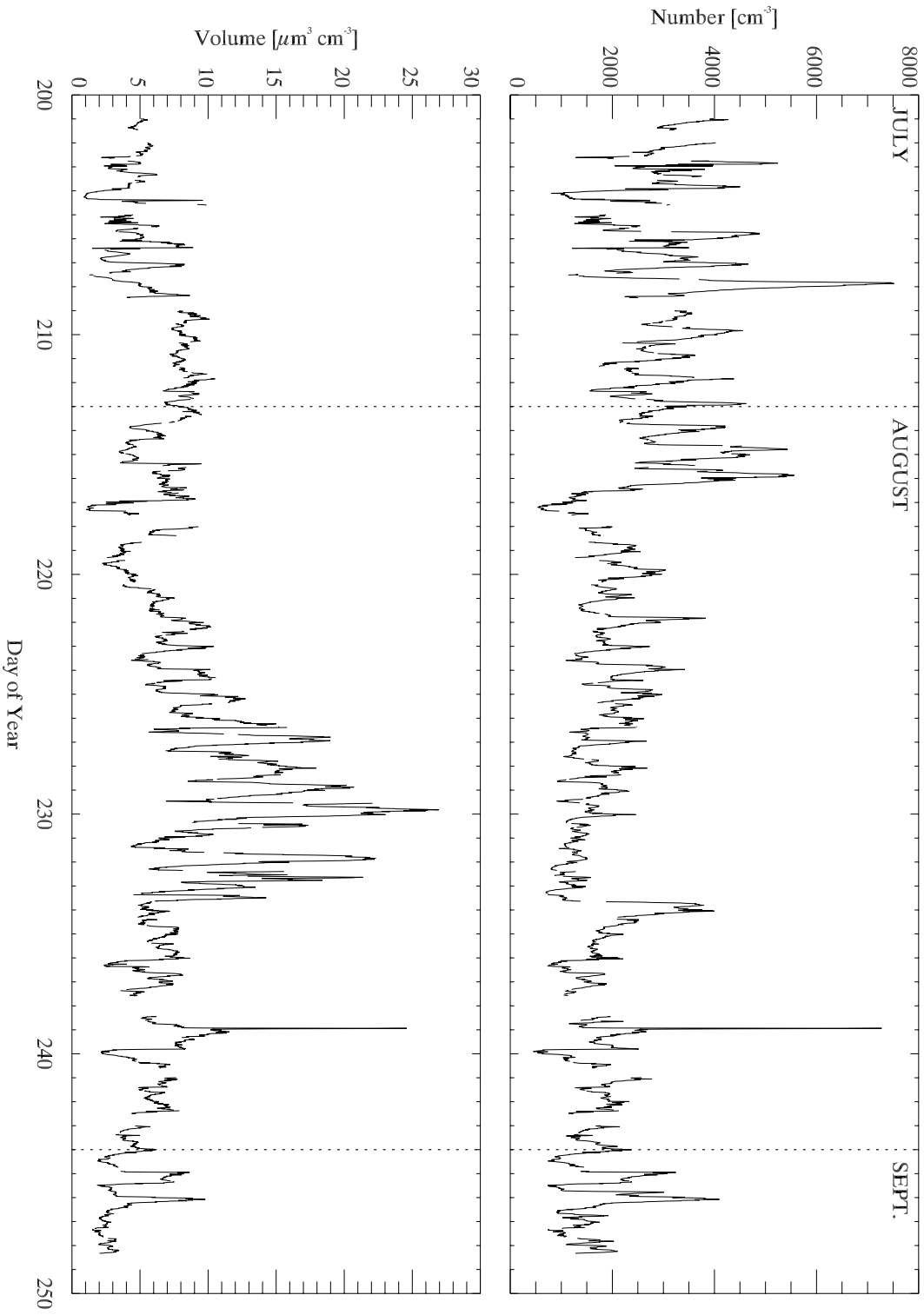

Figure 7.18 Timeline of total particle number concentration and aerosol volume (40 nm < Dp < 2.5 µm) during YACS.

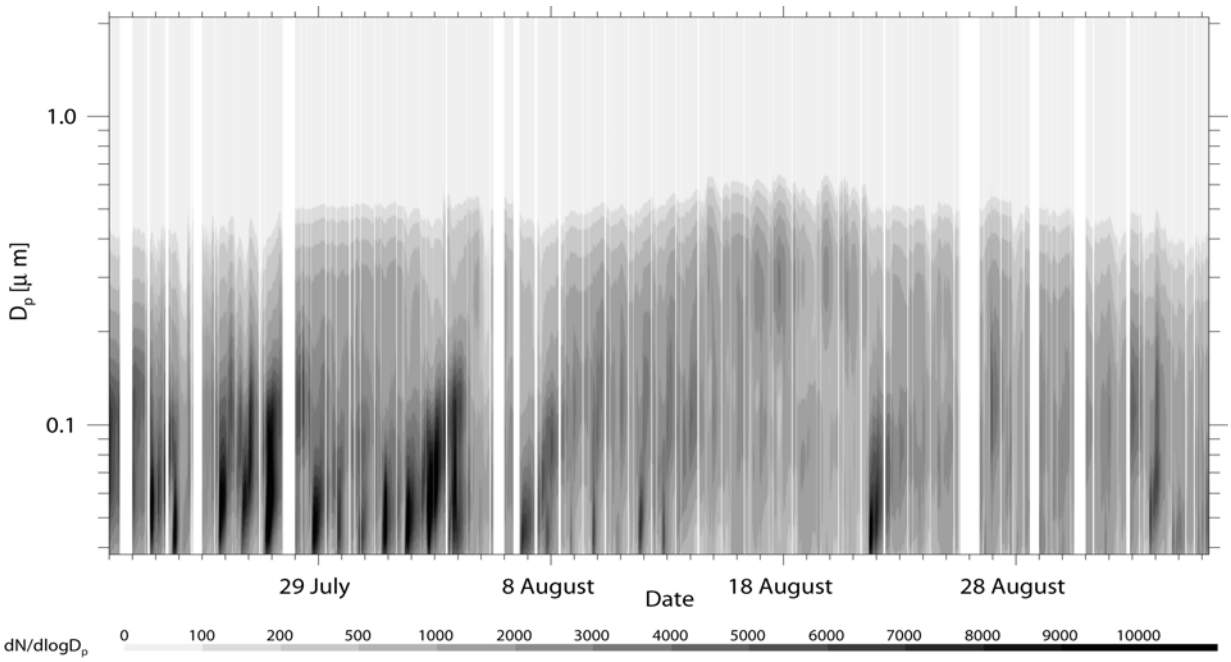

Figure 7.19 Contour plot timeline of aerosol number size distribution during YACS.

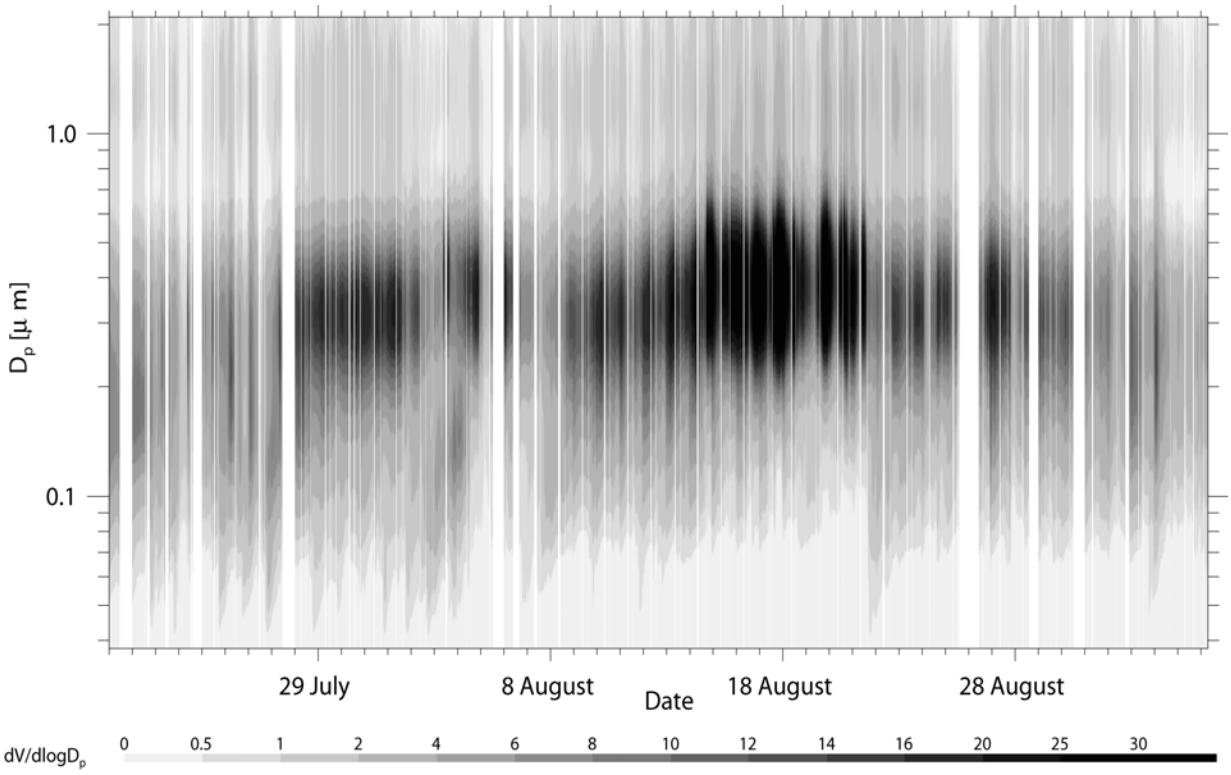

Figure 7.20 Contour plot timeline of aerosol volume size distribution during YACS.

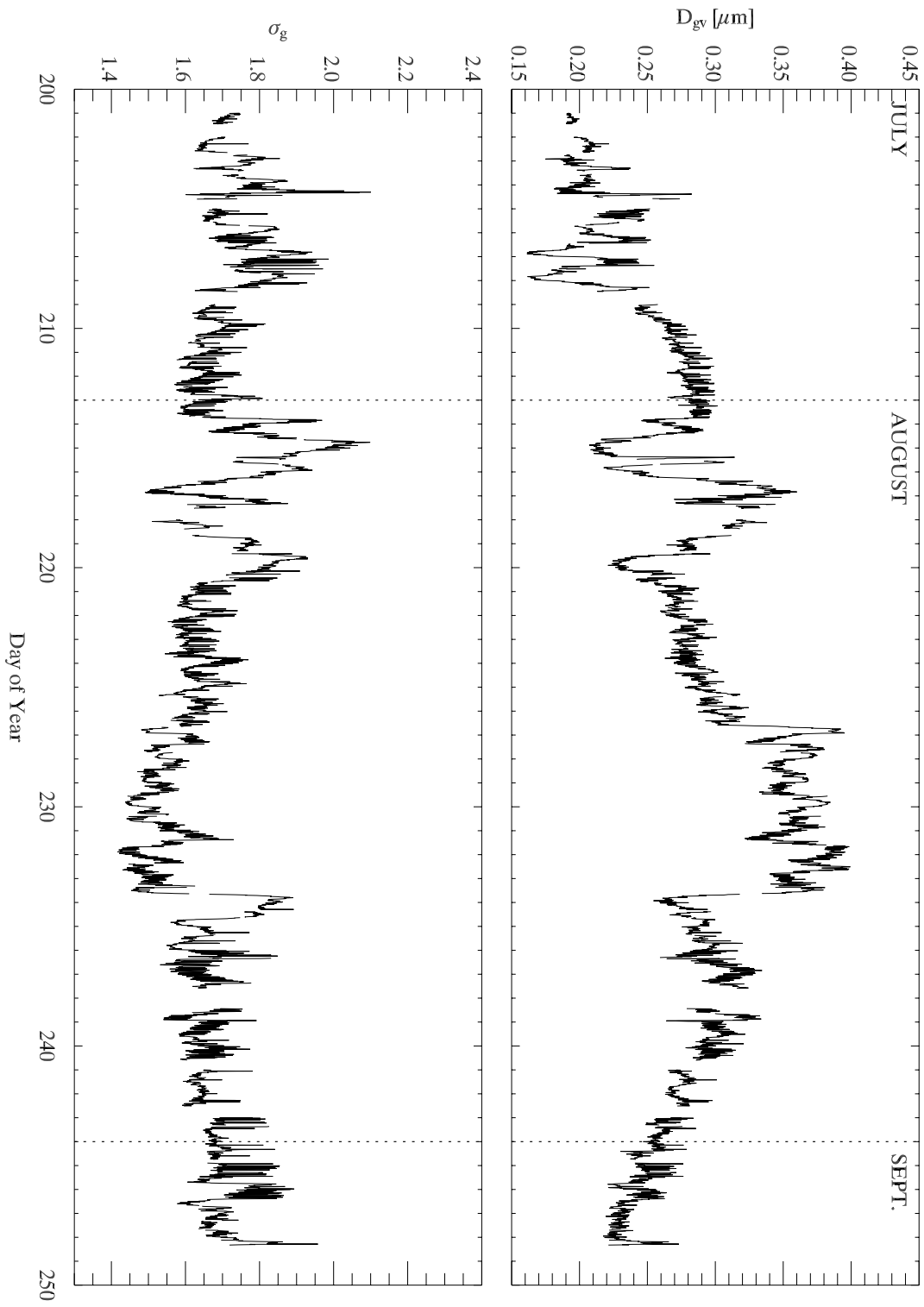

Figure 7.21 Timeline of geometric volume mean diameter and geometric standard deviation of the particle size distribution during YACS.

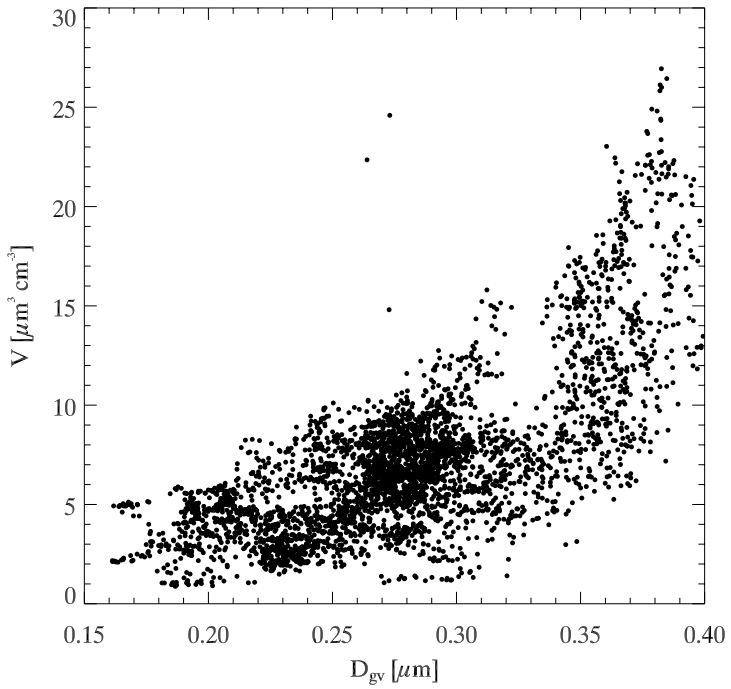

Figure 7.22 Relationship between geometric volume mean diameter and total aerosol volume concentration during YACS. Periods with high-volume concentrations featured a shift to larger particles.

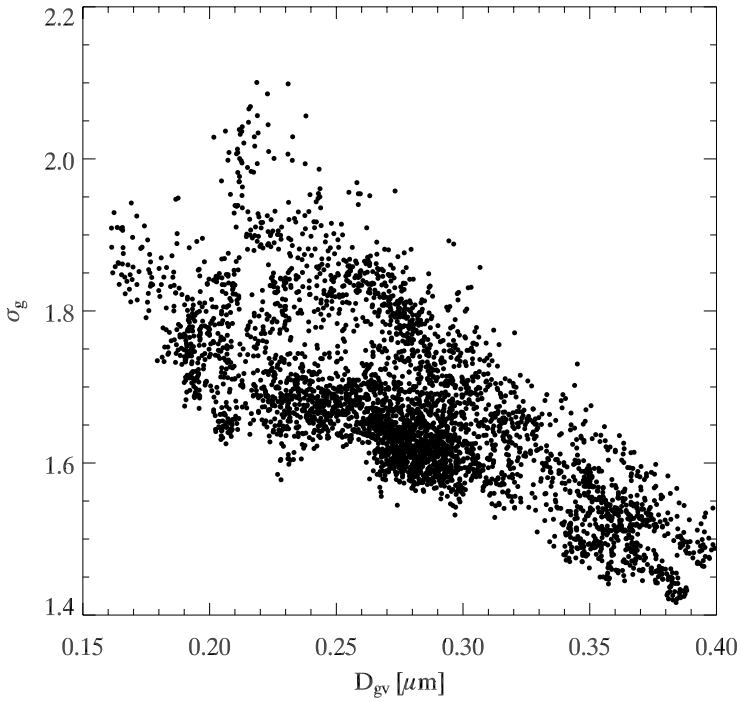

Figure 7.23 Relationship between geometric volume mean diameter and geometric standard deviation, which gives the width of the size distribution. Shifts to larger sizes were also accompanied by a narrowing of the size distribution.

7.2.9 Aerosol Refractive Index and Density

Estimates of refractive index were made from composition measurements using a volume-weighted mixing method and were compared to those retrieved by the alignment method [*McMeeking et al.*, 2005a]. Figure 7.24 shows a timeline of the refractive index retrieved by the alignment of the optical particle counter method, as well as the real and imaginary components calculated from chemical composition measurements. The mean and standard deviation of the retrieved refractive index was 1.577 ± 0.008, while the mean and standard deviation for the calculated was 1.570 ± 0.006 for the real part of the calculated refractive index. Overall, there was little variation in either retrieved or calculated refractive index, reflecting the nearly continual presence of a dominant organic carbon mass fraction. Best agreement was found during the early and late periods of the study when POM was less dominant. A larger difference between retrieved and modeled refractive index was observed during the carbon-dominated periods (1–2%), though within the experimental uncertainties. This is likely due to a low assumption of the refractive index for POM in the mixing model. The average imaginary part of the calculated index of refraction was 0.015 ± 0.003, and highest values were observed during the early and late periods of the study, reflecting a larger contribution by BC to total $PM_{2.5}$.

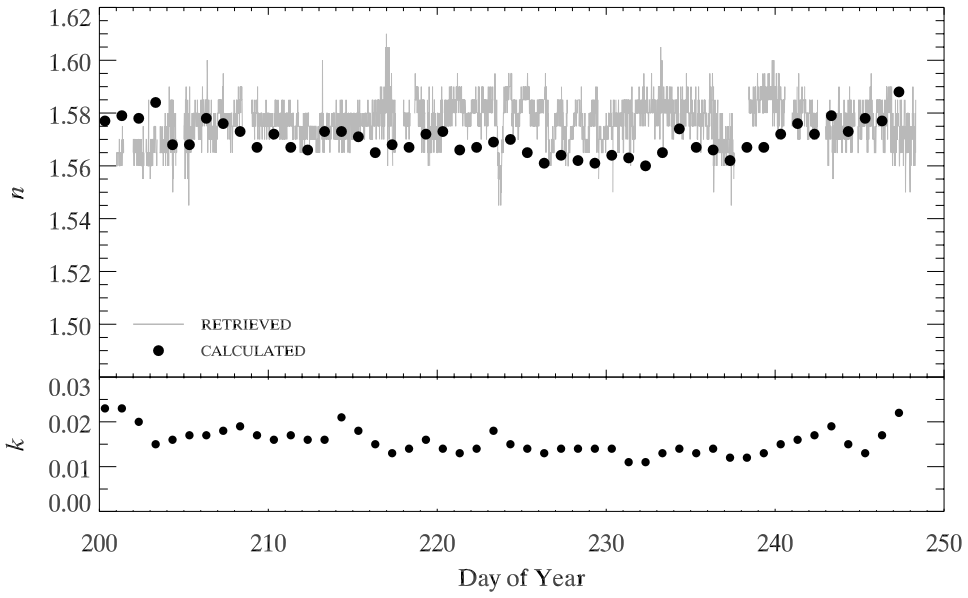

Figure 7.24 Timeline of retrieved real and imaginary part of aerosol refractive index during YACS.

7.2.10 Visibility and Optical Properties at Turtleback Dome, Yosemite, during YACS

Perception and enjoyment of landscapes in scenic areas is critically dependent on the ambient aerosol's light scattering and absorption characteristics. Episodic high $PM_{2.5}$ aerosol concentrations during YACS resulted in pronounced impacts on visibility (Figure 7.25). Ambient light extinction, b_{ext}, was measured with an Optec LPV2 transmissometer, which has an effective wavelength of 550 nm. Dry aerosol light scattering, b_{sp}, was measured with a Radiance Research M903 nephelometer, which has an effective wavelength of 530 nm. The difference in light scattering by gases at these two wavelengths is about 14%; however, based on an Ångström exponent of 2 for a typical accumulation mode dominated aerosol (as was the case during YACS) the difference would be ~ 7%. To compare the Optec transmissometer measurements with the Radiance Research nephelometer measurements, the nephelometer was normalized to 550 nm by a 7% reduction for cases with ambient RH < 30%. The comparison shows very similar values and $R^2 > 0.99$ for multiple instruments. The difference between the average normalized dry and ambient light scattering coefficients by particles is ~ 2.6 Mm^{-1}, which is within the nephelometer uncertainty estimate of 7% [*Anderson et al.*, 1996]. This small difference is consistent with low average ambient RH during the study and little observed hygroscopic growth at ambient RH.

Figure 7.25 Comparison of good and bad visibility days at Turtleback Dome.

Time series of light extinction and scattering show large temporal variability with total light extinction coefficients approaching the Rayleigh scattering limit during the beginning and end of the experiment and exceeding 200 Mm^{-1} during the haziest periods (Figure 7.27). The smoke episode of mid-August (~ DOY 230) shows a broad pronounced peak in the light scattering coefficient, which lasted approximately two weeks (Figure 7.27). Total light extinction during this period was dominated by light scattering associated with fine particles ($D_p < 2.5$ μm). This smoke episode was clearly evident from the physical and chemical measurements previously discussed (Figure 7.11, Figure 7.13). The average light extinction coefficient during the entire YACS study of 50 ± 40 Mm^{-1} is over three times greater than the EPA estimate annual average for "natural background" conditions of 15.8 Mm^{-1} [*United States Environmental Protection Agency*, 2003b] (Table 7.7). The difference between PM_{10} and $PM_{2.5}$ light scattering is small at 1.46 Mm^{-1}, actually smaller than nephelometer uncertainties [*Anderson et al.*, 1996], and shows the dominance of the fine mode to optical properties. In measuring PM_{10}, a nephelometer underestimates coarse particle scattering by up to a factor of 2, largely due to the limited angular range of the measurement [*Anderson et al.*, 1996]. Therefore average coarse particle scattering is likely ~ 3 Mm^{-1}. Based on the average coarse mass concentration of 7.5 $\mu g/m^3$ and assuming a coarse mass scattering efficiency of 0.6 m^2/g as per IMPROVE protocols, the light scattering coefficient due to coarse particles is estimated as a similarly low value of 4.5 Mm^{-1}. Either estimate demonstrates a very modest coarse mode contribution to light extinction during YACS. Differencing light extinction measured by the transmissometer and light scattering measured by the nephelometer (plus 1.5 Mm^{-1} to account for nephelometer large particle truncation error) leaves 9.7 Mm^{-1} attributed to light absorption. Thus a rough extinction budget yields 75% of extinction attributed to dry fine particle scattering, 6% is coarse particle scattering, 14% is light absorption, and 5% is scattering due to absorbed water primarily associated with the fine mode aerosol.

Table 7.7 Average aerosol optical properties at Turtleback Dome during YACS (n = 5606).

Variable	Mean	Std Dev	Minimum	Maximum
RH	33.51	10.62	9.25	82.40
b_{sp} _10	41.37	28.91	6.06	192.83
b_{sp} _2.5	39.91	28.86	5.58	190.69
b_{sp} _dry	37.28	28.99	5.23	189.85
b_{ext}	49.60	39.78	3.83	448.00

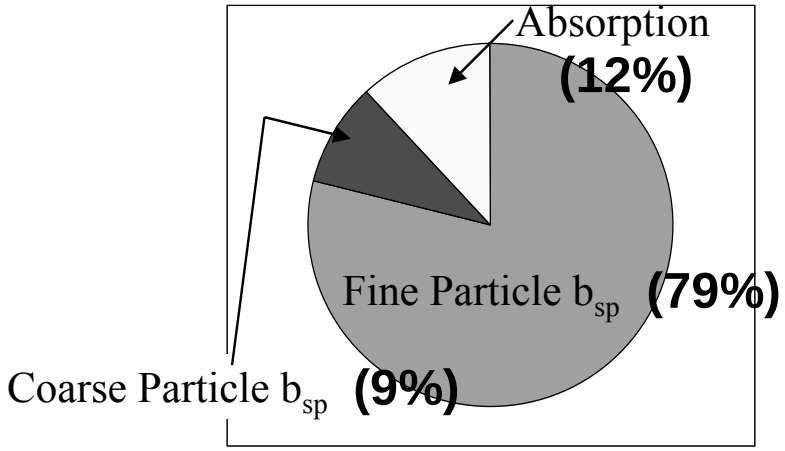

Figure 7.26 Budget of light extinction by particles during YACS.

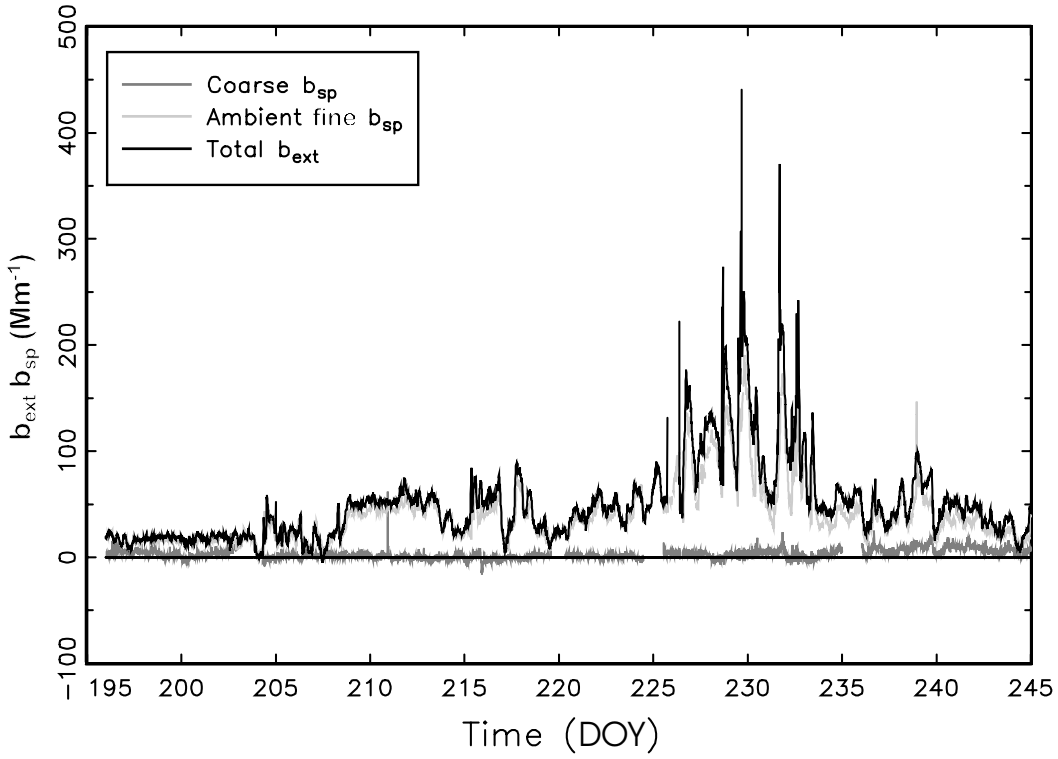

Figure 7.27 Time series of light extinction and scattering during YACS.

7.2.11 Measured versus Modeled Aerosol Optical Properties: Light Scattering Closure

In this section, closure between nephelometer measured and calculated particle light scattering coefficients for $PM_{2.5}$ is explored. The objectives of these calculations are twofold in assessing both the accuracy of aerosol measurements and the ability to estimate aerosol optical properties from independent measurements. Previously, harmony comparisons found better agreement between gravimetric and reconstructed mass with IMPROVE TOR carbon as compared with the

semi-continuous R&P 5400 instrument. Thus, a further interest is examining the discrepancies in carbon measurements with the measured and calculated light scattering.

According to standard IMPROVE protocols, $PM_{2.5}$ at most continental sites can be classified into five major types: sulfates (SO_4^{2-}), nitrates (NO_3^-), POM, elemental or light-absorbing carbon (EC), and soil dust. The IMPROVE protocol for reconstruction of light scattering by particles gives an estimate of light scattering based on these species concentrations and typical mass scattering efficiencies [*Malm et al.*, 1994]. Based on the PILS and MOUDI measurements described above, $NaNO_3$ was found to be the predominant NO_3^- species; therefore the IMPROVE equation for calculating dry scattering is expressed as

$$bsp = (3)[(NH4)2\,SO_4] + (1)[NaNO_3] + (4)[OMC] + (1)[SOIL]$$

Light scattering is also calculated under the assumption of homogenously mixed spherical particles using Mie light scattering theory. These calculations use inputs of the measured size distribution and refractive index estimated from the hourly chemical composition [*Malm et al.*, 2005a; *McMeeking et al.*, 2005a]. Agreement between reconstructed and measured scattering shows substantially better agreement using Mie theory, suggesting that the standard mass scattering efficiencies assumed above are not universally applicable (Figure 7.28). A scatter plot of measured dry scattering and calculated aerosol scattering, using semi-continuous R&P 5400 carbon measurements without normalizing to the 24-hour bulk TOR carbon measurements from IMPROVE filters, is given in Figure 7.29. This shows similar biases for low and high scattering that were observed with the previous mass reconstructions (Figure 7.6) where aerosol scattering is overestimated by almost 100% at low scattering values, while at higher scattering values aerosol scattering is underestimated by about 25%. The over- and underestimation is apparently related to the R&P carbon measurement uncertainty, imprecision, or, possibly, absorbed organic gases.

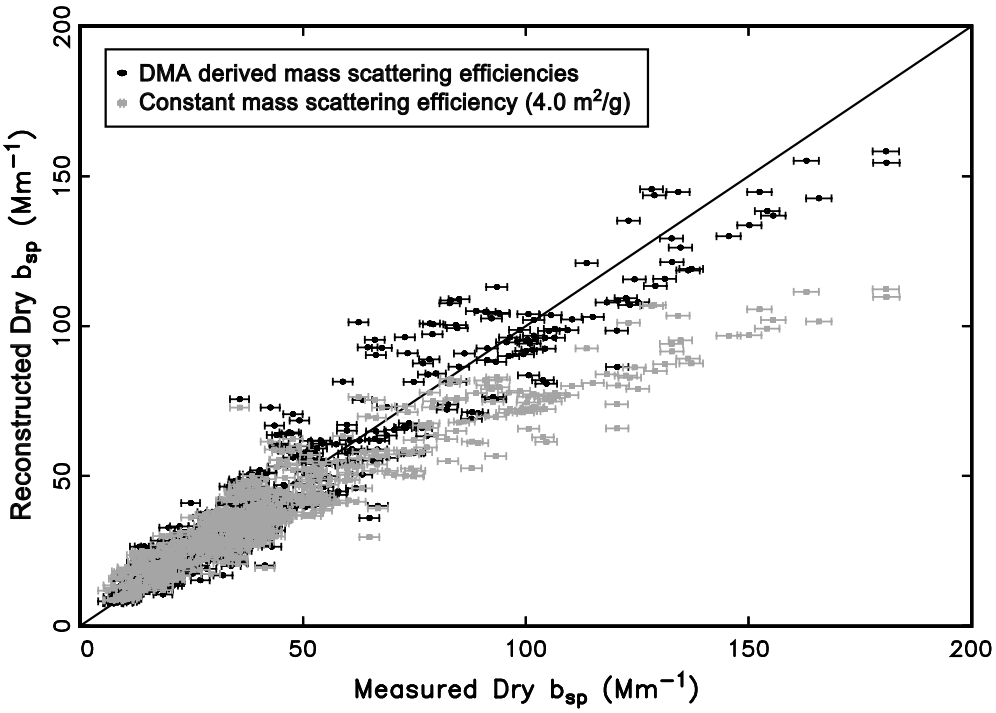

Figure 7.28 Scatter plot of calculated versus measured scattering assuming 4.0 m^2/g and 3.0 m^2/g for POM and sulfate and using DMA-determined mass scattering efficiencies.

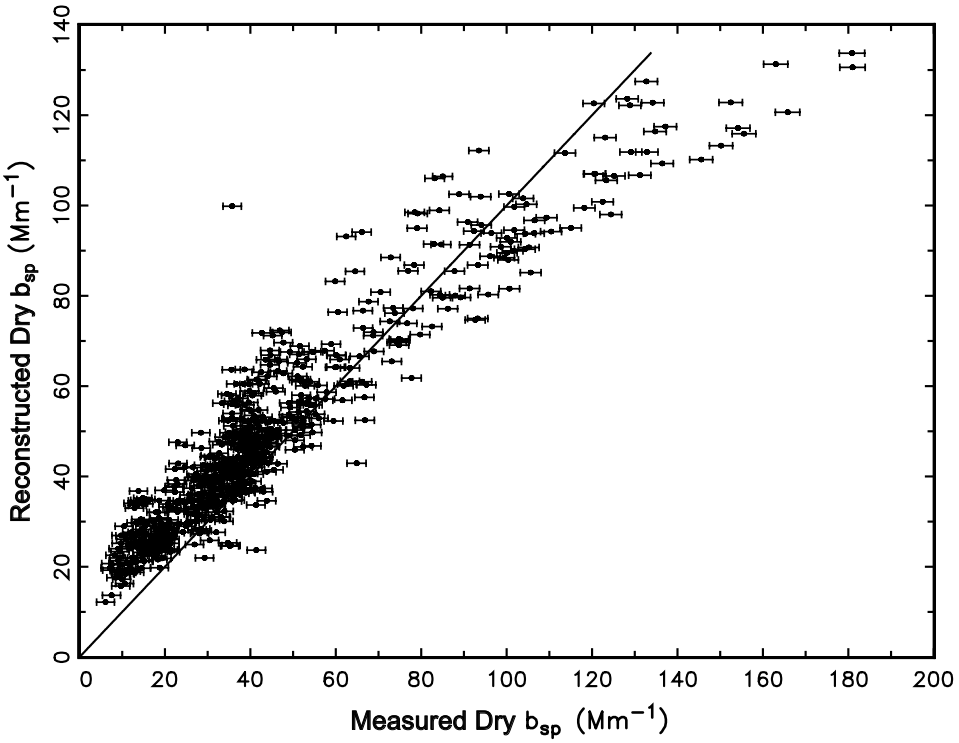

Figure 7.29 Scatter plot of aerosol versus measured scattering assuming DMA-derived mass concentrations and 1.8*R&P carbon concentrations.

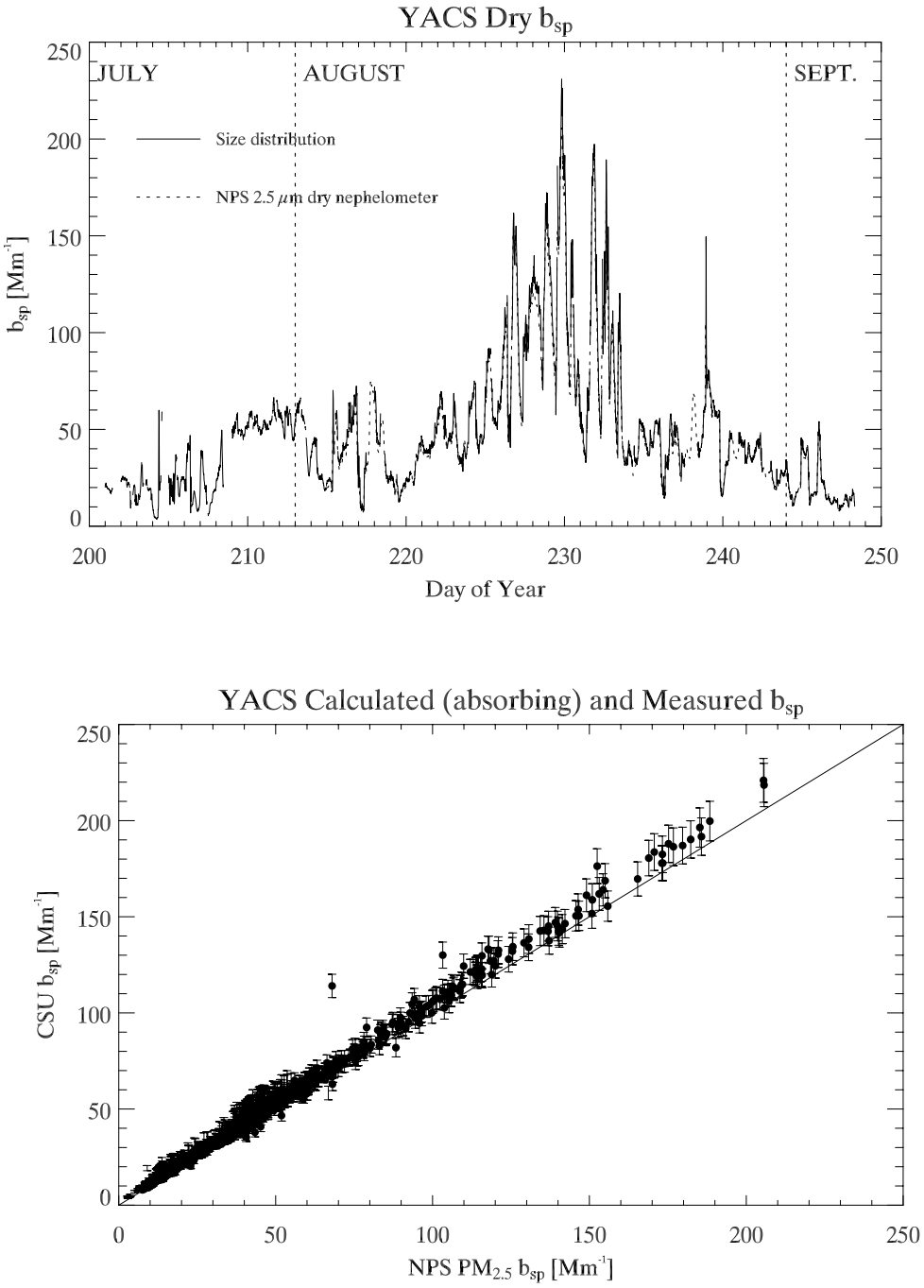

Figure 7.30 Time series and scatter plots of calculated (CSU) versus measured (NPS) scattering, using 15-minute size distributions from DMA, retrieved real refractive index, and mixing model calculated imaginary refractive index.

Using the 15-minute average size distributions, retrieved real refractive index, and imaginary refractive index from aethalometer measurements of black carbon and a mixing model shows the strongest agreement between measured and calculated light scattering (Figure 7.30) [*McMeeking et al.*, 2005b]. In this case no assumptions have to be made regarding the real refractive index of

POM or EC, and the highest time resolution measurements are used, showing the utility of this information for light scattering calculations.

Calculation of the mass scattering efficiency of the bulk $PM_{2.5}$ shows a wide range of values, largely a result of the changing size distribution (Figure 7.31). Calculated scattering coefficients were divided by the aerosol mass concentration integrated over the measured size distribution derived to determine mass scattering efficiencies (α_s). Average α_s during YACS was 4.3 ± 0.8 m^2 g^{-1} and varied between 3 and 6 m^2 g^{-1} (Figure 7.31). Highest values were found to occur in mid-August during the most pronounced smoke episode (Figure 7.31). The values of α_s are 30–50% greater than the value of 4.0 m^2/g assigned to POM under IMPROVE protocols [*United States Environmental Protection Agency*, 2003a, 2003b]. Estimating uncertainties with mass scattering efficiencies is difficult as a result of assumptions in the calculations, including the aerosol mixing state and the complex index of refraction for EC [*Fuller et al.*, 1999]. For example, scanning electron microscope measurements, as will be discussed later, shows a complex variety of mixing states during YACS [*Hand et al.*, 2005]. Nonetheless, these results suggest that the POM aerosol during YACS, and particularly dry, aged smoke aerosol particles, scatter light very efficiently.

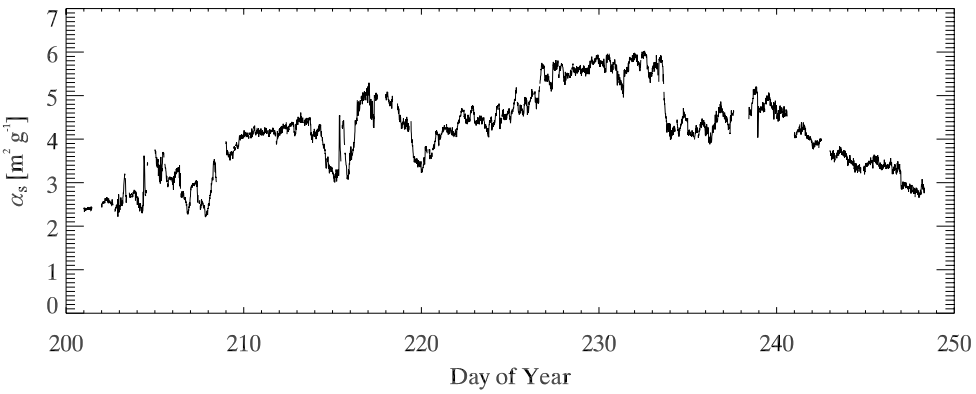

Figure 7.31 Timeline of bulk $PM_{2.5}$ mass scattering efficiency.

A light scattering contour plot during YACS, calculated using merged size distribution data, shows that particles $0.25 < D_p < 0.6$ µm contribute the vast majority to dry light scattering [*McMeeking et al.*, 2005a] (Figure 7.32). There was a very small contribution to light scattering by particles larger than 1.0 µm during the study. An intense peak in light scattering is observed during the mid-August regional smoke-haze period. As discussed previously, this period also featured a clear shift to a larger, narrower mode of particles (Figure 7.21) dominated by POM.

The mean light scattering diameter reaches 0.4 μm during mid-August, whereas it varies from 0.3 to 0.35 μm elsewhere.

Table 7.8 Statistical summary of dry measured light scattering by $PM_{2.5}$, reconstructed aerosol scattering, and the scattering from each species (parenthetical values are the approximate contribution of each aerosol species to reconstructed scattering (n = 661 samples)).

Variable	Mean	Std Dev	Minimum	Maximum
$b_{sp,measured}$	43.02	29.01	7.48	158.29
$b_{sp,aerosol}$	43.77	29.93	6.07	180.97
SO_4	5.54 (12.7)	2.38	1.86	13.98
NO_3	0.34 (0.8)	0.29	0.04	2.41
POM	36.53 (83.5)	28.34	2.27	152.39
SOIL	0.62 (1.4)	0.17	0.29	0.94

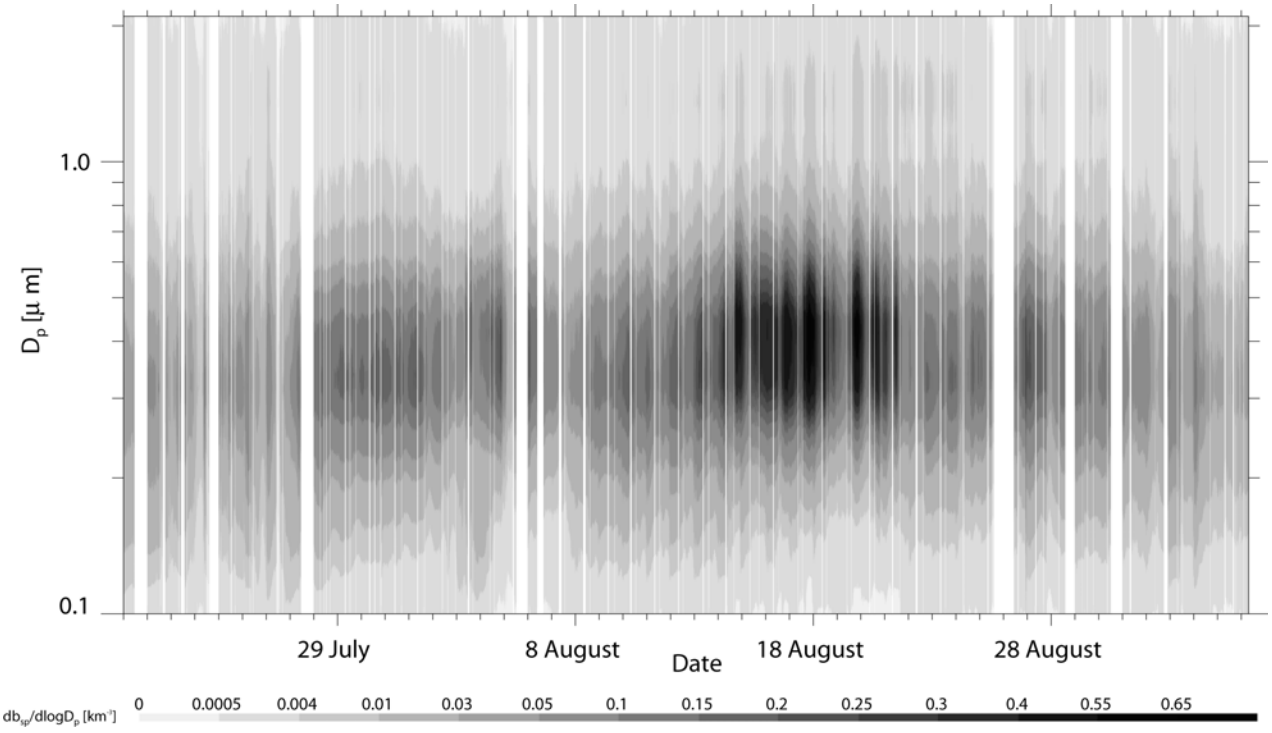

Figure 7.32 Contour plot timeline of light scattering distribution calculated based on measured size distributions.

7.3 Detailed Aerosol Physio-Chemical Properties

7.3.1 Aerosol Hygroscopic Properties: Diameter Growth Factors

Water uptake properties of inorganic aerosols have been extensively measured, and a number of equilibrium models describing these properties as a function of inorganic ion mixtures have been developed [*Clegg et al.*, 1998; *Nenes et al.*, 1999]. Laboratory experiments on mixtures of salts with organic species show a lowering of hygroscopic growth and the smoothing of clear deliquescence points with an increasing organic fraction [*Hansson et al.*, 1998; *Ansari and Pandis*, 2000; *Prenni et al.*, 2003]. Less well characterized are the hygroscopic properties of POM, particularly the diverse mixture of species found in the ambient environment. In order to investigate the hygroscopic properties of a POM-dominated and smoke-influenced aerosol, two techniques were employed during YACS [*Carrico et al.*, 2005; *Malm et al.*, 2005b].

Measurements of particle diameter growth factors were performed with a humidified tandem differential mobility analyzer (HTDMA). Measurable water uptake began at intermediate RH (40–70%) with average D(RH = 40, 60, and 70%)/D_o = 1.01, 1.03, and 1.06, respectively, for 200 nm particles (Figure 7.33). Beyond RH = 80%, the particles continued to take up water, though relatively weakly, with ensemble D(RH = 80% and 90%)/D_o of 1.15 ± 0.05 and 1.31 ± 0.06, respectively, for 200 nm particles. Slightly larger D/D_o values were observed for 100 nm particles. Observed hygroscopic growth for the Yosemite POM-dominated aerosol was much lower than that for salts such as $(NH_4)_2SO_4$ and NaCl that typically compose ambient aerosols in polluted and marine environments. D/D_o at the average ambient RH of 33% was estimated to be below the detection limit (1.02) for the sizes considered here, suggesting a very small contribution by aerosol phase water to light extinction for this site and conditions.

With diameter growth measurements, both monomodal and bimodal growth profiles were observed, with bimodal dominating the 200 nm particles (68%). Separation into more and less hygroscopic modes occurred near RH = 80%. D(RH = 80%) /D_o was 1.29 ± 0.08 and 1.11 ± 0.04 for more and less hygroscopic modes for 200 nm particles. Water uptake by 100 and 200 nm particles was overall very similar, though differences in the fraction of particles in less and more hygroscopic modes lead to a lower ensemble D/D_o for 200 nm. Trimodal profiles with modes nearly as hygroscopic as pure $(NH_4)_2SO_4$, nearly hygrophobic, and similar to the experiment average hygroscopicity were observed twice during changing aerosol composition.

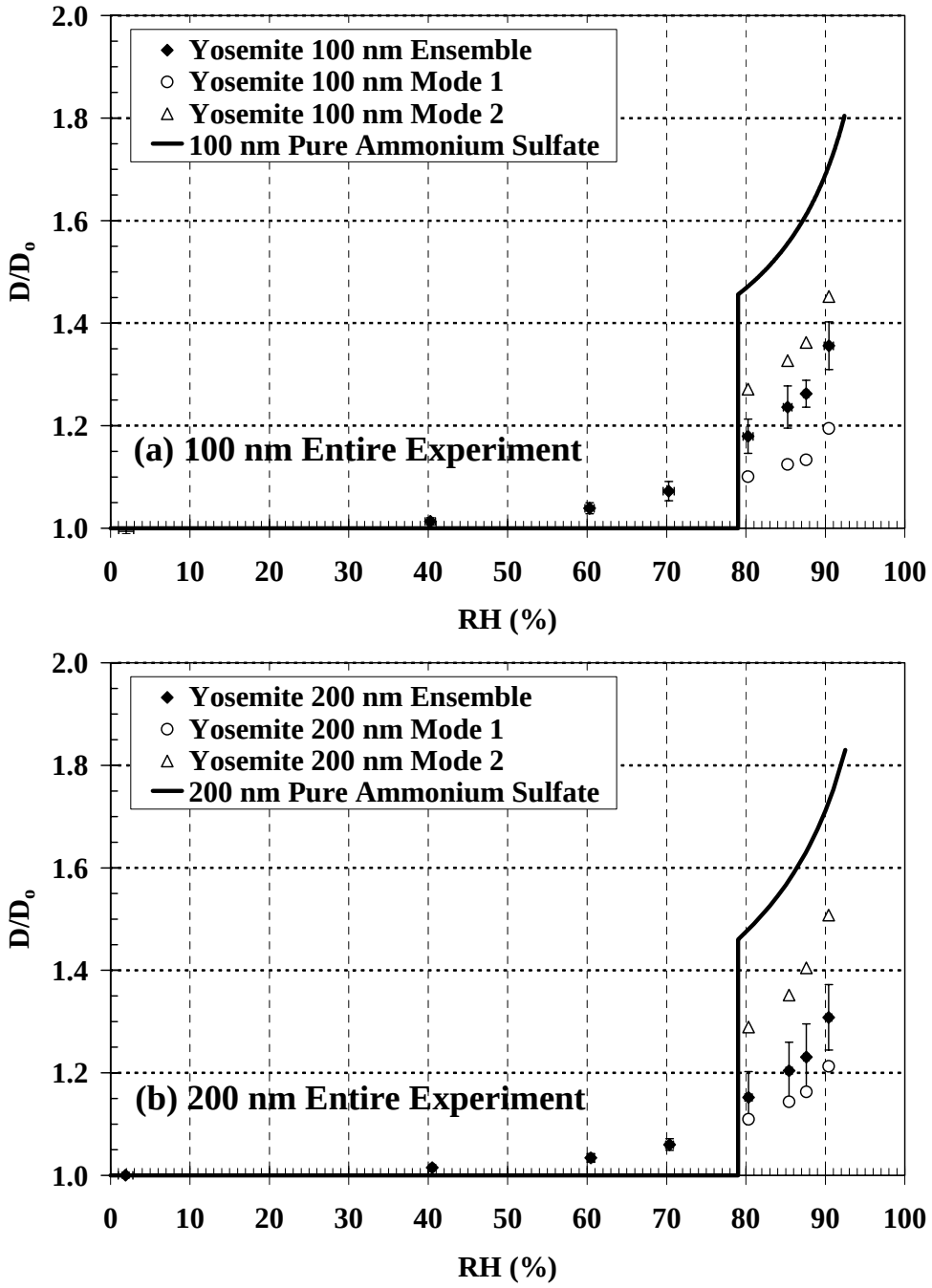

Figure 7.33 Experiment average mean and standard deviation diameter growth factors (D(RH)/Do) versus RH for (a) 100 nm particles and (b) 200 nm particles. Averages are shown for the less hygroscopic and more hygroscopic modes and an ensemble D/Do. In comparison is the theoretical growth curve for pure (NH4)2SO4. Standard deviations for D/Do and RH are shown.

Time series of D(RH = 80%)/D_o for 200nm dry particles are shown in Figure 7.34 along with the carbon mass fraction, an indicator of aerosol chemical composition. D/D_o is given independently for the less (mode 1) and more (mode 2) hygroscopic aerosol as well as an ensemble based on a cubic weighting of the modes. Also indicated qualitatively on the top and bottom margins of the

time series is whether the aerosol hygroscopic growth showed strongly deliquescent features. Overall, the middle of August (DOY 225–230) featured the largest POM contribution. It also featured the lowest $D(RH = 80\%)/D_o$, and typically monotonic rather than deliquescent growth.

A comparison of ensemble $D(RH = 80\%)/D_o$ versus the mass ratio of POM to total inorganics (primarily SO_4^{2-}, NH_4^+, and NO_3^-) shows decreasing hygroscopicity with increasing POM fraction (Figure 7.35). As the POM/ionic mass ratio exceeded 10, $D(RH = 80\%)/D_o$ approached 1.1. It should be noted that POM was a large fraction for most periods of HTDMA measurements. Only on DOY 247 (4 September 2002) was the ionic fraction greater than the POM fraction and, consequently, this day featured the largest D/D_o measured during YACS, as shown previously in the time series (Figure 7.34). Concurrent RH-controlled light scattering measurements likewise showed lower hygroscopic growth during POM-dominated periods [*Carrico et al.*, 2005; *Malm et al.*, 2005b]. A number of markers can be examined in relation to the hygroscopicity to explore the influence of biomass smoke. The difference between ultraviolet UV (350 nm) and near infrared IR (880 nm) light absorption as measured with a duel-wavelength aethalometer (UV-IR, expressed in terms of the BC measurement unit of μgm^{-3}) is a qualitative indicator for biomass smoke. This is thought to be due to the enhanced UV absorption associated with POM components that are found in wood smoke such as aromatic compounds (www.mageesci.com). Biomass burning also releases a large amount of potassium-rich submicrometer particles and thus the presence of nonseasalt soluble K^+ is also a smoke marker [*Andreae*, 1983; *Ma et al.*, 2003]. From these markers, the large peak in POM during mid-August also featured a strong contribution from biomass smoke (Figure 7.34), which from transport evidence was associated with massive wildfires in Oregon. Comparison of UV-IR averaged over the periods of D/D_o measurements shows a similar relationship to the POM/ionic mass ratio (Figure 7.35c,d). A higher POM fraction and periods of smoke influence (often coinciding during YACS) are both associated with decreasing hygroscopicity, particularly for 200 nm particles (Figure 7.35). Ensemble $D(RH = 80\%)/D_o$ gives linear correlations with POM, POM/ions, aethalometer UV-IR, and soluble K^+ of $-0.74 < R < -0.59$ for 200 nm and $-0.49 < R < -0.25$ for 100 nm particles. Stronger relationships for 200 nm and a dominant, less hygroscopic mode are likely related to a greater POM fraction in this size range (Figure 7.35).

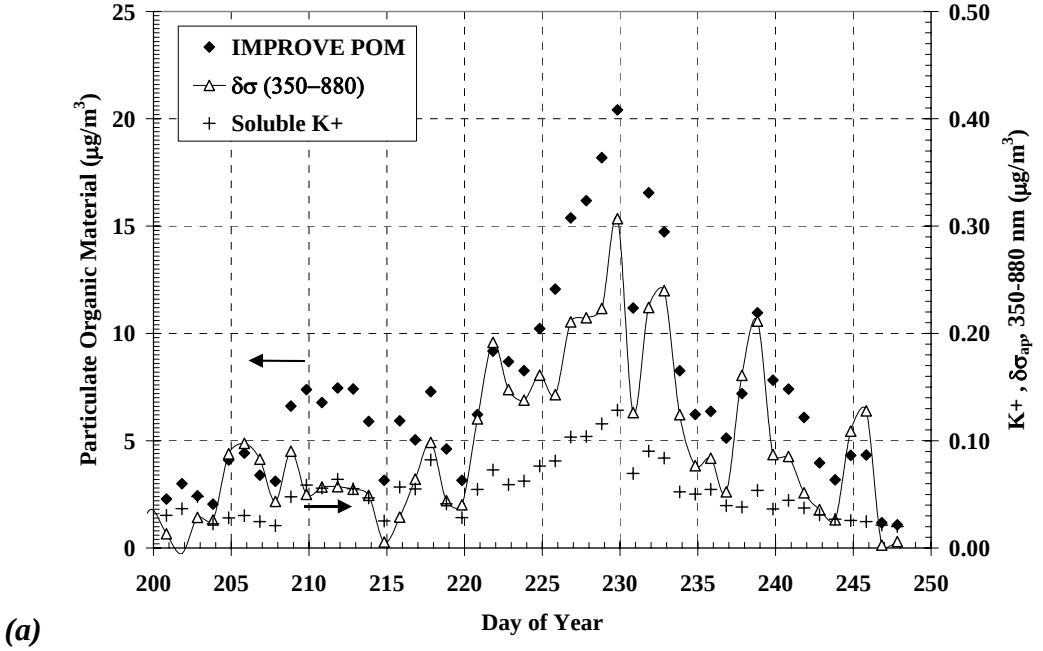

(a)

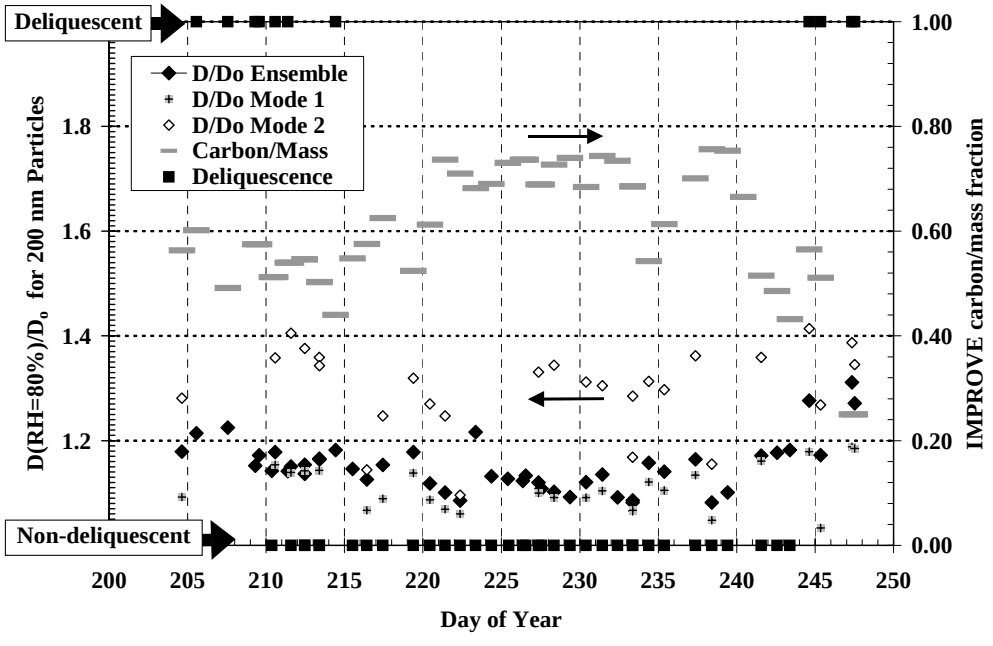

(b)

Figure 7.34 Time series (a) of 24-hour average POM (from 24-hour IMPROVE sampler assuming a carbon to POM multiplier of 1.8), soluble potassium (K+, 24-hour URG filter samples), and the difference in UV and IR wavelength measurements of "black carbon" from an aethalometer (350–880 nm). Time series (b) of D/Do (80%) for 200 nm particles, $PM_{2.5}$ carbon/$PM_{2.5}$ mass (IMPROVE), and a qualitative indicator for the observation of deliquescent hygroscopic growth for 200 nm particles.

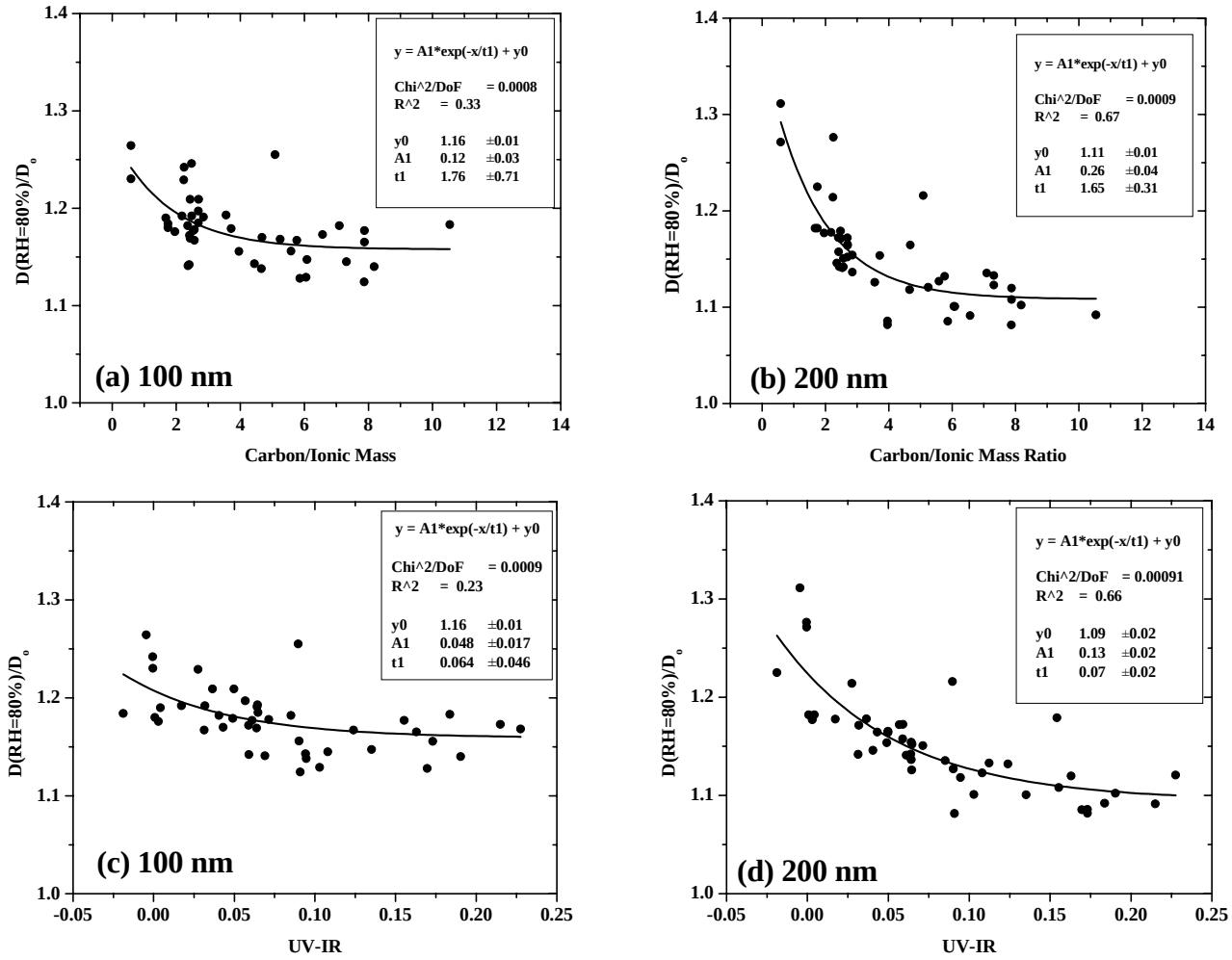

Figure 7.35 Comparison of diameter growth factors (D/Do (RH = 80%)) for (a) 100 nm and (b) 200 nm particles versus the 24-hour average ratio of POM (from 24-hour IMPROVE samples) to ionic mass concentration (from 24-hour URG filter measurements) for $PM_{2.5}$ and versus the difference in aethalometer 350 nm and 880 nm absorption (UV-IR) for (c) 100 nm and (d) 200 nm particles.

7.3.2 Aerosol Hygroscopic Properties: Growth in Light Scattering as a Function of RH

Using a controlled RH nephelometery system, the dependence of the total light scattering coefficient on relative humidity (*f*(RH)) was measured [*Day et al.*, 2000; *Day and Malm*, 2001; *Malm et al.*, 2005b]. Daily *f*(RH) curves were measured and exhibited a wide range of hygroscopic behavior. At times, particularly during the smoke episode of mid-August, very little hygroscopic growth was observed. Other times featured fairly strong hygroscopicity with a strong indication of deliquescent behavior (Figure 7.36). During select periods, measurements of *f*(RH) were conducted on both the upper and lower branches of the aerosol growth hysteresis loop. Observations during the ACE-Asia campaign in 2001 demonstrated a difference in light scattering between upper and lower branches of the hysteresis loop of 30% for polluted aerosols and 50% for marine aerosols at RH ~ 60% [*Carrico et al.*, 2003b]. These differences, though, are much smaller at Yosemite due to the much weaker hygroscopic growth observed. For example, Figure 7.37 shows aerosol hygroscopic growth for DOY 214 on both the deliquescent (increasing RH) and crystallization (decreasing RH) branches of the hysteresis loop. With increasing RH, the aerosol commences slight growth at RH ~ 40%. Above RH ~ 75%, stronger water uptake commences and continues with further increases in RH. Beginning from a hydrated state, the aerosol response to decreasing RH is depicted by the squares in Figure 7.37. The response shows a different pathway where this hysteresis effect is likely due to the formation of supersaturated droplets that retain a larger amount of water than is observed when increasing RH starting from a "dry" state. Generally, the haziest periods featured the weakest hygroscopic growth while the cleanest periods showed the strongest hygroscopicity (Figure 7.38). The fraction of POM in the aerosol was the key element in determining the hygroscopic growth properties as hygroscopic growth diminished with increasing POM (Figure 7.38, Figure 7.39).

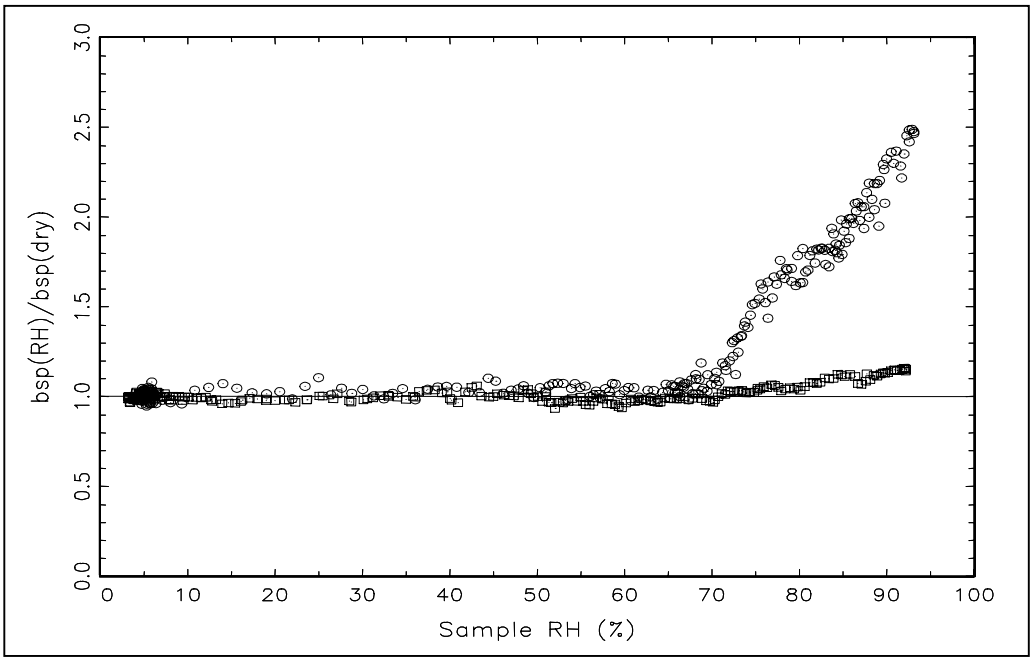

Figure 7.36 Hygroscopic growth in light scattering coefficient as a function of RH (f(RH)) showing the minimum and maximum hygroscopicity cases during YACS.

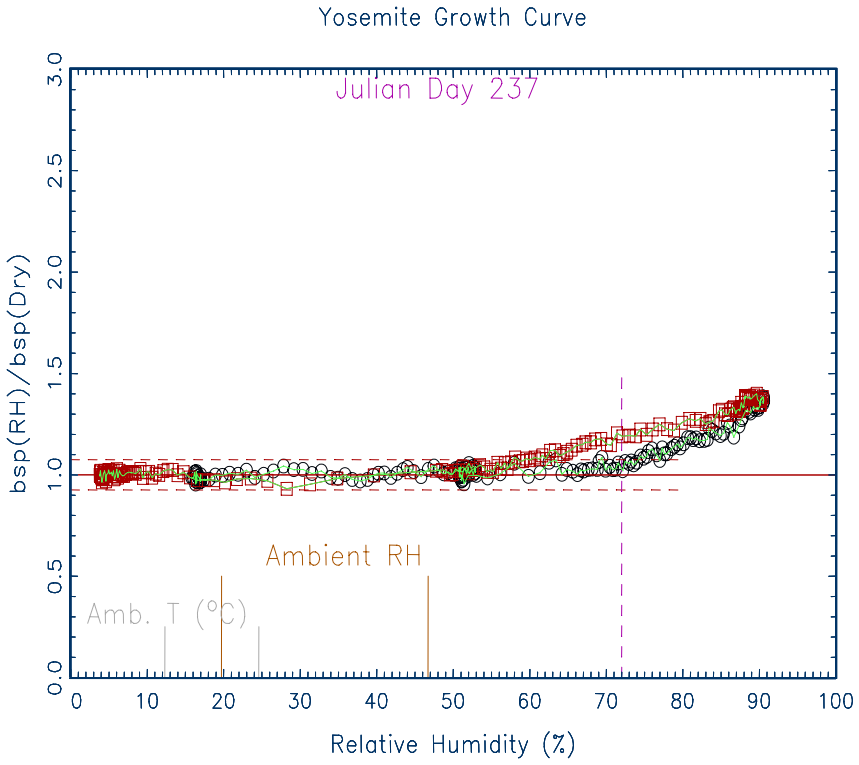

Figure 7.37 Hygroscopic growth in light scattering coefficient as a function of RH (f(RH)) on two branches of the hysteresis loop during YACS. Lower deliquescent branch is starting from a "dry" aerosol while upper metastable branch is starting from a hydrated aerosol.

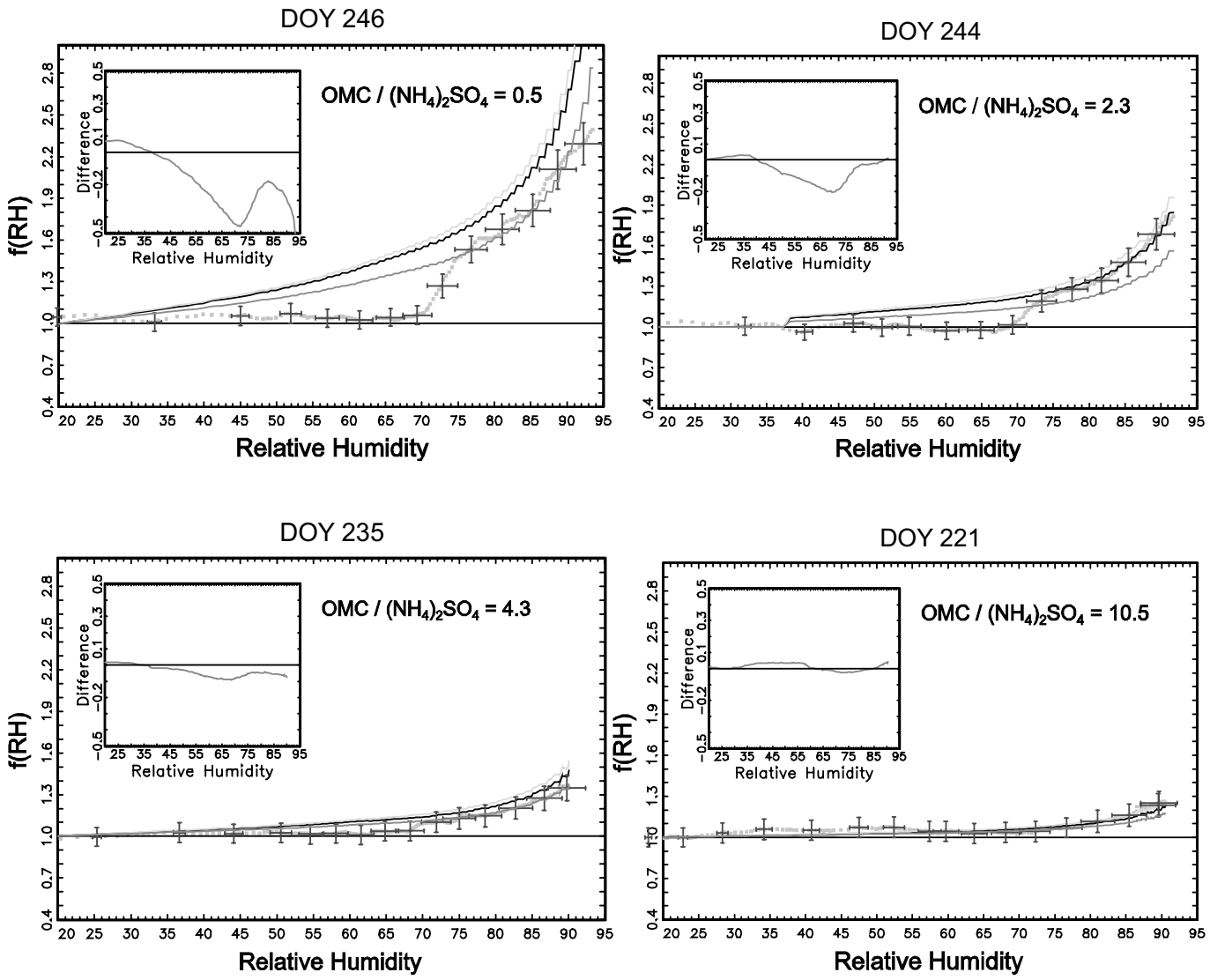

Figure 7.38 Four cases of measured f(RH) in comparison to modeled results that are given as lower and upper bounds. Also shown is the difference between measured and modeled f(RH) in the inset plot. The average particulate organic material to ammonium sulfate ratio ($OMC/(NH_4)_2SO_4$) is also given for each sampling period.

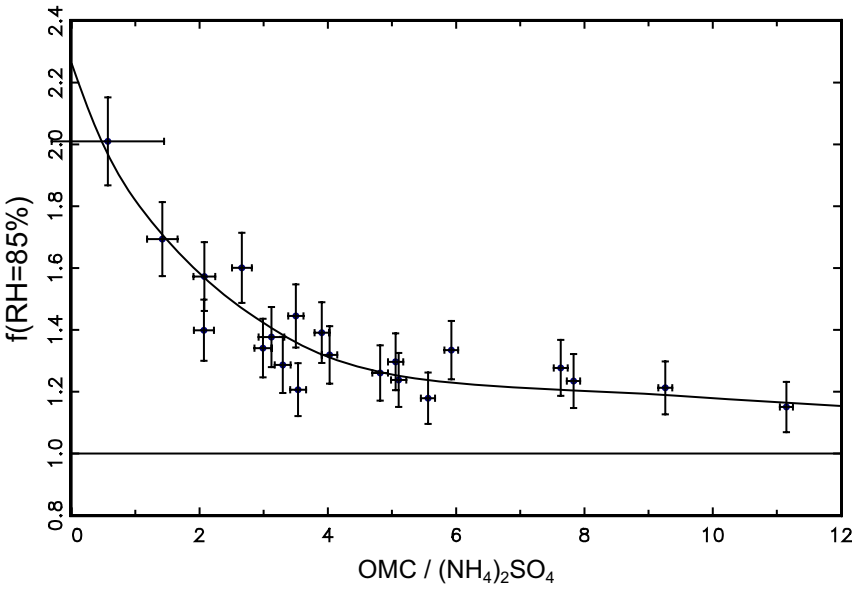

Figure 7.39 Plot of f(80 < RH < 95) as a function of OMC/$(NH_4)_2SO_4$. As the fraction of organic mass concentrations increases, the hygroscopicity of the aerosol decreases.

Results of water uptake measurements from light scattering and particle diameter instruments contribute to addressing important gaps in the knowledge of aerosol hygroscopic properties. This information is particularly valuable, as in the case of YACS, for an aerosol dominated by POM and strongly smoke impacted, as this is often observed in western U.S. national parks. Taken as a whole, the results show that aerosol phase water is a much smaller contributor to atmospheric extinction in POM-dominated, smoke-impacted, and low humidity environments, such as western U.S. parks. Taken together, the results from light scattering and diameter growth factors show a POM-dominated aerosol exhibits a modest enhancement in light scattering of 1.1 to 1.3 at an RH of 85%. Such results have important ramifications to visibility impacts in national parks and radiative forcing of climate.

7.3.3 Single Particle Morphological and Chemical Characteristics

Single particle analyses were performed on aerosol samples collected during YACS using computer-controlled scanning electron microscopy with energy-dispersed detection of x-rays (CCSEM/EDX) [*Laskin and Cowin*, 2001; *Laskin et al.*, 2003; *Hand et al.*, 2005]. The method allows the microphysical characteristics of individual particles to be examined including morphology and chemical composition. Individual particle mixing characteristics suggest four major types of particles, including volatile particles, tar balls, nonvolatile particles, and soot (Figure 7.40). Volatile particles are lost under the vacuum conditions in the microscope or upon

impaction. They leave a film that may or may not surround a nonvolatile inclusion. Tar balls are spheres or agglomerates of spheres that are not beam sensitive and do not volatilize under vacuum. One study speculates that tar balls are amorphous carbon balls, distinct from soot, and belong to an intermediate stage in the aging of organic particles from biomass burning [*Posfai et al.*, 2004]. They are composed of high molecular weight organic polymer type species that are water-insoluble and may absorb light in the visible spectrum [*Posfai et al.*, 2004]. During YACS, tar balls were observed to predominate during episodes of low visibility, which occurred during the smoke/haze events in mid-August around DOY 230 (Figure 7.41) [*Hand et al.*, 2005]. A significant correlation between occurrence of tar balls and high UV light absorption (measured at $\lambda = 370$) suggests that tar balls absorb light in the near UV and possibly visible light as well. This is important to visibility and climate as POM from biomass burning typically is not assumed to absorb solar radiation. Nonvolatile particles do not volatilize under vacuum, are not beam sensitive, and are visually distinct from tar balls. Soot-type particles are chain aggregates of graphitic carbon and are visually different than tar balls. Of the ~ 11,000 particles visually inspected from the SEM images, 47% are volatile types, 30% tar balls, 23% nonvolatile, and 0.3% soot particles.

Analysis of energy dispersive x-ray (EDX) spectra from individual particles allows determination of semi-quantitative particle composition as atomic percent above a minimum detection limit of 0.5%. High atomic percents of carbon in most of the particles suggest that carbon was the dominant species, consistent with the bulk composition data discussed previously. In fact, carbon plus oxygen accounts for > 95% of the atomic percents of the composition for 68% of the ~48,000 particles analyzed with EDX. Carbon atomic percents were less than 70% in only 0.7% of particles. Sulfur was present in 43% of the particles, K was present in 5% of the particles, Si was present in 21%, Na was present in 3%, and Cl was present in 0.7% of particles. Sulfur tended to mix with Si (11% of all particles had S-Si) rather than with potassium (2% had S-K). The particles were predominantly in the fine particle mode, with 92% of the particles having area-equivalent diameters < 0.7 μm. Tar balls tend to be dominated by carbon but are internally mixed with varying amounts of inorganic elements such as S, K, Si, Na, and Cl, while internally-mixed volatile particles (presumably, organic carbon) have higher contributions from elements other than carbon. At any given time, the particle population was an external mixture of these four carbon

particle “types”; however, there were typically internal mixtures consisting of carbon and various elemental contributions.

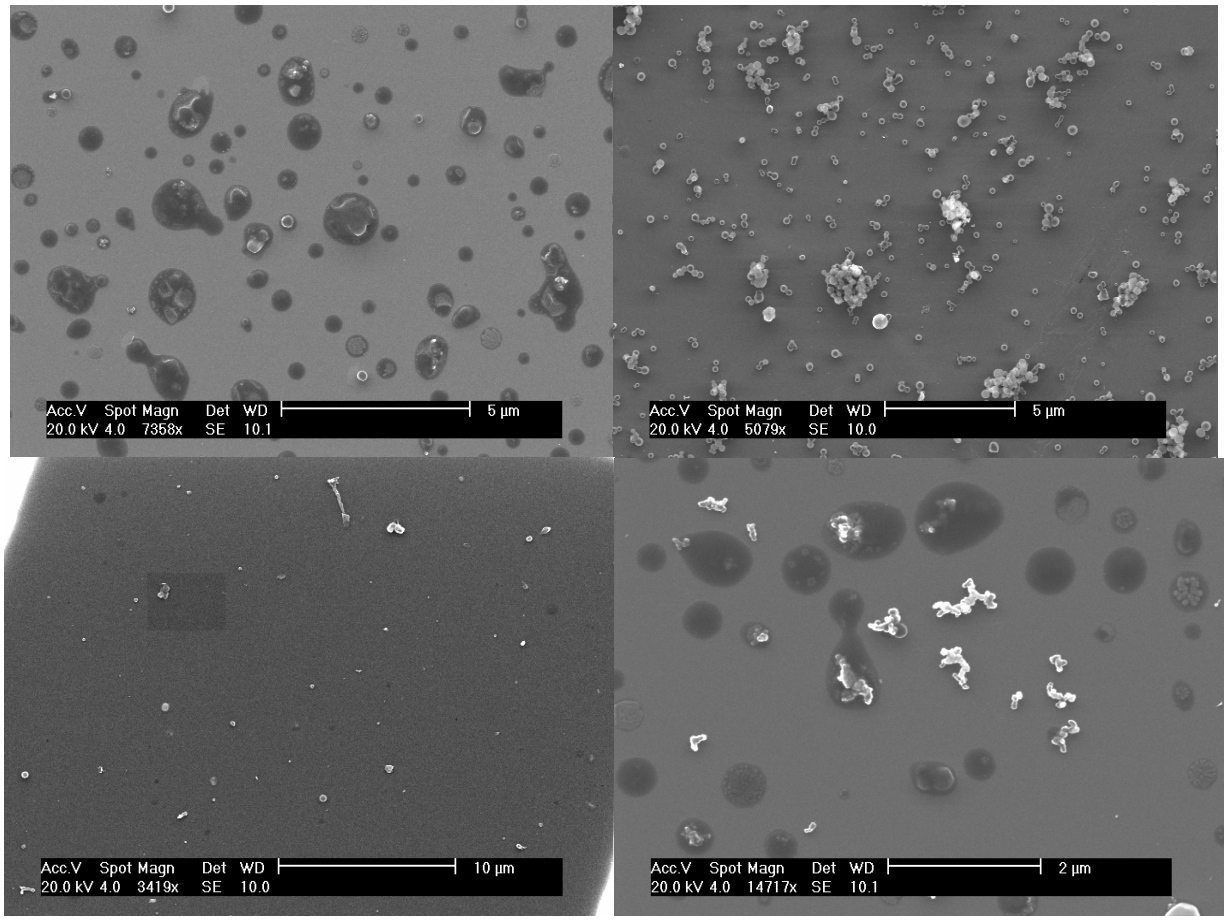

Figure 7.40 Examples of four major categories of particles observed during YACS including volatile particles (DOY 228.729), tar balls (DOY 229.853), nonvolatile particles (DOY 246.047), and soot particles, in this case, aggregated with tar balls (DOY 228.729).

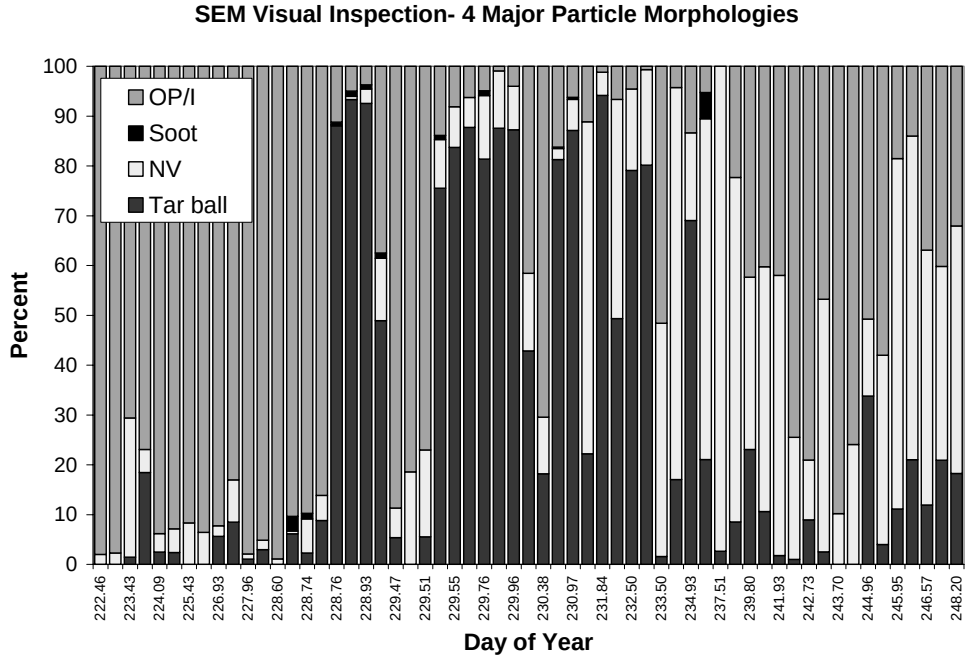

Figure 7.41 Percentage contributions of four primary particle morphologies.

Principal component analysis was used to investigate the relationships between particle morphology and bulk composition (PILS ions, normalized R&P carbon) and optical data (nephelometer and aethalometer) [*Hand et al.*, 2005]. Particle morphology was included as frequency of occurrence of a particle type for a given sample. These data were loaded onto principal components based on the calculation of eigenvectors of the correlation coefficient matrix of the centered and scaled data. Three principal components that accounted for a majority of the variation (76%) in the data matrix were subjected to varimax rotation. Temporal trends were investigated by using the principal component scores from the rotated eigenvectors. The highest loadings for factor 1 (38% of the variance) were associated with aerosols influenced by smoke. They include tar balls, b_{sp}, black carbon concentration from UV (UVBC) and near IR channels (IRBC), potassium, and OC. These relationships were not surprising given that the frequency of tar balls was significantly correlated at the 95% confidence level with b_{sp} ($r = 0.69$), OC ($r = 0.57$), potassium ($r = 0.62$), UVBC ($r = 0.67$), and IRBC ($r = 0.69$). Tar balls were also correlated with mass scattering efficiencies ($r = 0.46$); in fact, high values (~ 6 m^2 g^{-1}) were observed when tar balls accounted for > 80% of particles. These correlations link the presence of tar balls with biomass smoke and visibility impacts during YACS. Based on the SEM analysis, soot was not significantly present during the study, especially on days affected by smoke, suggesting that soot was not responsible for the majority of particle light absorption. Variables loaded onto factor 2

(27% of the variance) were associated with inorganic species such as Na, NH_4^+, Mg, Ca, NO_3^-, and SO_4^{2-}, though no particle morphology type was associated. Scores for this factor were highest during the latter part of the study (27 August to 1 September) when POM decreased after the major smoke episode. The third factor (11% of the variance) was associated with volatile type particles.

7.3.4 Isotopic Analysis of Carbonaceous $PM_{2.5}$

Measurements collected at Turtleback Dome (0800–2000 local time) using $PM_{2.5}$ high-volume filter samplers were analyzed using carbon isotopic analysis at Lawrence Livermore National Lab. A two-component model examining proportions of $^{12}C/^{14}C$ allows delineation of fossil carbon from contemporary carbon [*Bench and Herckes*, 2004]. Use of the two-component model yields a first-order answer to derive fossil and contemporary biogenic carbon contents and assumes that contributions from nonfossil and noncontemporary sources of carbon during the sampling periods were negligible. Fossil carbon is analogous to anthropogenic carbon from fossil fuel sources, while contemporary carbon is attributed to biogenic sources including fires.

Isotopic analysis indicated that >90% of the fine POM was derived from contemporary sources rather than fossil fuel combustion. Total carbon (TC) concentrations at Turtleback Dome were directly proportional to contemporary carbon with a slope of 0.9997, $R^2 = 0.98$, and an intercept of -0.7 (Figure 7.42). Fossil carbon was nearly constant at 0.7 ± 0.1 μg/m^3 and largely independent of the total carbon content. Thus the variability of TC was driven by the variable contemporary carbon contribution added to the "background signal" of a small fossil carbon contribution. Furthermore, periods of impaired visibility during YACS were largely a result of increased contemporary carbon contributions. The analysis cannot, however, distinguish between smoke and other sources of contemporary carbon. It should be noted that the samples were collected during daytime, upslope flow conditions and exclude nighttime, downslope influences.

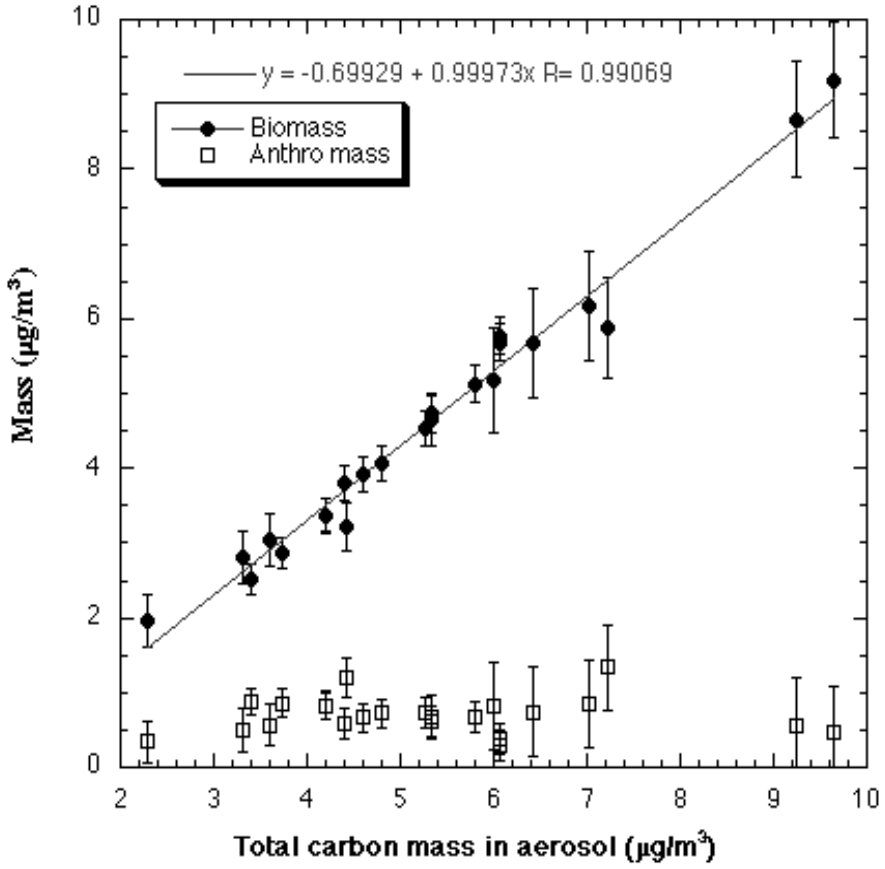

Figure 7.42 Fossil and contemporary carbon contributions to OC at Yosemite during YACS.

7.3.5 Speciation of Particulate Organic Carbon: Markers for Biogenic, Pyrogenic, and Anthropogenic Source Categories

Speciated composition of POM for weekly composite and 12–24 hour samples were obtained from $PM_{2.5}$, PM_{10}, and six-stage cascade-impactor, high-volume collectors. Speciation of the organic aerosol fraction was accomplished by solvent extraction, followed by quantification using gas chromatography with mass spectrometric detection (GC-MS) [*Brown et al.*, 2002; *Engling et al.*, 2005]. A large spectrum of POM constituents was quantified, including n-alkanes, alkanols, carbonyls, carboxylic acids, PAHs, and a variety of molecular tracer compounds. Based on source profiles from literature, ratios of marker to POM concentrations were used to estimate the relative contributions of wood smoke and anthropogenic sources.

POM speciation was consistent with carbon isotopic analysis discussed previously in that it showed strong markers for biogenic compounds, both wood smoke and biogenic secondary organic aerosol compounds. High values (3 to 6) of the "carbon preference index" (CPI) were

observed where values greater than 2 indicate dominance of biogenic/pyrogenic sources [*Brown et al.*, 2002; *Engling et al.*, 2005]. Lower CPI values were observed at Yosemite Valley, showing the greater contribution of anthropogenic sources there relative to Turtleback Dome. Overall, tracers for anthropogenic markers, such as hopanes and steranes, showed low concentrations and indicated <10% contribution to $PM_{2.5}$ from vehicular sources on average.

Based on POM speciation, the second half of the study featured higher concentrations of wood smoke markers including resin acids, anhydrosugars including levoglucosan, and methoxyphenols (Figure 7.43). All wood smoke tracers show a diurnal trend in the form of higher concentrations during the night compared to daytime. In contrast, total POM concentrations typically peaked in the late afternoon, which may be related to higher photochemical activity and greater formation of secondary biogenic aerosol components. Secondary biogenic compounds constituted an important POM source, as indicated by relatively high concentrations of pinene oxidation products such as pinonaldehyde and pinic and pinonic acid (Figure 7.44). The period with the highest overall POM concentration (Week 5, 10–16 August 2002) also featured high concentrations of markers for both smoke and secondary organic aerosol (SOA) (Figure 7.43, Figure 7.44). Levoglucosan was measured with peak concentrations of 180 ng/m^3 during the second intensive haze episode in mid-August. Weekly composite samples during this period showed wood smoke contributions as high as 65%. The high concentration of biogenic SOA compounds, coinciding with high concentrations of wood smoke tracers, may be related to higher emission rates of biogenic VOCs due to elevated temperatures during a wildfire. The persistence of high wood smoke markers into the latter part of the study may be related to some short duration overnight local smoke events in the last couple weeks of the study.

Investigation of particle size distributions of tracer compounds showed that some compounds, such as n-alkanes and n-alkanoic acids, were present in particles of a wider size range extending to super-micrometer particles. Other species, including hopanes, dicarboxylic acids, and selected pinene oxidation products, were detected only for $D_p < 1$ μm particles (Figure 7.45). Overall, organic speciation during YACS indicated that POM was dominated by natural sources, in particular by smoke from wildfires and secondary organics.

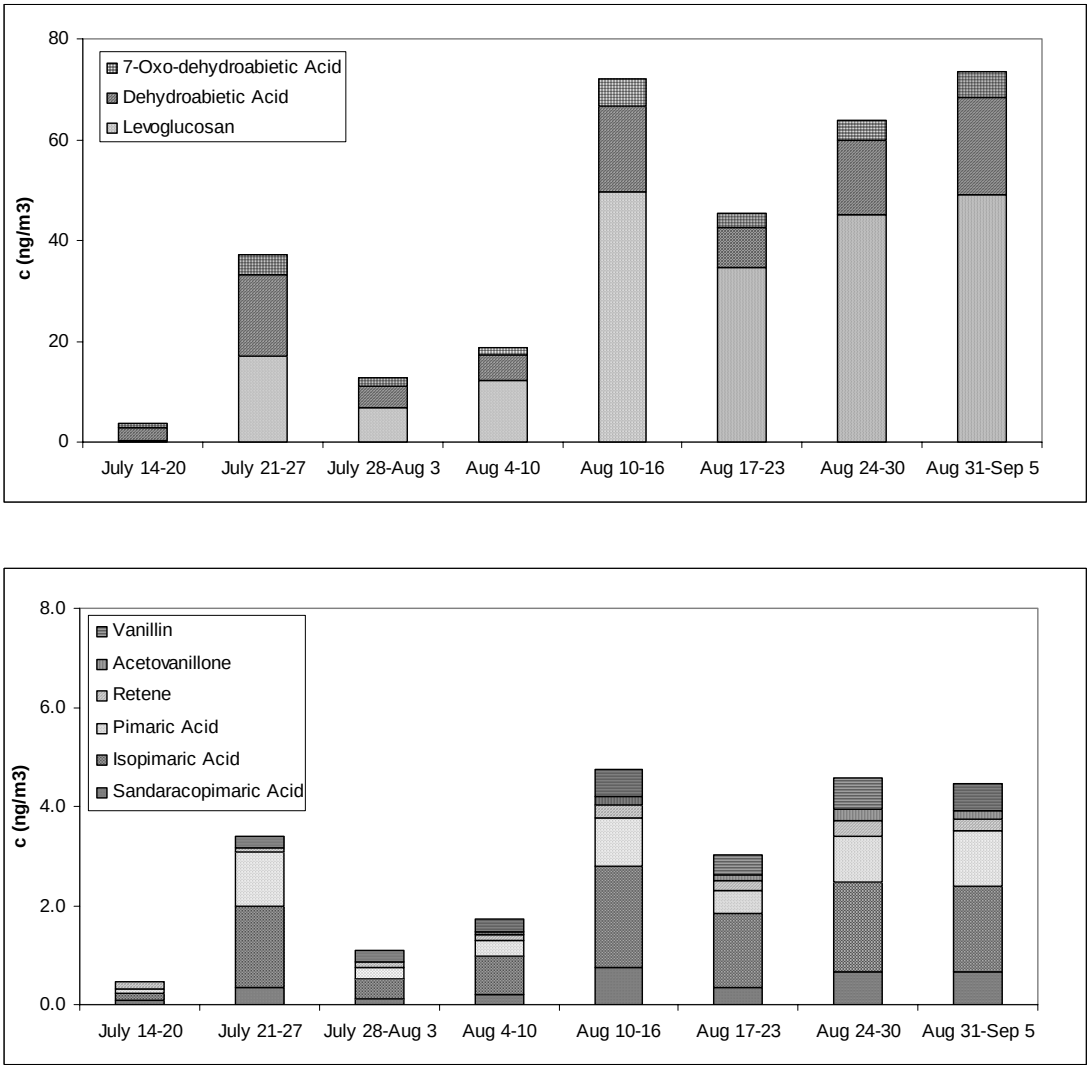

Figure 7.43 Timeline of wood smoke marker concentrations.

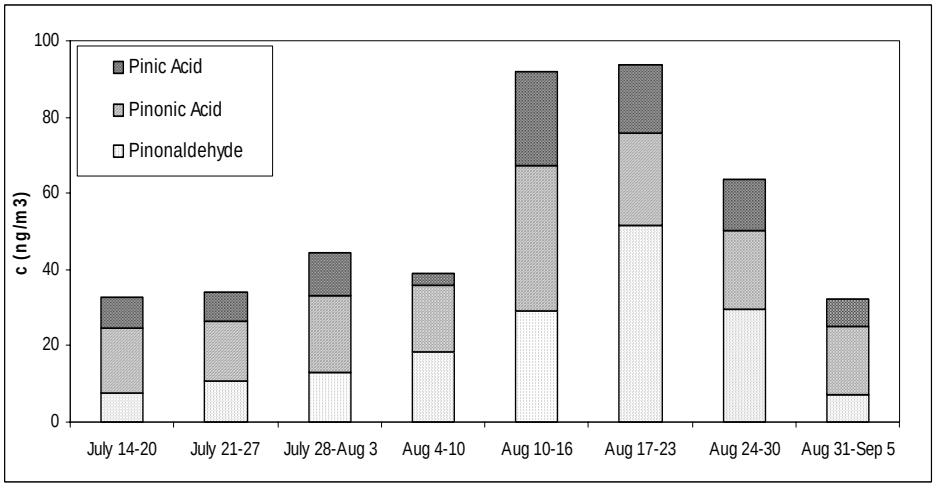

Figure 7.44 Timeline of biogenic secondary organic aerosol species concentrations.

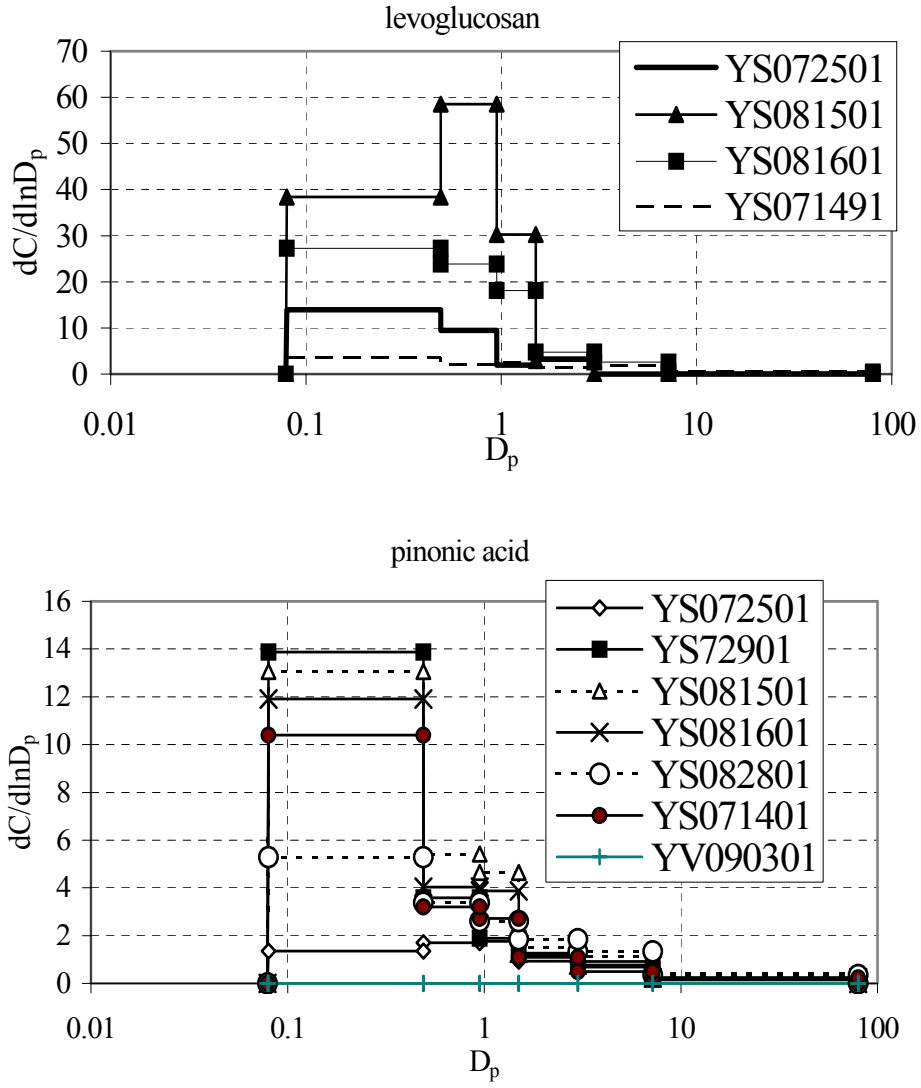

Figure 7.45 Size distributions from several dates of molecular marker compounds from multistage, hi-vol impactor samples including levoglucosan (woodsmoke tracer) and pinonic acid (biogenic SOA tracer).

7.4 Exploring Probable Aerosol Sources during YACS

7.4.1 Fires and California Air Quality during YACS

The analyses described above all suggest a predominantly biogenic/pyrogenic aerosol source and, in particular, a strong contribution from biomass smoke. Examination of the fire record and airmass transport evidence in relation to the measured aerosol properties further illuminates the source of the widespread haze at Yosemite during YACS. Overall, the United States experienced an active fire season during 2002, with about 7 million acres burned in about 88,000 fires (http://www.nifc.gov/fireinfo/2002/summary.html) (Figure 7.46,Table 7.9). The severe fire

season resulted from extreme drought conditions throughout most of the United States, with nearly half the country reporting moderate to extreme drought conditions early in the season.

Numerous and massive fires in West Coast states (Figure 7.47) contributed to the regional haze that engulfed California's San Joaquin valley. By September of 2002, California experienced 248% and the Pacific Northwest 372% of their average yearly acreage burned. The combined acreage burned in California and Oregon was approximately 1.5 million acres with the Biscuit fire in southwest Oregon (~ 500,000 acres, Figure 7.48) and the McNalley fire in Sequoia/Kings Canyon National Park (150,000 acres) as the largest contributors. The Biscuit fire in Oregon was the largest reported in the last century in Oregon (Figure 7.48) (National Interagency Fire Center). The Biscuit and McNalley fires were located approximately 700 km north northwest and 150 km south of Yosemite, respectively. Satellite imagery (MODIS; http://:visibleearth.nasa.gov) suggests smoke from both of these fires likely impacted air quality in the San Joaquin valley and Yosemite (Figure 7.49). Due in part to this heavy fire activity, the summer of 2002 featured poor air quality throughout the central valley of California and at Yosemite. Schools were advised to cancel outdoor activities on 14 days and the 11 "hazardous air days" represented the highest number of severely polluted days since 1998 (http://www.arb.ca.gov/homepage.htm). Additionally, several fires in Yosemite National Park, though relatively small, potentially influenced sampling during YACS due to their proximity (Figure 7.47).

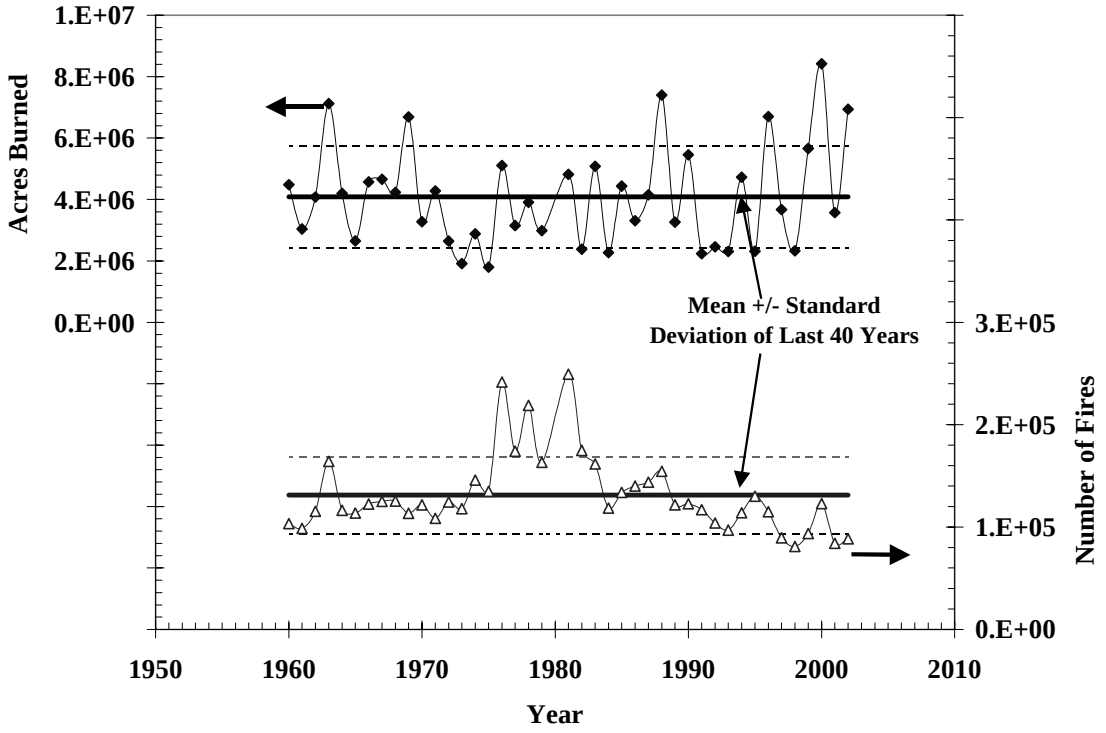

Figure 7.46 U.S. history of wildfire number and acres burned (data from NIFC). 2002 featured a large number of acres burned with relatively fewer fires as compared with historical averages.

Table 7.9 Summary of 2002 wildfire statistics (Source: National Interagency Fire Center).

Parameter	Quantity
Number of Fires (2002 final)	88,458
10-year Average (1992–2001)	103,112
Acres Burned (2002 final)	6,937,584
10-year Average (1992–2001)	4,215,089
Structures Burned	2,381
Estimated Cost of Fire Suppression (federal)	$1.6 billion

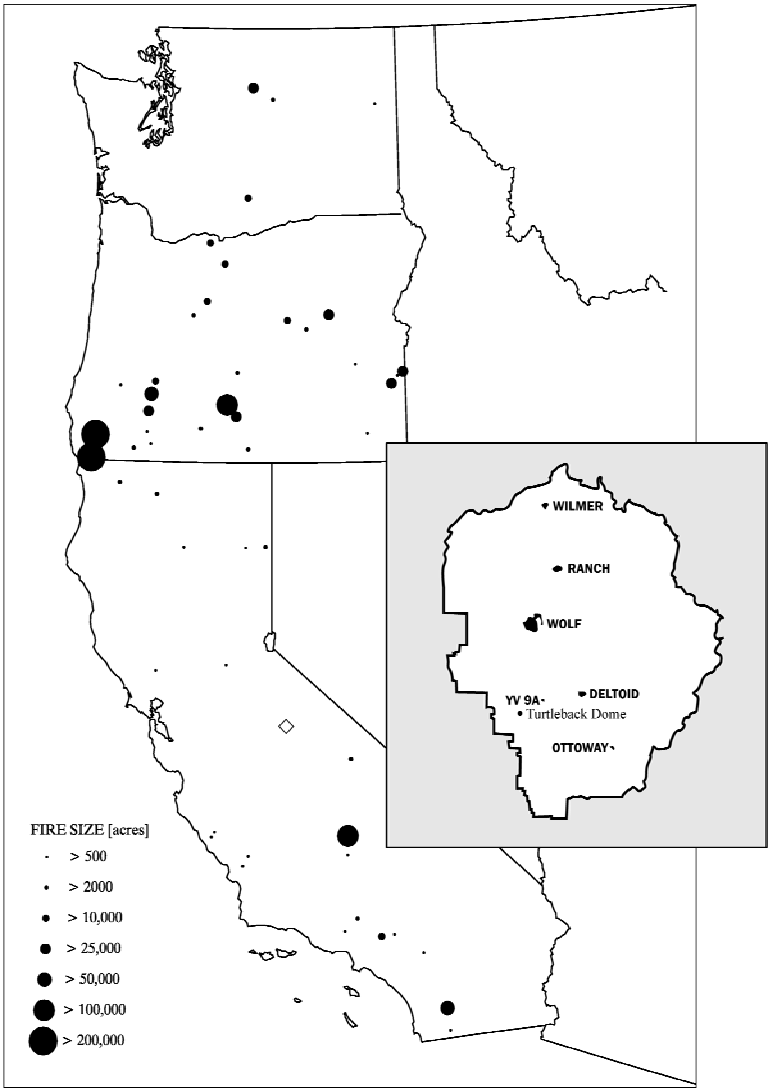

Figure 7.47 Fires in California, Oregon, and Washington during YACS in summer 2002.

Figure 7.48 Images from the Biscuit fire of 2002 in southwest Oregon that burned ~ 500,000 acres (NIFC; 15 August 2002; photos by Karen Wattenmaker).

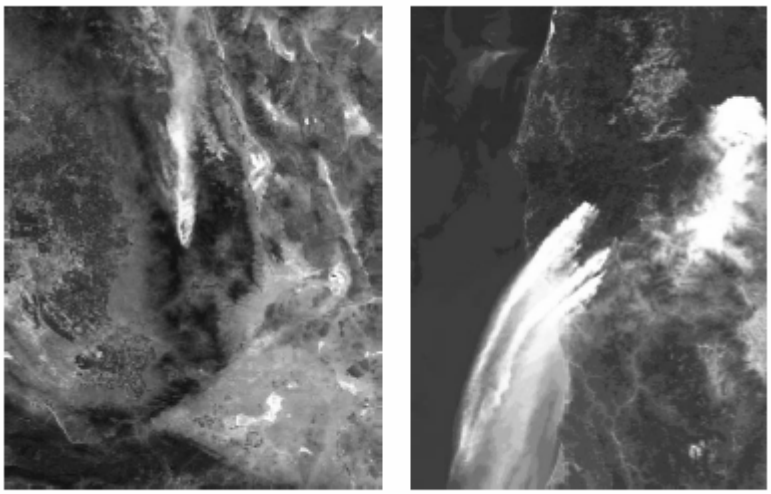

Figure 7.49 MODIS satellite photos of smoke plumes from the Biscuit and McNalley fires during YACS.

7.4.2 Transport Patterns during YACS

In order to examine the source regions of the aerosols arriving at Yosemite, airmass back trajectories and residence times were calculated for the entire study period (20 July through 5 September 2002). An example airmass back trajectory calculated using the National Oceanic and Atmospheric Administration (NOAA) Hybrid Single-Particle Lagrangian Integrated Trajectory (HYSPLIT) model [*Draxler et al.*, 1994] at several heights from an individual day (13 August 2002, during the strongest haze episode) indicates airmasses passing over Oregon and northern California before arrival at Yosemite (Figure 7.50). The locations of wildfires that grew larger than 500 acres during the study are also plotted for California, Oregon, and Washington. Examination of backward trajectories for other times revealed two main paths for transport during the study. The first path originated off the coast of British Columbia, ran south over the coasts of Washington, Oregon, and northern California, before heading east over the San Francisco Bay area and the San Joaquin valley to the site. The other traveled through central Oregon and northwestern Nevada before reaching the park from the east. Additional modeled transport pathways originated from the south of Yosemite and to the west, though this occurred infrequently. Overall, most transport pathways traveled over Oregon or very close to the Oregon coastline before reaching Yosemite.

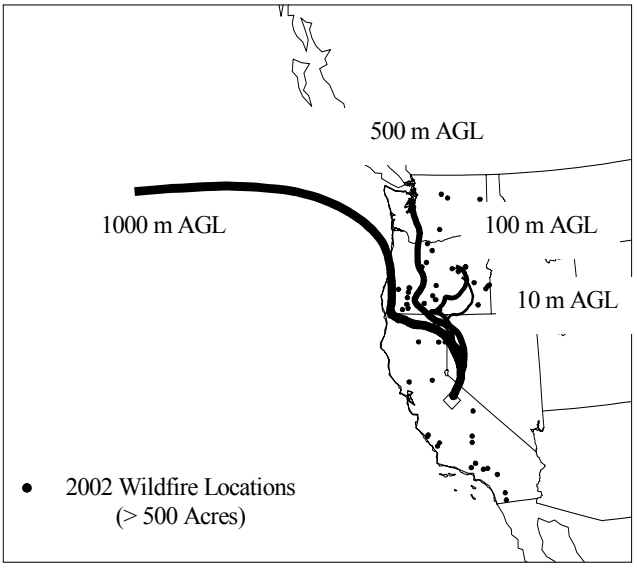

Figure 7.50 Plots of back trajectories modeled using HYSPLIT for 1200 local time on 13 August 2002 for four different heights above ground level. Locations of fires that reached a size greater than 500 acres are shown as circles and the hollow diamond indicates Turtleback Dome.

Residence time analysis can be used to produce maps that show the transport pathways where air parcels are most likely to have resided before reaching the receptor [*Gebhart et al.*, 2001]. For the entire study, residence times were determined for 0.5 x 0.5 degree cells on a grid domain bounded by latitudes of 24 N and 74 N and the 170 W and 110 W meridians. A contour map of normalized residence times for the YACS study period indicates source regions where lighter colors in northern California and western Oregon indicate longer contact time with the indicated region (Figure 7.51). The majority of backward trajectories modeled during the study originated to the northwest of the study site and underscore the impact of the Biscuit and other fires in Oregon and northern California [*McMeeking*, 2004].

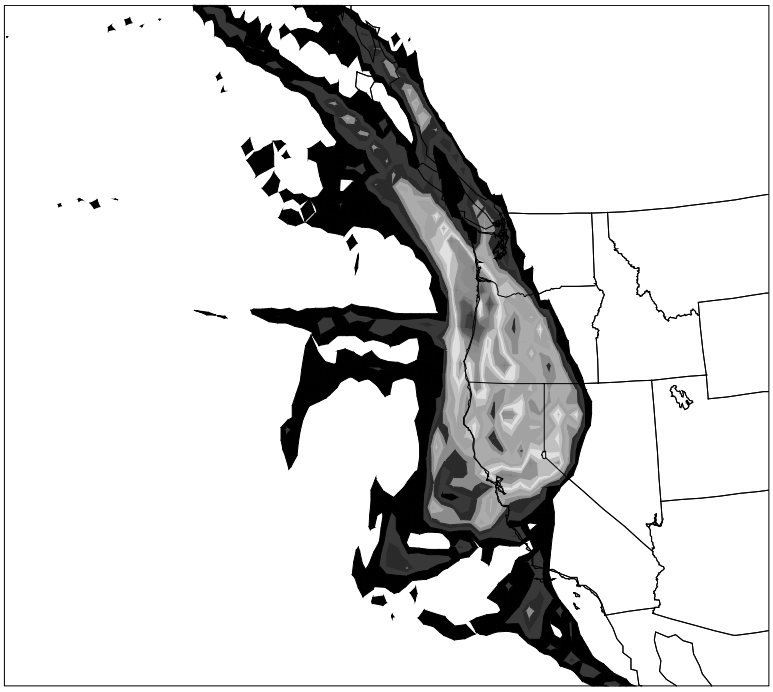

Figure 7.51 Contour plot of normalized residence times for all trajectories arriving at Turtleback Dome for the period 20 July 2002 through 5 September 2002. Lighter colors in northern California and western Oregon indicate higher probability of air parcels traveling through that region before reaching the site.

7.4.3 Smoke Influences on Aerosol Properties

A timeline of the daily average POM, soluble potassium, and difference in the UV and IR channels of the aethalometer shows that these parameters track each other quite closely (Figure 7.52). The difference in UV (350 nm) and near IR (880 nm) light absorption as measured with a dual-wavelength aethalometer (UV-IR, expressed in terms of the BC measurement unit of μgm^{-3}) is a qualitative indicator for biomass smoke. This is thought to be due to the enhanced UV

absorption associated with POM components such as aromatic compounds that are found in wood smoke (www.mageesci.com). Biomass burning also releases a large amount of potassium-rich submicrometer particles, and thus the presence of nonseasalt soluble K^+ is also a smoke marker [*Ma et al.*, 2003]. From these markers, the large peak in POM during mid-August also featured a strong contribution from biomass smoke. Other, shorter-duration episodes also appeared to have been considerably impacted by smoke, possibly from local fires. In addition to the primary smoke contributions, a substantial secondary organic aerosol component was observed [*Engling et al.*, 2005]. Comparison of POM during summer 2002 and historically shows it to be an above average year but not atypical of Yosemite conditions (Figure 7.53, Table 7.10). A scatter plot of OC versus soluble potassium further illustrates the controlling influence of smoke on POM concentrations during YACS and suggests it is somewhat stronger than historical associations (Figure 7.54).

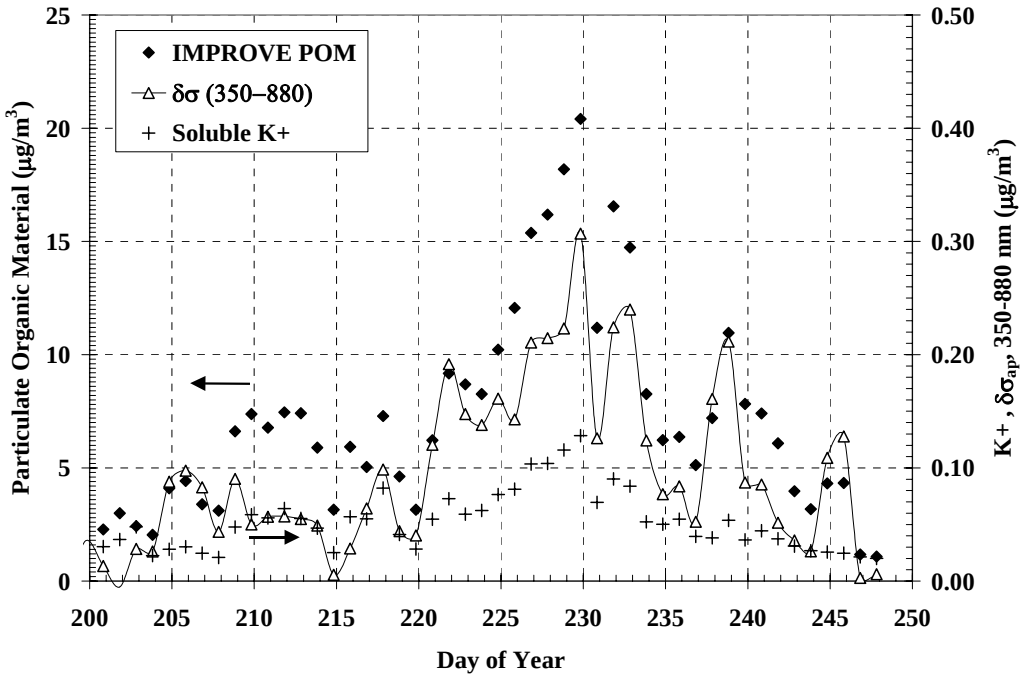

Figure 7.52 Time series of POM (assuming 1.8*OC) from IMPROVE measurements, difference in aethalometer BC concentrations, and soluble potassium at Yosemite during YACS.

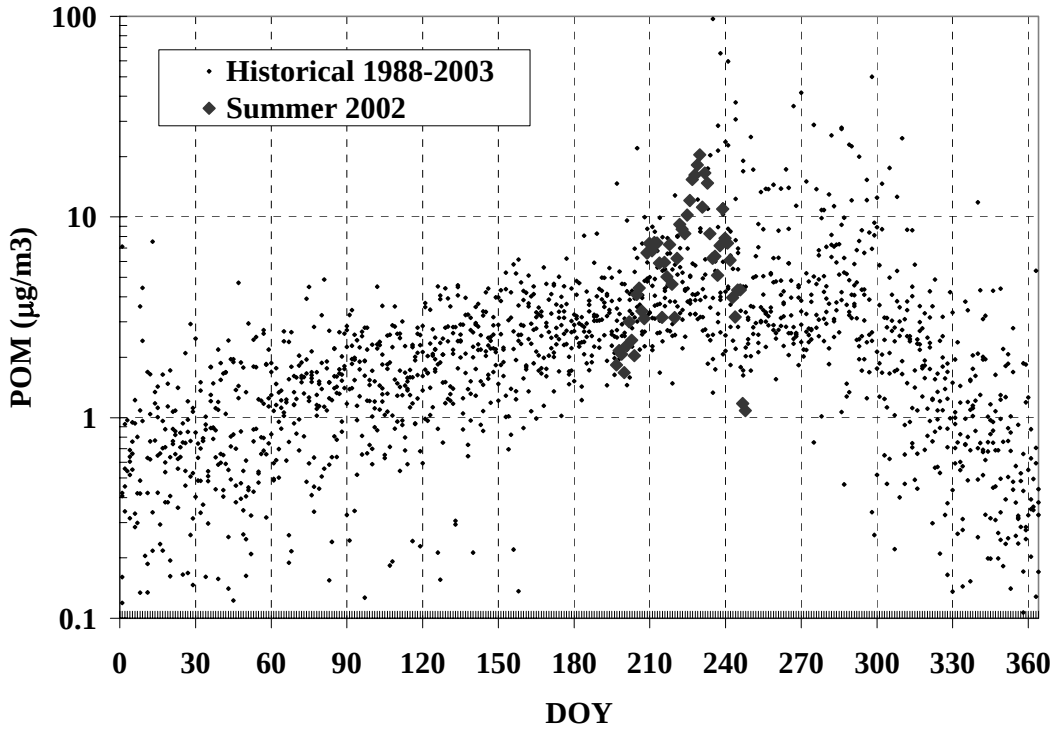

Figure 7.53 Comparison of POM (assuming 1.8*OC) from IMPROVE measurements during YACS and historically at Yosemite.

Table 7.10 Comparison of summer 2002 versus IMPROVE historical data summer 1988–2003.

	YOSE Summer 2002			YOSE Historical (1988–2003)		
	Mean	**Std Dev**	**n**	**Mean**	**Std Dev**	**n**
$PM_{2.5}$	10.48	4.87	52	8.37	4.91	1560
POM	6.81	4.59	52	6.41*	9.53*	1709
EC	0.38	0.22	52	0.52	0.72	1559
SO_4^{2-}	1.16	0.30	52	1.22	0.46	1565
NO_3^-	0.35	0.17	52	0.35	0.29	1588
K	0.05	0.03	52	0.06	0.03	1589

* average POM decreases to 5.4 ± 4.8 μgm^{-3} excluding 2001 when POM reached 97 μgm^{-3} with local fire impact

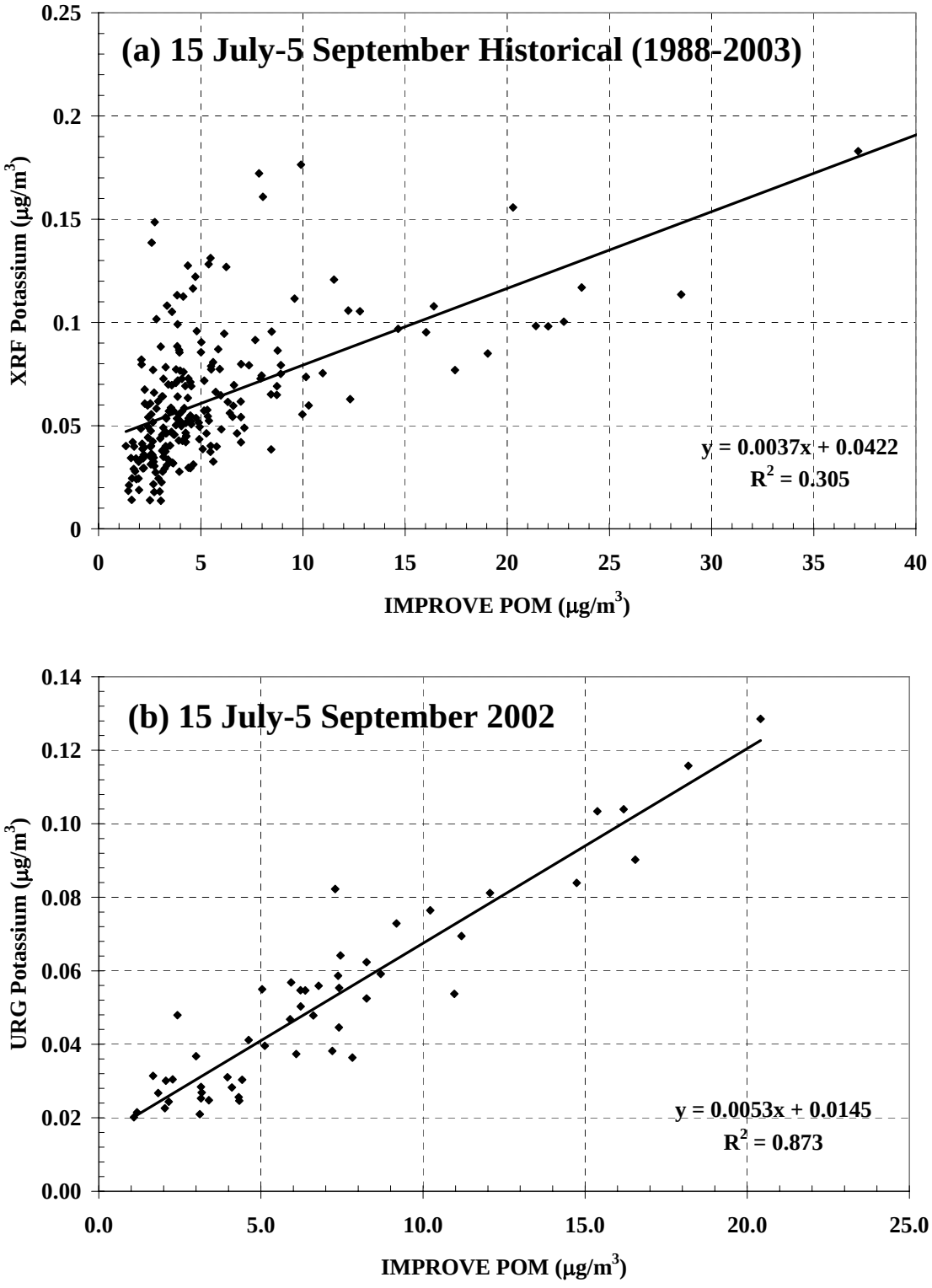

Figure 7.54 Scatter plot of organic carbon (OC) versus soluble potassium from IMPROVE filters historically and during YACS.

An estimate of the source contributions to fine POM can be arrived at using source attributions based on molecular markers [*Engling et al.*, 2005] and radiocarbon measurements [*Bench and Herckes*, 2004]. Using radiocarbon measurements (daytime only) and the 1.8 POM/OC multiplier found herein, the fossil POM varied about ~1 μgm^{-3} during YACS and was largely independent of total POM. As a percentage, the fossil carbon component of POM on a 24-hour basis varied from <5% (during the highest POM periods) to a maximum of 20% (during the lowest POM concentration periods), with an average contribution of ~ 10% (Table 7.11). Consistent with the radiocarbon measurements, molecular markers for meat cooking and vehicular sources combined to give a maximum of 10% contribution based on weekly speciated samples [*Engling et al.*, 2005].

As described in section 5.2, the remaining, dominant "modern" carbon may be classified as from pyrogenic (biomass burning) or biogenic (from biological activities excluding fire) sources. The association between these two categories observed during YACS complicates this delineation [*Engling et al.*, 2005]. This association relates to the high POM/OC ratio of 1.8 observed during YACS, indicating a relatively aged aerosol. Fresh POM aerosols have been observed to have a substantially lower POM/OC multiplier of ~ 1.2 [*Turpin and Lim*, 2001]. The increased POM/OC ratio during YACS is due to the oxidation of primary carbon emissions as well as the formation of secondary organic aerosol from condensation of precursor VOC species. During the least hazy days, multiple smoke indicators, including soluble potassium, aethalometer data (UV-IR), and wood smoke tracers such as levoglucosan, denoted a low influence of smoke, estimated here as 10%, considering both primary and any formation of secondary organic aerosol on existing smoke particles. Thus the remaining 70+% of the POM mass is likely the result of the "natural background" from biogenic sources, both primary and secondary, unassociated with biomass burning.

During the haziest period when POM reached ~ 15 μgm^{-3}, transport patterns indicated the influence of massive wildfires in Oregon [*McMeeking et al.*, 2005a]. As discussed previously, markers including the aethalometer data and soluble potassium showed the influence of biomass smoke during such periods. In addition, marker-related biogenic sources such as pinic and pinonic acid also increased by factors of 2–4 during the haziest period, underscoring the enhanced contribution of secondary organic aerosol during such periods (Figure 7.44). Thus a simultaneous increase in purely biogenic SOA concentrations as well as an increase in wood smoke concentrations occurred during hazy periods. Carbon speciation showed roughly a 20%

contribution by primary smoke during the hazy periods. This is likely a lower bound of the primary pyrogenic contribution as the stability of these markers in aged smoke may limit their lifetime. The remaining 75% of POM is secondary species and modern carbon, biogenic or pyrogenic in source. Conceivably, the biogenic concentration unrelated to smoke increased by a factor of 2 to 4 from "clean" conditions, resulting in approximately 4 μgm^{-3} or 25% of the POM during the haziest periods. The remaining 50% of POM is thus attributed to secondary species formed on the aged, transported primary smoke emissions (Table 7.11).

As an experiment average, the fossil carbon component composed ~ 15% of the carbon during YACS from the radiocarbon analysis. The remaining 85% of the 7 μgm^{-3} of POM is from "modern" carbon sources. The average biogenic contribution portion unassociated with biomass smoke is estimated as ~ 2.5 μgm^{-3} or 35% of average POM. From the experiment-average carbon speciation, roughly 15% of POM on average is primary smoke [*Engling et al.*, 2005]. Thus approximately 40% of POM on average is secondary organic aerosol that can be attributed to smoke. It should be reiterated though, that due to the association of smoke and biogenic indicators and the inability to distinguish marker compounds for SOA related and unrelated to smoke, a clear distinction between the biogenic and pyrogenic sources is not possible. More study of the formation and evolution of POM aerosols from pyrogenic and biogenic sources is clearly needed. A summary of the estimates of estimated POM contributions is given in Table 7.11.

Table 7.11 Approximate percentage contributions to POM during YACS 2002 from anthropogenic, pyrogenic (primary and secondary contributions), and biogenic sources (secondary aerosol unrelated to biomass smoke).

	POM Concentration ($\mu g/m^3$)	**Anthropogenic Contribution**	**Pyrogenic Contribution**	**Biogenic Contribution**
"Cleanest" Days	2	20%	5–10%	70+%
"Haziest" Days	15	5%	20% primary 50% secondary	25%
Average YACS 2002	7	10%	15% primary 40% secondary	35%

7.4.4 Measurements at Neighboring IMPROVE Sites during YACS

A comparative look at other nearby IMPROVE sites during YACS demonstrates the regional nature of the haze during this period. Three parks in northern California, Lassen Volcanic

National Park, Trinity National Recreation Area, and Pinnacles National Monument, show large peaks in aerosol loading during July to August of 2002. At Lassen and Trinity, OC reaches peak values of 17–19 μgm^{-3} (equivalent to POM of 30–35 μgm^{-3} assuming POM/OC of 1.8) during the middle of August around DOY 230 (18 August 2002). Pinnacles, located farther south and more distant from the Oregon fires, shows peak OC values of ~ 8 (POM = 15 μgm^{-3}). Contour plots of OC and EC concentrations based on the IMPROVE network measurements as a function of latitude show this gradient trend in more detail (Figure 7.56, Figure 7.57). The plots are time series of EC and OC as a function of latitude (for a fixed longitude equal to that of Yosemite). A huge peak in both EC and OC is evident near the large fires in Oregon around the middle of August 2002. Also of note is the broader peak in OC concentration, as this has both primary and secondary contributions that can form downwind of the emission source. EC is a primary emission and thus exhibits highest concentrations closer to the source.

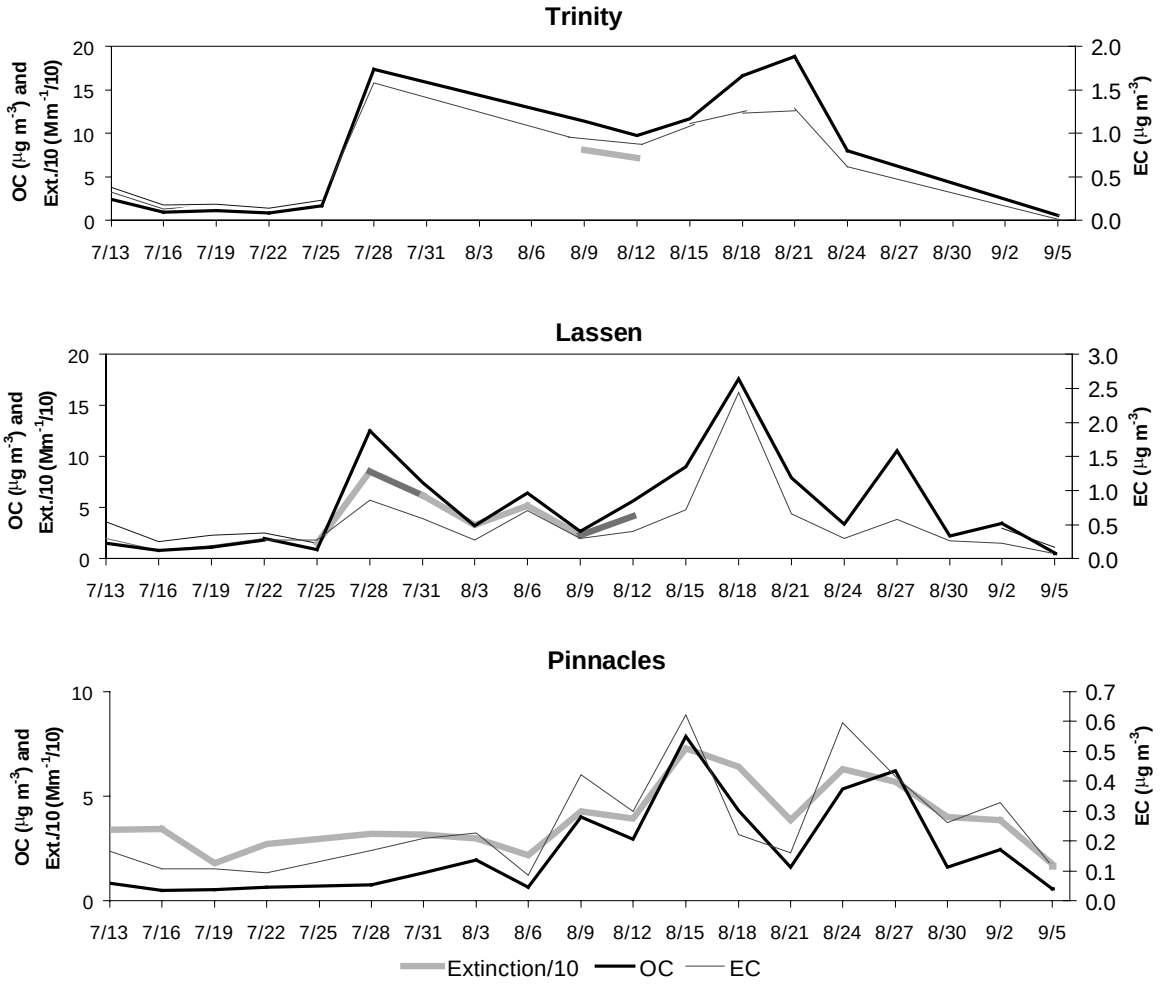

Figure 7.55 Time series of light extinction, POM, and EC at several California parks during YACS.

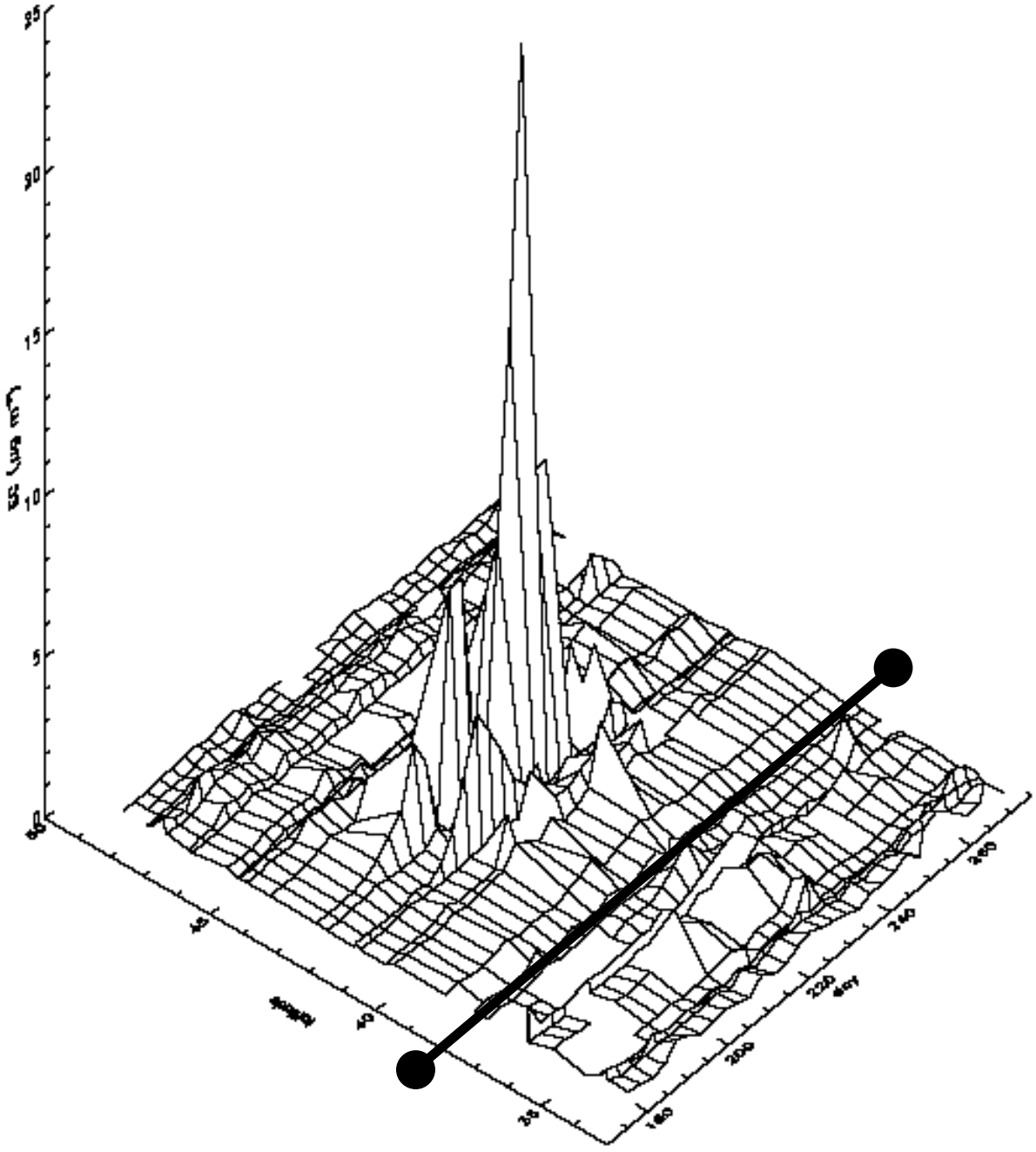

Figure 7.56 IMPROVE EC as a function of latitude and time during YACS. The solid dark line indicates the approximate latitude of Yosemite.

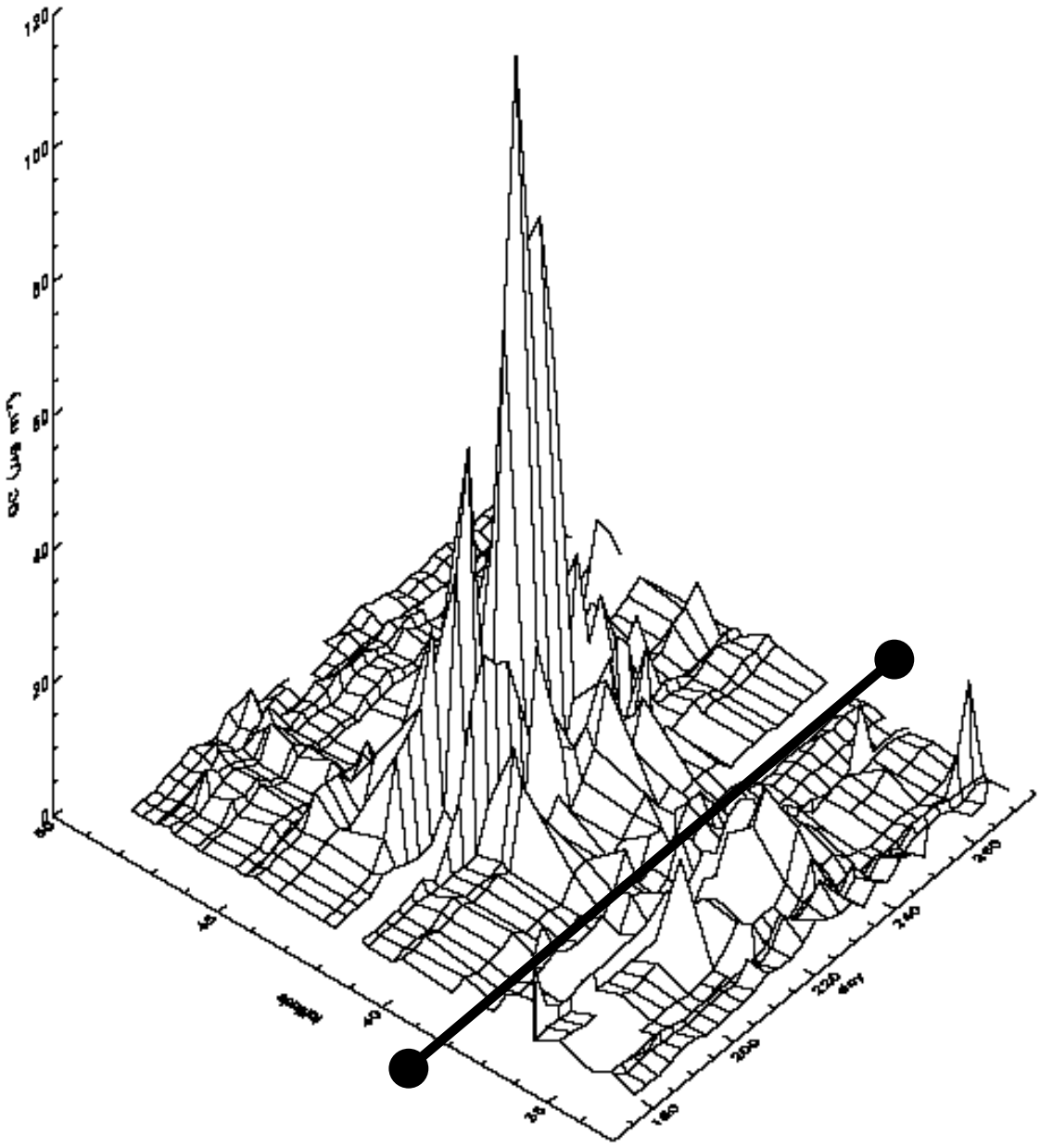

Figure 7.57 IMPROVE OC as a function of longitude and time during YACS. The solid dark line indicates the approximate latitude of Yosemite.

8. *SUMMARY AND CONCLUSIONS*

8.1 Summary of Field Campaign

A field measurement campaign was conducted in summer 2002 at Yosemite National Park to improve understanding of aerosol properties and visibility impacts at a western U.S. park. The Yosemite Aerosol Characterization Study (YACS) involved field measurements at the IMPROVE site located at Turtleback Dome in Yosemite. Historical records from IMPROVE measurements at Yosemite reveal an aerosol dominated by particulate organic material (POM) at the site, and summer 2002 was not an exception to this trend. The intensive aerosol measurements included a broad suite of detailed physical, chemical, and optical properties complementing the ongoing IMPROVE network measurements at Yosemite. These properties are all important to air quality and visibility impacts of aerosols in Class I visibility areas and have implications for the U.S. EPA's Regional Haze Rule.

Aerosol $PM_{2.5}$ and PM_{10} gravimetric mass were measured with the IMPROVE filter sampling system at Turtleback Dome and at the visitor center in Yosemite Valley. The IMPROVE filters also were analyzed for anions, elements, and elemental and organic carbon. In addition to the two sets of IMPROVE network filter samplers, aerosol chemical composition was measured by a range of time-integrated and high time resolution techniques. Among the 24-hour samplers was the URG $PM_{2.5}$ filter sampling system, yielding major cations and anions using ion chromatography. A MOUDI cascade impactor provided size distributions of inorganic species as well. A semi-continuous particle-into-liquid sampler was used to measure high time resolution (15 minute) $PM_{2.5}$ anions and cations. In addition to the IMPROVE $PM_{2.5}$ organic and elemental carbon measurement, total carbon was measured hourly with a semi-continuous thermal evolution technique (R&P 5400 particulate carbon monitor). Subtracting the black carbon concentrations measured with an aethalometer from the total carbon measurement gives organic carbon. To yield POM, organic carbon must be multiplied by a factor that accounts for associated elements such as oxygen, nitrogen, and hydrogen. This was a factor that proved to be an important parameter studied in this experiment. High-volume filter samples were collected to examine organic carbon species as well as the carbon isotopic content. Isotopic analysis provides a dichotomy of carbon into "modern" and "fossil" carbon. Carbon speciation using gas-chromatography coupled to a

mass spectrometer (GC-MS) provides markers for anthropogenic, biogenic, and pyrogenic sources.

Aerosol optical and physical properties were measured with a variety of techniques. Measurements of dry particle size distributions were made with a differential mobility analyzer (DMA) and an optical particle counter (OPC). Best fit OPC and DMA size distributions were then merged to give a complete size distribution over the diameter range of $0.038 < D_p < 2.1$ μm and a retrieved real refractive index for the aerosol. Aerosol light scattering was measured with several nephelometers for "dry," near ambient, and controlled high RH conditions. Parallel measurements of dry and controlled RH light scattering give a measure of the aerosol hygroscopic response. Furthermore, diameter growth factors were measured with a tandem DMA system for select particle dry diameters. Aerosols collected using a time-resolved aerosol collector and analyzed by scanning electron microscopy were used to characterize individual particle shape, mixing, and chemical components.

The range of complementary techniques used during YACS provided "harmony" intercomparisons and quality control checks on the various measurements. In addition, the breadth of information collected by the suite of instruments allowed for closure calculations on the aerosol light scattering properties and comparison to measurements. These included the reconstruction of light scattering using the IMPROVE protocols, as well as more detailed Mie light extinction calculations. Light scattering coefficients were calculated for comparison to measurements using measured particle size distributions and information on refractive index and chemical composition.

8.2 Summary of Findings

During summer 2002, air quality in the San Joaquin valley was the worst in several years, resulting in elevated $PM_{2.5}$, and much of this regional haze reached Yosemite National Park. Fine aerosol mass at Yosemite was dominated by POM. Overall, the average $PM_{2.5}$ gravimetric mass concentration was 9.6 μg/m^3, with POM, elemental carbon, ammonium sulfate, sodium nitrate, and soil dust accounting for 70, 4, 15, 5, and 6% respectively. The dominance of POM is exceptionally high, even among western U.S. national parks, and its properties were considerably different than standard assumptions. For example, based on mass reconstructions of $PM_{2.5}$, the

multiplier to convert organic carbon to POM was considerably higher (1.8) than values typically assumed in models and forecasts (1.4).

Total light extinction was dominated by light scattering by $PM_{2.5}$ (79%) with smaller contributions from coarse particles and particle light absorption. The average total dry light scattering coefficient by particles was 49 ± 36 Mm^{-1} (visual range Vr ~ 80 km based on the Koschmeider relationship only considering particle light scattering). During the mid-August smoke haze episode, the light scattering coefficient exceeded 200 Mm^{-1} (V_r ~ 20 km). These are much higher than typical "background" conditions in nonurban western U.S. sites that the EPA gives as 16 Mm^{-1} for Yosemite (annual average).

Overall, the influx of regional haze featured a shift to a larger but narrower mode of particles. Volume size distributions showed that geometric mean diameters ranged from ~ 0.2 μm during relatively clean periods to ~ 0.4 μm during the haziest periods. These shifts resulted in large impacts on haziness and visibility through an increased mass scattering efficiency. Reconstructed light scattering using the standard IMPROVE protocols of measured species concentrations and mass scattering efficiencies compared poorly to the measured light scattering coefficient. As part of this reconstruction, the EPA regional haze guidance suggests using a value of 4.0 m^2/g as a mass scattering efficiency for POM. However, using measured aerosol size distributions, retrieved refractive index, and Mie light scattering calculations, dry mass scattering efficiencies as high as 6 m^2/g were obtained and resulted in much better agreement with measured light scattering.

A secondary objective was to evaluate the comparability of a wide variety of aerosol monitoring systems including two semi-continuous monitors measuring inorganic ions and total carbon. The 24-hour "bulk" measurements of various aerosol species compared more favorably with each other than with the semi-continuous data. Sulfates, more than any other species, compared the most favorably across all monitoring systems. The difference between the two sampling systems for sulfate was 8% with an intervariable correlation coefficient of 0.98, while sulfate derived from the MOUDI sampler was 6% lower than the average of IMPROVE and URG. Generally, when OC was low, R&P OC was greater than IMPROVE/TOR, while the opposite was true at higher concentrations. On the average, R&P-derived OC was about 40% higher than IMPROVE/TOR OC, but more importantly, there was not a clear additive or multiplicative bias between the two

measurements. Both mass and light scattering reconstructions suggested that semi-continuous carbon measurements were biased and this bias was a function of the POM concentration.

Evidence from speciation, meteorological transport patterns, and smoke markers showed an important, though episodic, influence of biomass smoke. During one 14-day smoke episode in mid-August 2002, 24-hour $PM_{2.5}$ concentrations ranged from 15 to 20 $\mu g/m^3$ and POM contributed > 80% of $PM_{2.5}$. Carbon isotopic analysis from daily filters showed that modern (rather than fossil) carbon composed 73–95% of the $PM_{2.5}$ carbon. Nearly all variability in total carbon mass was from modern carbon (i.e., biogenic carbon from either secondary aerosol formation or wood smoke). Correlations between POM and soluble potassium, isotopic analysis, and speciation of POM suggest a dominant impact of smoke on $PM_{2.5}$ properties during YACS. The middle of August featured the most substantial smoke impact from multiple indicators. This period featured the highest POM concentrations, the largest divergence of UV and visible channel light absorption from the aethalometer, and the highest soluble potassium, likewise a biomass smoke indicator. The modern carbon fraction exhibits a similar profile, peaking above 95% in mid-August, though it never was less than 70%. Based on carbon speciation, dominant modern carbon sources were primary biomass smoke components (levoglucosan, anhydrosugars, methoxyphenols, resin acids) and secondary biogenic compounds (pinene oxidation products). Enhanced secondary organic aerosol from biogenic emissions associated with wildfires or condensation of precursor VOCs may have contributed synergistically. Organic speciation showed that vehicular emission tracers (hopanes and steranes) were detected at low concentrations, suggesting ~ 5% contribution to average POM. Massive wildfires in southwest Oregon that burned 0.5 million acres were an important contributor to haze at Yosemite. Widespread haze at neighboring IMPROVE sites and back trajectory analysis suggest large influences from regional wildfires, including particularly the Biscuit Complex (SW Oregon) fires and secondary contributions from the McNalley fire (SEKI) and small fires within Yosemite.

High time resolution measurements showed strong diurnal patterns associated with the mountain-valley thermal system, which imposed distinct, though sometimes differing, diurnal cycles on aerosol species. Generally though, upslope westerly flow each morning initiated transport of a quiescent haze layer from the valleys below. The pronounced diurnal pattern in OC concentrations, including afternoon peaks, also suggested a natural biogenic contribution. The ionic fraction of the aerosol was typically dominated by ammoniated sulfate (Figure 1). Close

tracking of NO_3^- and Na^+ concentrations provided evidence of the upwind reaction of nitric acid with sea salt before arrival at Yosemite. A diurnal pattern in aerosol size distribution was also evident with concentrations of accumulation mode particulates often increasing beginning in the morning, and an ultra-fine mode often appearing in the afternoon, perhaps resulting from nucleation events. Nitrate was strongly associated with the coarse mode aerosol. High time resolution interspecies correlations demonstrated nitrate to be associated with sodium and calcium, demonstrating the importance of aged sea salt and soil dust, respectively.

The predominance of POM greatly affected aerosol water uptake properties. Low hygroscopicity was observed, based on measurements of both growth in particle diameters and light scattering. Furthermore, decreasing hygroscopicity with increasing POM fraction was apparent. Diameter growth factors often showed separation into more and less hygroscopic modes, occurring at RH = 80% with average growth factors of 1.11 ± 0.04 and 1.29 ± 0.08 for the less and more hygroscopic modes for D_o = 200 nm particles. A strong inverse relationship between carbon content and hygroscopicity was particularly evident with 200 nm particles (R^2 = 0.72, using an exponential decay fit) with a growth factor at RH = 80% approaching 1.1 as the POM/ionic mass ratio exceeded 10. Though limited hygroscopic growth was typically observed for RH < 70%, beyond RH = 80%, growth was much weaker than typical ionic species. Particles of 200 nm grew by ratios of 1.14 and 1.29 at RH = 80% and 90%, respectively (compared with ~ 1.5 and 1.7 for pure $(NH_4)_2SO_4$ particles). Light scattering measurements showed yet lower growth due to the predominance of smoke in the optically important range. Comparison of light scattering at dry and unconditioned, near ambient RH demonstrated a very small contribution of aerosol phase water to atmospheric light extinction. The results showed that, though smoke particles take up water, their hygroscopic growth is considerably weaker than typical salt particles such as sulfates, nitrates, and sea salt.

Single particle analysis showed the presence of four different particle morphologies including volatile particles, nonvolatile particles, soot agglomerates, and “tar balls”. Most particles, however, were found to be internally mixed (i.e., having both inorganic and organic compounds) rather than being pure external mixtures. The largest smoke episode in mid-August revealed the presence of tar ball particles that were associated with long-range transport of biomass smoke to the park. Although tar balls have been observed previously during biomass smoke events, their optical properties are not well understood. Results from this study suggest that tar balls efficiently

scatter light and do absorb solar radiation, which has important implications for visibility and climate effects of organic carbon particles emitted from biomass burning

8.3 Implications and Future Directions

The summer of 2002 in the western U.S. was an active fire season, and a prevalent influence of biomass smoke was observed at Yosemite. Evidence showed that some of the smoke properties were substantially different than standard assumptions used, for example, with the IMPROVE protocol. For instance, a larger POM/OC multiplier of 1.8 and a mass scattering efficiency of up to 6 m^2/g combine to yield an underestimate of smoke-related light scattering by about a factor of two if these results are typical of aged biomass smoke. These results should be examined for other smoke events where aerosol aging and fuel types are different. This is important to developing a better understanding of secondary organic aerosol formation in smoke plumes and how this affects POM/OC ratios, aerosol hygroscopicity, and light extinction efficiency. Exploring the markers for secondary organic aerosol and associating these with biogenic and pyrogenic sources is a priority.

During YACS, nitrate was typically observed in the form of sodium nitrate rather than the commonly assumed ammonium nitrate. Considering the chemical form and size distribution of nitrate at other locations and seasons has important implications for visibility impacts. Hygroscopic measurements suggested that the POM aerosol was weakly hygroscopic. The IMPROVE assumption of zero growth for POM and hygroscopic growth strictly attributable to ionic species may be a small underestimate of the visibility impacts of POM. Conversely, other models that assume smoke with substantial hygroscopic growth likely overestimate visibility impacts at high RH. As the smoke impacting Yosemite during YACS was largely well-aged (up to several days), the applicability of these results to primary and less aged smoke is an area for further study.

9. ***REFERENCES***

Abel, S.J., J.M. Haywood, E.J. Highwood, J. Li, and P.R. Buseck, Evolution of biomass burning aerosol properties from an agricultural fire in southern Africa, *Geophysical Research Letters*, *30* (15), Art. No. 1783, 2003.

Ames, R.B., and W.C. Malm, Chemical species' contributions to the upper extremes of aerosol fine mass, *Atmos. Environ.*, *35* (30), 5193-5204, 2001.

Ames, R.B., D.G. Fox, W.C. Malm, and B.A. Schichtel, Preliminary apportionments of carbonaceous aerosols to wild fire smoke using observations from the IMPROVE network, *A&WMA Regional Haze Specialty Conference*, 74, Asheville, NC, 2004.

Anderson, T.L., D.S. Covert, S.F. Marshall, M.L. Laucks, R.J. Charlson, A.P. Waggoner, J.A. Ogren, R. Caldow, R.L. Holm, F.R. Quant, G.J. Sem, A. Wiedensohler, N.A. Ahlquist, and T.S. Bates, Performance characteristics of a high-sensitivity, three-wavelength, total scatter/backscatter nephelometer, *J. Atmos. Oceanic Technol.*, *13* (5), 967-986, 1996.

Andreae, M.O., Soot carbon and excess fine potassium: long-range transport of combustion-derived aerosols, *Science*, *220*, 1148-1151, 1983.

Andreae, M.O., and P.J. Crutzen, Atmospheric aerosols: biogeochemical sources and role in atmospheric chemistry, *Science*, *276*, 1052-1058, 1997.

Andreae, M.O., and P. Merlet, Emission of trace gases and aerosols from biomass burning, *Global Biogeochem. Cycles*, *15* (4), 955-966, 2001.

Ansari, A.S., and S.N. Pandis, Water absorption by secondary organic aerosol and its effect on inorganic aerosol behavior, *Environ. Sci. Technol.*, *34*, 71-77, 2000.

Bench, G., and P. Herckes, Measurement of contemporary and fossil carbon contents of $PM_{2.5}$ aerosols: Results from Turtleback Dome, Yosemite National Park (vol 38, pg 2424, 2004), *Environ. Sci. Technol.*, *38* (10), 2960-2960, 2004.

Blanchard, D.C., and A.H. Woodcock, The production, concentration, and vertical distribution of the sea-salt aerosol, *Annals of the New York Academy of Sciences*, *338*, 330-346, 1980.

Brechtel, F.J., and S.M. Kreidenweis, Predicting particle critical supersaturation from hygroscopic growth measurements in the humidified TDMA. Part II: Laboratory and ambient studies, *Journal of the Atmospheric Sciences*, *57* (12), 1872-1887, 2000.

Brooks, S.D., P.J. DeMott, and S.M. Kreidenweis, Water uptake by particles containing humic materials and mixtures of humic materials with ammonium sulfate, *Atmos. Environ.*, *38* (13), 1859-1868, 2004.

Brown, S.G., P. Herckes, L. Ashbaugh, M.P. Hannigan, S.M. Kreidenweis, and J.L. Collett, Characterization of organic aerosol in Big Bend National Park, Texas, *Atmos. Environ.*, *36* (38), 5807-5818, 2002.

Carrico, C.M., M.H. Bergin, J. Xu, K. Baumann, and H. Maring, Urban aerosol radiative properties: Measurement during the 1999 Atlanta Supersite Experiment, *J. Geophys. Res.*, *108* (D7, 8422), doi: 10.1029/2001JD001222, 2003a.

Carrico, C.M., P. Kus, M.J. Rood, P.K. Quinn, and T.S. Bates, Mixtures of pollution, dust, sea salt, and volcanic aerosol during ACE-Asia: Radiative properties as a function of relative humidity, *J. Geophys. Res.*, *108* (D23), 2003b.

Carrico, C.M., S.M. Kreidenweis, W.C. Malm, D.E. Day, T. Lee, J. Carrillo, G.R. McMeeking, and J.L. Collett, Hygroscopic growth behavior of a carbon-dominated aerosol in Yosemite National Park, *Atmos. Environ.*, *39*, 1393-1404, 2005.

Charlson, R.J., J. Langner, and H. Rodhe, Sulphate aerosol and climate, *Nature*, *348* (22), 1990.

Charlson, R.J., S.E. Schwartz, J.M. Hales, R.D. Cess, J.A. Coakley, Jr., J.E. Hansen, and D.J. Hofmann, Climate forcing by anthropogenic aerosols, *Science*, *255*, 423-430, 1992.

Chow, J.C., J.G. Watson, L.C. Pritchett, W.R. Pierson, C.A. Frazier, and R.G. Purcell, The DRI thermal/optical reflectance carbon analysis system: Description, evaluation and applications in U.S. air quality studies, *Atmos. Environ.*, *27A* (8), 1185-1201, 1993.

Chung, S.H., and J.H. Seinfeld, Global distribution and climate forcing of carbonaceous aerosols, *J. Geophys. Res.*, *107* (D19), Art. No. 4407, 2002.

Clegg, S.L., P. Brimblecomb, and A. Wexler, A thermodynamic model of the system H+ - NH4+ - SO42- -NO3- - H2O at tropospheric temperatures, *Journal of Physical Chemistry A*, *102*, 2137-2154, 1998.

Cocker, D.R., N.E. Whitlock, R.C. Flagan, and J.H. Seinfeld, Hygroscopic properties of Pasadena, California aerosol, *Aerosol Sci. Technol.*, *35* (2), 637-647, 2001.

Conny, J.M., and J.F. Slater, Black carbon and organic carbon in aerosol particles from crown fires in the Canadian boreal forest, *J. Geophys. Res.*, *107* (D11), 4116, doi:10.1029/2001JD001528, 2002.

Day, D.E., and W.C. Malm, Aerosol light scattering measurements as a function of relative humidity: a comparison between measurements made at three different sites, *Atmos. Environ.*, *35* (30), 5169-5176, 2001.

Day, D.E., W.C. Malm, and S.M. Kreidenweis, Aerosol light scattering measurements as a function of relative humidity, *J. Air Waste Manage. Assoc.*, *50* (5), 710-716, 2000.

Draxler, R.R., J.T. Mcqueen, and B.J.B. Stunder, An evaluation of air pollutant exposures due to the 1991 Kuwait oil fires using a Lagrangian model, *Atmos. Environ.*, *28* (13), 2197-2210, 1994.

Engling, G., P. Herckes, S.M. Kreidenweis, W.C. Malm, and J.L. Collett, Composition of the fine organic aerosol in Yosemite National Park during the 2002 Yosemite Aerosol Characterization Study, *Atmos. Environ, in press*, 2005.

Formenti, P., W. Elbert, W. Maenhaut, J. Haywood, S. Osborne, and M.O. Andreae, Inorganic and carbonaceous aerosols during the Southern African Regional Science Initiative (SAFARI 2000)

experiment: Chemical characteristics, physical properties, and emission data for smoke from African biomass burning, *J. Geophys. Res.*, *108* (D13), doi:10.1029/2002JD002408, 2003.

Fuller, K.A., W.C. Malm, and S.M. Kreidenweis, Effects of mixing on extinction by carbonaceous particles, *J. Geophys. Res.*, *104* (D13), 15941-15954, 1999.

GCVTC, *Report of the Grand Canyon Visibility Transport Commission to the United States Environmental Protection Agency*, http://www.westgov.org/wga/publicat/final.doc, 92 pp., 1996.

GCVTC, *Grand Canyon Visibility Transport Commission Integrated Assessment System Documentation Summary Task 2.1 Final Report*, The Pechan-Avanti Group, a unit of E.H. Pechan & Associates, Inc., Pechan Report No. 99.03.001/572, Springfield, VA, 74 pp., 1999.

Gebhart, K.A., S.M. Kreidenweis, and W.C. Malm, Back-trajectory analyses of fine particulate matter measured at Big Bend National Park in the historical database and the 1996 scoping study, *Sci. Total Environ.*, *276* (1-3), 185-204, 2001.

Graham, B., P. Guyon, W. Maenhaut, P.E. Taylor, M. Ebert, S. Matthias-Maser, O.L. Mayol-Bracero, R.H.M. Godoi, P. Artaxo, F.X. Meixner, M.A.L. Moura, C. Rocha, R. Van Grieken, M.M. Glovsky, R.C. Flagan, and M.O. Andreae, Composition and diurnal variability of the natural Amazonian aerosol, *J. Geophys. Res.*, *108* (D24), 2003.

Hand, J.L., and S.M. Kreidenweis, A new method for retrieving particle refractive index and effective density from aerosol size distribution data, *Aerosol Sci. Technol.*, *36* (10), 1012-1026, 2002.

Hand, J.L., W.C. Malm, D. Day, T. Lee, C. Carrico, J. Carrillo, J.L. Collett, A. Laskin, C. Wang, J.P. Cowin, and M.J. Iedema, Optical, physical and chemical properties of tar balls observed during the Yosemite Aerosol Characterization Study, *J. Geophys. Res.*, *110*, doi:10.1029/204JD005728, 2005.

Hansen, A.D.A., H. Rosen, and T. Novakov, The aethalometer - an instrument for the real-time measurement of optical-absorption by aerosol-particles, *Sci. Total Environ.*, *36* (JUN), 191-196, 1984.

Hansson, H.-C., M.J. Rood, S. Koloutsou-Vakakis, K. Hameri, D. Orsini, and A. Wiedensohler, NaCl aerosol particle hygroscopicity dependence on mixing with organic compounds, *J. Atmos. Chem.*, *31* (3), 321-346, 1998 .

Hao, W.M., and M.H. Liu, Spatial and temporal distribution of tropical biomass burning, *Global Biogeochem. Cycles*, *8* (4), 495-503, 1994.

Haywood, J.M., S.R. Osborne, P.N. Francis, A. Keil, P. Formenti, M.O. Andreae, and P.H. Kaye, The mean physical and optical properties of regional haze dominated by biomass burning aerosol from the C-130 aircraft during SAFARI 2000, *J. Geophys. Res.*, *108* (D13, 8473), doi:10.1029/2002JD002226, 2003.

Hering, S.V., and P.H. McMurry, Optical counter response to monodisperse atmospheric aerosols, *Atmos. Environ.*, *25A*, 463-468, 1991.

Hinds, W.C., *Aerosol Technology: Properties, Behavior, and Measurement of Airborne Particles*, 483 pp., Wiley-Interscience, New York, 1999.

Hobbs, P.V., J.S. Reid, R.A. Kotchenruther, R.J. Ferek, and R. Weiss, Direct radiative forcing by smoke from biomass burning, *Science*, *275*, 1776-1778, 1997.

Huebert, B.J., and R.J. Charlson, Uncertainties in data on organic aerosols, *Tellus*, *52* (5), 1249-1255, 2000.

Iacobellis, S.F., R. Frouin, and R.C.J. Somerville, Direct climate forcing by biomass-burning aerosols: Impact of correlations between controlling variables, *J. Geophys. Res.*, *104* (D10), 12031-12046, 1999.

Kaufman, Y.J., P.V. Hobbs, V.W.J.H. Kirchhoff, P. Artaxo, L.J. Remer, B.N. Holben, M.D. King, D.E. Ward, E.M. Prins, K.M. Longo, L.F. Mattos, C.A. Nobre, J.D. Spinhirne, Q. Ji, A.M. Thompson, J.F. Gleason, S.A. Christopher, and S.-C. Tsay, Smoke, clouds, and radiation - Brasil (SCAR-B) experiment, *J. Geophys. Res.*, *103* (D24), 31783-31808, 1998.

Knutson, E.O., and P.J. Lioy, Measurement and presentation of aerosol size distributions, in *Air Sampling Instruments for Evaluation of Atmospheric Contaminants, 7th Edition*, edited by S.V. Hering, pp. 59-71, American Conference of Governmental Industrial Hygienists, Cincinnati, OH, 1989.

Kotchenruther, R.A., and P.V. Hobbs, Humidification factors of aerosols from biomass burning in Brazil, *J. Geophys. Res.*, *103* (D24), 32081-32089, 1998.

Kreidenweis, S.M., L.A. Remer, R. Bruintjes, and O. Dubovik, Smoke aerosol from biomass burning in Mexico: Hygroscopic smoke optical model, *J. Geophys. Res.*, *106* (D5), 4831-4844, 2001.

Laskin, A., and J.P. Cowin, Automated single particle SEM/EDX analysis of submicrometer particles down to 0.1 μm, *Anal. Chem.*, *73* (5), 1023-1029, 2001.

Laskin, A., M.J. Iedema, and J.P. Cowin, Time-resolved aerosol collector for CCSEM/EDX single-particle analysis, *Aerosol Sci. Technol.*, *37* (3), 246-260, 2003.

Lee, T., S.M. Kreidenweis, and J.L. Collett, Aerosol ion characteristics during the Big Bend Regional Aerosol and Visibility Observational Study, *J. Air Waste Manage. Assoc.*, *54* (5), 585-592, 2004.

Ma, Y., R.J. Weber, Y.N. Lee, D.A. Orsini, K. Maxwell-Meier, D.C. Thornton, A.R. Bandy, A.D. Clarke, D.R. Blake, G.W. Sachse, H.E. Fuelberg, C.M. Kiley, J.H. Woo, D.G. Streets, and G.R. Carmichael, Characteristics and influence of biosmoke on the fine-particle ionic composition measured in Asian outflow during the Transport and Chemical Evolution Over the Pacific (TRACE-P) experiment, *J. Geophys. Res.*, *108* (D21), 2003.

MacCleery, D.W., *American Forests: A History of Resiliency and Recovery*, United States Department of Agriculture Forest Service, FS-540, Durham, NC, 1992.

Malm, W.C., and D.E. Day, Estimates of aerosol species scattering characteristics as a function of relative humidity, *Atmos. Environ.*, *35* (16), 2845-2860, 2001.

Malm, W.C., and S.M. Kreidenweis, The effects of models of aerosol hygroscopicity on the apportionment of extinction, *Atmos. Environ.*, *31* (13), 1965-1976, 1997.

Malm, W.C., and M.L. Pitchford, Comparison of calculated sulfate scattering efficiencies as estimated from size-resolved particle measurements at three national locations, *Atmos. Environ.*, *31* (8), 1315-1326, 1997.

Malm, W.C., J.F. Sisler, D. Huffman, R.A. Eldred, and T.A. Cahill, Spatial and seasonal trends in particle concentration and optical extinction in the United-States, *J. Geophys. Res.*, *99* (D1), 1347-1370, 1994.

Malm, W.C., J.V. Molenar, R.A. Eldred, and J.F. Sisler, Examining the relationship among atmospheric aerosols and light scattering and extinction in the Grand Canyon area, *J. Geophys. Res.*, *101* (D14), 19251-19265, 1996.

Malm, W.C., B.A. Schichtel, R.B. Ames, and K.A. Gebhart, A 10-year spatial and temporal trend of sulfate across the United States, *J. Geophys. Res.*, *107* (D22), doi:10.1029/2002JD002107, 2002.

Malm, W.C., D.E. Day, S.M. Kreidenweis, J.L. Collett, and T. Lee, Humidity-dependent optical properties of fine particles during the Big Bend regional aerosol and visibility observational study, *J. Geophys. Res.*, *108* (D9), doi:10.1029/2002JD002998, 2003.

Malm, W.C., B.A. Schichtel, M.L. Pitchford, L.L. Ashbaugh, and R.A. Eldred, Spatial and monthly trends in speciated fine particle concentration in the United States, *J. Geophys. Res.*, *109* (D03306), doi:10.1029/2003JD003739, 2004.

Malm, W.C., D.E. Day, C.M. Carrico, S.M. Kreidenweis, J. J.L. Collett, G. McMeeking, T. Lee, J. Carrillo, and B.A. Schichtel, Intercomparison and closure calculations using measurements of aerosol species and optical properties during the Yosemite Aerosol Characterization Study, *J. Geophys. Res.*, *110*, doi:10.1029/2004JD005494, 2005a.

Malm, W.C., D.E. Day, S.M. Kreidenweis, J.L. Collett, C.M. Carrico, G. McMeeking, and T. Lee, Hygroscopic growth properties of an organic-laden aerosol, *Atmos. Environ.*, *39*, 4969-4982, 2005b.

Markowicz, K.M., P.J. Flatau, P.K. Quinn, C.M. Carrico, M.K. Flatau, A.M. Vogelmann, D. Bates, M. Liu, and M.J. Rood, Influence of relative humidity on aerosol radiative forcing: An ACE-Asia experiment perspective, *J. Geophys. Res.*, *108* (D23), 2003.

Marple, V.A., K.L. Rubow, and S.M. Behm, A micro-orifice uniform deposit impactor (MOUDI) - description, calibration, and use, *Aerosol Sci. Technol.*, *14* (4), 434-446, 1991.

Martins, V.J., P. Artaxo, C. Liousse, J.S. Reid, P.V. Hobbs, and Y.J. Kaufman, Effects of black carbon content, particle size, and mixing on light absorption by aerosols from biomass burning in Brasil, *J. Geophys. Res.*, *103* (D24), 32041-32050, 1998.

McDonald, J.D., B. Zielinska, E.M. Fujita, J.C. Sagebiel, J.C. Chow, and J.G. Watson, Fine particle and gaseous emission rates from residential wood combustion, *Environ. Sci. Technol.*, *34*, 2080-2091, 2000.

McKenzie, L.M., W.M. Hao, G.N. Richards, and D.E. Ward, Measurement and modeling of air toxins from smoldering combustion of biomass, *Environ. Sci. Technol.*, *29* (8), 2047-2054, 1995.

McMeeking, G.R., Size distribution measurements of wildfire smoke-influenced aerosol at Yosemite National Park, Master's thesis, Colorado State University, Fort Collins, CO, 2004.

McMeeking, G.R., S.M. Kreidenweis, C.M. Carrico, T. Lee, J.L. Collett, and W.C. Malm, Observations of smoke influenced aerosol during the Yosemite Aerosol Characterization Study: Size distributions and chemical composition, *J. Geophys. Res.*, *110*, doi:10.1029/2004JD005389, 2005a.

McMeeking, G.R., S.M. Kreidenweis, C.M. Carrico, J.L. Collett, D.E. Day, and W.C. Malm, Observations of smoke influenced aerosol during the Yosemite Aerosol Characterization Study: 2. Aerosol scattering and absorbing properties, *J. Geophys. Res.*, *110*, doi:10.1029/2004JD005624, 2005b.

Molenar, J.V., Analysis of the real world performance of the Optec NGN-2 ambient nephelometers, *Air and Waste Management Association Specialty Conference Visual Air Quality: Aerosols and Global Radiation Balance*, 243-265, 1997.

Molenar, J.V., D.L. Dietrich, and R.M. Tree, Application of a long range transmissometer to measure the ambient atmospheric extinction coefficient in remote pristine environments, in *Transactions Visibility and Fine Particles*, edited by C.V. Mathai, Air and Waste Management Association, Pittsburgh, PA, 1989.

Moosmuller, H., W.P. Arnott, C.F. Rogers, J.L. Bowen, J.A. Gillies, W.R. Pierson, J.F. Collins, T.D. Durbin, and J.M. Norbeck, Time-resolved characterization of diesel particulate emissions. 2. Instruments for elemental and organic carbon measurements, *Environ. Sci. Technol.*, *35* (10), 1935-1942, 2001.

Nenes, A., S.N. Pandis, and C. Pilinis, Continued development and testing of a new thermodynamic aerosol module for urban and regional air quality models, *Atmos. Environ.*, *33* (10), 1553-1560, 1999.

Ogunjobi, K.O., Z. He, K.W. Kim, and Y.J. Kim, Aerosol optical depth during episodes of Asian dust storms and biomass burning at Kwangju, South Korea, *Atmos. Environ.*, *38* (9), 1313-1323, 2004.

Park, R.J., D.J. Jacob, M. Chin, and R.V. Martin, Sources of carbonaceous aerosols over the United States and implications for natural visibility, *J. Geophys. Res.*, *108* (D12), 2003.

Penner, J.E., R.E. Dickenson, and C.A. O'Neill, Effects of aerosol from biomass burning on the global radiation budget, *Science*, *256*, 1432-1434, 1992.

Pilinis, C., S.N. Pandis, and J.H. Seinfeld, Sensitivity of direct climate forcing by atmospheric aerosols to aerosol-size and composition, *J. Geophys. Res.*, *100* (D9), 18739-18754, 1995.

Posfai, M., A. Gelencser, R. Simonics, K. Arato, J. Li, P.V. Hobbs, and P.R. Buseck, Atmospheric tar balls: Particles from biomass and biofuel burning, *J. Geophys. Res.*, *109* (D6), Art. No. D06213, 2004.

Prenni, A.J., P.J. DeMott, and S.M. Kreidenweis, Water uptake of internally mixed particles containing ammonium sulfate and dicarboxylic acids, *Atmos. Environ.*, *37* (30), 4243-4251, 2003.

Prospero, J.M., and D.L. Savoie, Effect of continental sources on nitrate concentrations over the Pacific Ocean, *Nature*, *339*, 687-689, 1989.

Pyne, S.J., *America's Fires : Management on Wildlands and Forests*, 54 pp., Forest History Society, Durham, NC, 1997a.

Pyne, S.J., *Fire in America, A Cultural History of Wildland and Rural fire*, University of Washington Press, Seattle, WA, 1997b.

Rader, D.J., and P.H. McMurry, Application of the tandem differential mobility analyzer to studies of droplet growth or evaporation, *J. Aerosol. Sci.*, *17* (5), 771-787, 1986.

Radke, L.F., D.A. Hegg, P.V. Hobbs, J.D. Nance, J.H. Lyons, K.K. Laursen, R.E. Weiss, P.J. Riggan, and D.E. Ward, Particulate and trace gas emissions from large biomass fires in North America, in *Global Biomass Burning: Atmospheric, Climatic and Biospheric Implications*, edited by R. Prinn, pp. 219-224, MIT Press, 1991.

Richardson, C.B., and R.L. Hightower, Evaporation of ammonium nitrate particles, *Atmos. Environ.*, *21* (4), 971-975, 1987.

Riebau, A.R., and D. Fox, The new smoke management, *Int. J. Wildland Fire*, *10* (3-4), 415-427, 2001.

Rogge, W.F., M.A. Mazurek, L.M. Hildemann, G.R. Cass, and B.R.T. Simoneit, Quantitation of urban organic aerosols at a molecular level: identification, abundance and seasonal variation, *Atmos. Environ.*, *27A* (8), 1309-1330, 1993.

Rosenfeld, D., Suppression of rain and snow by urban and industrial air pollution, *Science*, *287* (5459), 1793-1796, 2000.

Rupprecht, G., H. Patashnick, D.E. Beeson, R.N. Green, and M.B. Meyer, A new automated monitor for the measurement of particulate carbon in the atmosphere, *Particulate Health: Health and Regulatory Issues*, 1-6, Pittsburgh, PA, 1995.

Sachweh, B., H. Umhauer, F. Ebert, H. Buttner, and R. Friehmelt, In situ optical particle counter with improved coincidence error correction for number concentrations up to 10(7) particles cm(-3), *J. Aerosol. Sci.*, *29* (9), 1075-1086, 1998.

Saxena, P., and L.M. Hildemann, Water-soluble organics in atmospheric particles: a critical review of the literature and application of thermodynamics to identify candidate compounds, *J. Atmos. Chem.*, *24*, 57-109, 1996.

Saxena, P., L.M. Hildemann, P.H. McMurry, and J.H. Seinfeld, Organics alter hygroscopic behavior of atmospheric particles, *J. Geophys. Res.*, *100* (D9), 18755-18770, 1995.

Seinfeld, J.H., and S.N. Pandis, *Atmospheric Chemistry and Physics: From Air Pollution to Climate Change*, 1326 pp., John Wiley & Sons, Inc., New York, 1998.

Simoneit, B.R.T., J.J. Schauer, C.G. Nolte, D.R. Oros, V.O. Elias, M.P. Fraser, W.F. Rogge, and G.R. Cass, Levoglucosan, a tracer for cellulose in biomass burning and atmospheric particles, *Atmos. Environ.*, *33* (2), 173-182, 1999.

Sullivan, T.J., D.L. Peterson, C.L. Blanchard, and S.J. Tanenbaum, *Assessment of Air Quality and Air Pollutant Impacts in Class I National Parks of California*, United States Department of Interior-National Park Service, NPS D-1454, 2001.

Trijonis, J.C., W.C. Malm, M. Pitchford, M., W.H. White, R. Charlson, and R. Husar, *Visibility: Existing and Historical Conditions: Causes and Effects*, National Acid Precipitation Assessment Program, Report 24, Washington, DC, 1990.

Turpin, B.J., and H.-J. Lim, Species contributions to $PM_{2.5}$ mass concentrations: Revisiting common assumptions for estimating organic mass, *Aerosol Sci. Technol.*, *35* (1), 602-610, 2001.

United States Environmental Protection Agency, *Regional Haze Regulations; Final Rule*, Code of Federal Regulations, Title 40, Part 51, Fed. Regist., pp. 35714-35774, 1999.

United States Environmental Protection Agency, *Guidance for Tracking Progress under the Regional Haze Rule*, EPA-454/B-03-004, Research Triangle Park, NC, 100 pp., 2003a.

United States Environmental Protection Agency, *Guidance for Estimating Natural Visibility Conditions Under the Regional Haze Program*, EPA-454/B-03-005, Research Triangle Park, NC, 66 pp., 2003b.

Weber, R.J., D. Orsini, Y. Daun, Y.N. Lee, P.J. Klotz, and F. Brechtel, A particle-into-liquid collector for rapid measurement of aerosol bulk chemical composition, *Aerosol Sci. Technol.*, *35* (3), 718-727, 2001.

Wotawa, G., and M. Trainer, The influence of Canadian forest fires on pollutant concentrations in the United States, *Science*, *288* (5464), 324-328, 2000.

Zhang, X.Q., B.J. Turpin, P.H. McMurry, S.V. Hering, and M.R. Stolzenburg, Mie theory evaluation of species contributions to 1990 wintertime visibility reduction in the Grand-Canyon, *J. Air Waste Manage. Assoc.*, *44* (2), 153-162, 1994.

10. ***APPENDIX***

Bibliography

Carrico, C.M., S.M. Kreidenweis, W.C. Malm, D.E. Day, T. Lee, J. Carrillo, G.R. McMeeking, and J.L. Collett Jr., Hygroscopic growth behavior of a carbon-dominated aerosol in Yosemite National Park, *Atmos. Environ.*, *39*, 1393-1404, 2005.

Engling, G., P. Herckes, S.M. Kreidenweis, W.C. Malm, and J.L. Collett Jr., Composition of the fine organic aerosol in Yosemite National Park during the 2002 Yosemite Aerosol Characterization Study, *Atmos. Environ, in press*, 2005.

Hand, J.L., W.C. Malm, D. Day, T. Lee, C. Carrico, J. Carrillo, J.L. Collett Jr., A. Laskin, C. Wang, J.P. Cowin, and M.J. Iedema, Optical, physical and chemical properties of tar balls observed during the Yosemite Aerosol Characterization Study, *J. Geophys. Res.*, *110*, doi:10.1029/204JD005728, 2005.

Malm, W.C., D.E. Day, C.M. Carrico, S.M. Kreidenweis, J. J.L. Collett Jr., G. McMeeking, T. Lee, J. Carrillo, and B.A. Schichtel, Intercomparison and closure calculations using measurements of aerosol species and optical properties during the Yosemite Aerosol Characterization Study, *J. Geophys. Res.*, *110*, doi:10.1029/2004JD005494, 2005a.

Malm, W.C., D.E. Day, S.M. Kreidenweis, J.L. Collett Jr., C.M. Carrico, G. McMeeking, and T. Lee, Hygroscopic growth properties of an organic-laden aerosol, *Atmos. Environ.*, *39*, 4969-4982, 2005b.

McMeeking, G.R., S.M. Kreidenweis, C.M. Carrico, T. Lee, J.L. Collett Jr., and W.C. Malm, Observations of smoke influenced aerosol during the Yosemite Aerosol Characterization Study: Size distributions and chemical composition, *J. Geophys. Res.*, *110*, doi:10.1029/2004JD005389, 2005a.

McMeeking, G.R., S.M. Kreidenweis, C.M. Carrico, J.L. Collett Jr., D.E. Day, and W.C. Malm, Observations of smoke influenced aerosol during the Yosemite Aerosol Characterization Study: 2. Aerosol scattering and absorbing properties, *J. Geophys. Res.*, *110*, doi:10.1029/2004JD005624, 2005b.

McMeeking, G.R., S.M. Kreidenweis, M. Lunden, J. Carrillo, C.M., Carrico, T. Lee, P. Herckes, G. Engling, D.E. Day, J.L. Hand, N. Brown, W.C. Malm, and J.L. Collett Jr., Smoke-impacted regional haze in California during the summer of 2002. *Agricultural and Forest Meteorology, accepted* 17 January 2006.